The Electro-Chemo-Mechanical Coupling in Lithium Alloy Electrodes

**Vom Promotionsausschuss der
Technischen Universität Hamburg-Harburg**

zur Erlangung des akademischen Grades

Doktor der Naturwissenschaften (Dr. rer. nat.)

genehmigte Dissertation

von
Tobias Kitzler

aus
Haag am Hausruck, Österreich

2016

Acknowledgements

I want to thank Prof. Jörg Weißmüller for giving me the possibility to write my thesis in the group "Hybrid materials" of the "Materials mechanics" institute at the Helmholtz-Zentrum Geesthacht. Furthermore I want to thank him, for introducing me to the topic of the interaction of electrochemistry and mechanics, as well as the deep insight into the thermodynamics of electrochemical systems. Among many other aspects of my work he has made possible, I want to say a special thanks for the freedom to work in my own way.

A second person who enabled me to do this work is Jürgen Markmann. Whit countless discussions on scientific and not as scientific topics he helped a lot and gave me a deep scientific insight in many aspects of materials science and x-ray diffraction. Furthermore he always lent me an ear for all my thoughts, even if they had not been completely thought through. Those discussions were extremely helpful to accomplish an understanding on the interrelations of different physical measures. Apart from scientific discussions Jürgen was very important for me as well. Especially in difficult times I could always count on him.

I want to thank Prof. Dr. rer. nat. Andreas Stierle for being the second reviewer for this thesis and Prof. Dr. Erica Lilleodden for being the chairman of the Disputation.

Of course I want to thank all my colleges from the HZG as well as the TUHH. Amongst many others my special thanks goes to Nadiia Mameka, Ban Dinh Nam Ngo, Jana Wilmers, Charlotte Stenner, Edgar Hussar, Lukas Lührs, Yahui Xue, Mark Busch, Urs Haßlinger for countless discussions on scientific and other topics. Nadiia Mameka for the countless times where she helped me in the lab and with sample preparation. Qibo Deng and Maxim Smetanin for helping me with the dynamic electro-chemo-mechanical analysis and again Qibo Deng for the scanning tunnelling micrograph he made for me. Julia Hütsch for the help with the scanning electron microscopy and for performing the electron backscatter diffraction for me. Jana Wilmers and Jürgen Markmann, Astrid and Andreas Safron for proofreading my thesis. Edgar Hussar for the finite element modelling which helped clarify some aspects. Jürgen Knaak for many favors with regards to laboratory equipment and last but not least I want to thank Bernhard Eltzschig for manufacturing several parts of the in-situ electrochemical cells as well as Henning Lohmann for transferring my Designs to construction blueprints and the technikum for manufacturing the DECMA stage and parts of the in-situ electrochemical cell.

For the support in preparing and during the measurements at the synchrotron facility BESSY II in Berlin I wan to thank again Jürgen Markmann, Emad Maawad, Daniel M. Többens and Markus Ziehmer. It wouldn't have been possible without you.

For the financing of my work as part of the "Energiespeicher Initiative" I want to thank the Helmholtz community.

Work isn't everything, so I want to thank all my colleges and friends for turning Hamburg from the place where I live to my home. I really enjoyed the last years and all of you had a lot to do with this.

Last but not least I want to thank all members of my family, my mum Hildegard and my dad Robert as well as my siblings Astrid Manuel and Paul as well as their partners for the tremendous amount of support and love I have received in every possible way. You gave me the strength to go my way and finish this thesis.

<div align="center">Thank you!!!</div>

Abstract

Lithium-alloy electrodes are among the most promising battery anodes for future generations of lithium-ion batteries. Due to electrochemically induced stresses, which arise from the volume change upon loading and unloading, these electrodes suffer from poor cycling stability. Additionally, these stresses couple with the electrochemical potential, which can lead to an inhomogeneous lithium distribution with the potential consequence of a reduced mechanical stability. In order to increase the cycling stability, the structure size of alloy electrodes is being reduced, which on the one hand reduces the stress due to alloy formation and on the other hand increases the impact of the surface stress because of the significantly increased surface to volume ratio. This increase influences the mechanical stability as well.

Measurements of the coupling of the electromotive force to mechanical stresses/strains, as well as distinction of surface and bulk contributions to this coupling turn out to be quite challenging. In the course of this work the dynamic electro-chemo-mechanical analysis (DECMA), which is an established method in aqueous electrolytes, is tested in lithium-ion battery electrolytes to provide a direct way of measuring the potential-strain coupling parameter. For distinguishing surface and bulk contributions, the results are compared to tilting angle dependent changes of the lattice parameter. In order to do so the following steps were required:

- Calculating the effective dynamic electro-chemo-mechanical coupling parameter from two separate contributions.
- Calculation of the interrelation of the electro-chemo-mechanical coupling parameter with the change in lattice parameter, i.e. creation of an appropriate model description for the electrode.
- Design of a dynamic electro-chemo-mechanical analysis stage for measurements in lithium-salt containing electrolytes.
- Design of an in-situ electrochemical cell suitable for measuring the lattice parameter during electrochemical cycling, parallel and perpendicular to the surface.

DECMA and in-situ x-ray diffraction experiments were successfully carried out for a gold model-electrode. Using the measured effective electro-chemo-mechanical coupling parameter and cyclic voltammetry data, it was possible to evaluate an interval for the local electro-chemo-mechanical coupling parameter of underpotential deposition of lithium on the gold surface of ($0.7\,\text{V} < \widehat{\varsigma}_{\text{UPD}} < 1.07\,\text{V}$). A corresponding electro-chemo-mechanical coupling parameter, which was calculated from literature density functional theory results ($\widehat{\varsigma}_{\text{UPD}} = 0.84\,\text{V}$) is well within this interval.

A comparison of the lattice parameter changes to results from cantilever bending experiments shows good qualitative correlation under the assumption that both are linked to bulk mechanisms. Qualitative differences are found most prominent where underpotential deposition and stripping occurs. This finding lead to the conclusion, that bulk effects are responsible for changes of the lattice parameter.

Finally the results of the dynamic electro-chemo-mechanical analysis and the lattice parameter shift were compared according to the electrode model. Again this comparison shows good qualitative correlation in a wide potential range. Significant differences appear as expected for underpotential deposition and stripping, and in a potential range where electrolyte decomposition is expected. This is because these processes appear at the surface and not in the bulk of the electrode. These results lead to the conclusion that in the potential range of 250 to 2000 mV vs. Li/Li$^+$ a major part of the stress results from bulk contributions. Consequently, a major part of the charge transported while

cycling in the corresponding potential range results from lithium entering the volume. The lattice parameter changes together with the behaviour of the electro-chemo-mechanical coupling parameter give a strong indication that, in the potential range under investigation, lithium is mainly deposited within grain boundaries of the gold model electrode.

Kurzfassung

Lithium-Legierungselektroden gehören zu den vielversprechendsten Batterieanoden für zukünftige Lithium-Ionen Batteriesysteme. Auf Grund von elektrochemisch induzierten mechanischen Spannungen, verursacht durch Volumenänderungen während des Lade- und Entladevorgangs, leiden diese Elektrodenmaterialien unter einer geringen Zyklenstabilität. Zusätzlich dazu sind die mechanischen Spannungen mit dem elektrochemischen Potential gekoppelt, was zu einer inhomogenen Verteilung von Lithium und in Folge dessen zu einer Reduktion der mechanischen Stabilität führen kann. Um die Zyklenstabilität zu erhöhen, geht der Trend zu immer kleineren Strukturgrößen der Elektrodenmaterialien. Dadurch wird zum einen die mechanische Spannung durch die Volumenänderung reduziert, zum anderen wird durch die folglich deutlich erhöhte Oberfläche auch der Einfluss der elastischen Grenzflächenspannung erhöht, was wiederum die mechanische Stabilität beeinflussen kann.

Sowohl die Messung der Kopplungsstärke des chemischen Potentials mit der mechanischen Spannung/Dehnung, als auch die Unterscheidung von Beiträgen der Oberfläche und des Volumens zu dieser Kopplung, erweist sich bisher als sehr herausfordernd. Im Zuge der vorliegenden Arbeit wird eine in wässrigen Elektrolyten etablierte Methode (die dynamische elektro-chemo-mechanische Analyse, DECMA) in Lithium-Ionen Batterieelektrolyten für die direkte Messung des elektro-chemo-mechanischen Kopplungsparameters verwendet. Zur Unterscheidung von Oberflächen- und Volumeneffekten werden die Ergebnisse mit kippwinkelabhängigen Änderungen des Gitterparameters während elektrochemischer Zyklen verglichen. Um das zu ermöglichen waren mehrere Schritte notwendig:

- Berechnung eines effektiven elektro-chemo-mechanischen-Kopplungsparameters aus zwei unterschiedlichen Beiträgen.
- Berechnung des Zusammenhangs zwischen elektro-chemo-mechanischer-Kopplung und Gitterparameteränderung für Oberflächen und Volumeneffekte anhand eines Elektrodenmodells.
- Design eines Aufbaus zur dynamischen elektro-chemo-mechanischen- Analyse in Lithium Elektrolyten.
- Design einer elektrochemischen Zelle zur in-situ Messung des Gitterparameters während elektrochemischer Zyklen parallel und normal zur Oberfläche.

Beide experimentellen Aufbauten wurden erfolgreich zur Untersuchung einer Gold-Modellelektrode verwendet. Mithilfe der Ergebnisse war es möglich ein Intervall für den lokalen Elektro-Chemo-Mechanischen-Kopplungs- Parameter der Unterpotentialabscheidung von Lithium auf Gold anzugeben ($0.7\,\mathrm{V} < \widehat{\varsigma}_{\mathrm{UPD}} < 1.07\,\mathrm{V}$). Ein entsprechender Kopplungs- Parameter welcher aus Dichtefunktional-Theorie basierten Literaturwerten berechnet wurde ($\widehat{\varsigma}_{\mathrm{UPD}} = 0.84\,\mathrm{V}$) liegt genau in diesem Intervall.

Ein Vergleich der Gitterparameter Änderung mit Ergebnissen von Biegebalken-Experimenten zeigt unter der Annahme, dass die Messergebnisse von Volumeneffekten hervorgerufen werden, eine über weite Bereiche gute qualitative Übereinstimmung. Abweichungen treten vorwiegend in Potentialbereichen auf, bei denen Unterpotentialabscheidung oder -abtragung stattfindet.

Zuguterletzt wurden die Ergebnisse aus beiden Messungen anhand des Elektrodenmodells miteinander verglichen. Dieser Vergleich zeigt ebenfalls über weite Potentialbereiche gute qualitative Übereinstimmung. Größere Abweichungen treten nur in Potentialbereichen auf, bei denen Lithium abgeschieden oder abgetragen wird, oder Elektrolytzersetzung zu erwarten ist, was darauf zurückzuführen ist, dass diese Prozesse an der Oberfläche auftreten und nicht im Volumen. Die Ergebnisse lassen somit den Schluss zu, dass ein großer Teil der mechanischen Spannungen, im Bereich von 2 V

bis 250 mV bezüglich Li/Li$^+$, auf Volumeneffekten beruht. Des Weiteren lässt sich abschätzen, dass ein großer Teil der Ladung die fließt, während das Potential geändert wird durch Lithium, welches in das Volumen der Probe eindringt, verursacht wird. Das Verhlaten des elektro-chemo-mechanischen Kopplungsparameters zusammen mit der Änderung des Gitterparameters sind ein starkes Indiz dafür, dass im untersuchten Potentialbereich die Einlagerung von Lithium in Gold vorwiegend in den Korngrenzen stattfindet.

Contents

1 Introduction and motivation

Before starting the introduction a short overview on the terminology is required. The positive and negative electrodes of secondary (rechargeable) batteries are often named cathode and anode, corresponding to the electrochemical function during unloading of the battery. For characterising electrodes there are some common measures: The electrode potential, the amount of lithium they can store with respect to volume or mass, as well as the cycling stability (a value which measures the number of load-unload cycles until the capacity drops below a certain fraction of the initial capacity). Electrode potentials are typically measured against a reference potential. The usual reference electrodes used in aqueous electrolytes are not suitable for lithium ion-battery cells, hence another reference electrode is required. A common reference is the Nernst potential of lithium (Li/Li^+). For comparing the amount of lithium the electrode can store, the volumetric capacity (amount of lithium, which can be stored reversibly per volume of the electrode) and the specific capacity (amount of lithium, which can be stored reversibly per weight of the electrode) are used. Both of those values depend on the state of charge. This sometimes leads to confusions like the indication that the lithium silicon alloy has a higher specific capacity than metallic lithium (see e.g. [1]). To omit this confusion, the specific and the volumetric capacity will be given in the charged state, when the active lithium is at the negative electrode.

A measure for the interaction of electrochemistry and mechanics is the so called electrocapillary coupling parameter, which is related to surface effects as suggested by the term "electrocapillary". In the thesis at hand, bulk effects are of major concern, hence it seems misleading to the author to use "electrocapillary". This is even more pressing, since another coupling parameter for electrochemistry and mechanics is introduced, which represents the measurable value in case more than one effects contributes to the measurement. To omit this misleading terminology, the electrocapillary coupling parameter will be called the potential-strain coupling parameter (PSCP) of the surface (ς^s). In a similar manner the apparent electrocapillary coupling parameter will be called the PSCP of the bulk (ς^b).

Since the early 1990's when commercial lithium-ion batteries were introduced, these batteries have turned into one of the most important energy storage devices. Nowadays they can be found in almost every portable electronic device. The big success of lithium-ion batteries is a result of the high energy density compared to other commercially available secondary battery systems. This has become possible, because of several differences to other secondary battery technologies. First of all, using lithium has the big advantage that it has the lowest weight per atom and the lowest electrochemical potential of all metals. Furthermore the electrolyte is not involved in the reversible electrode reactions (in contrast to e.g. lead acid or nickel–cadmium batteries), nor are the components dissolved in the electrolyte (at least ideally). This allows to use a very small amount of electrolyte, and to build batteries, that provide a high voltage (e.g. average of $3.7\,V$ for cells with a carbon anode and a $Li_{1-x}CoO_2$ cathode) at a high specific charge (charge per weight). These features make the Lithium-ion battery the rechargeable battery with the highest specific energy (stored energy per weight) as well as highest energy density (stored energy per volume) operating at room temperature on the market [2]. The huge success of lithium-ion batteries and the fact that commercial batteries are still far away from the theoretical capacities [3], has triggered lots of research activities. Besides the volumetric and the specific capacity of the battery many other aspects, like the cycling stability, the power density, the energy storage efficiency, the operation temperature and safety issues have to be considered. The overall performance of the battery naturally depends on all the components of the battery including the electrodes, the electrolyte, the current collectors as well as the separator. Already the number of
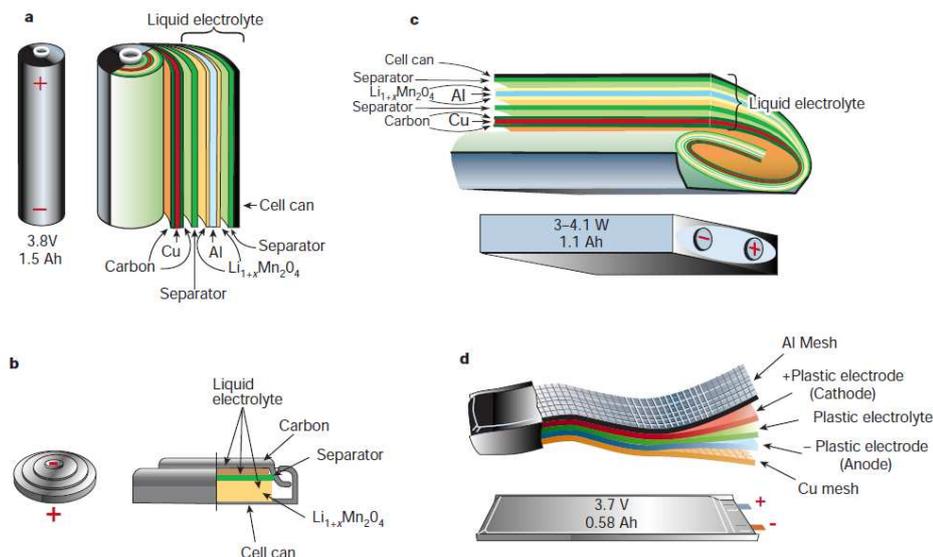
Figure 1.1: Schematic representation of commercial lithium-ion batteries in different shape: a) cylindrical b) coin cell c) prismatic cell and d) thin and flexible plastic cell. Except the plastic cell all cells use a separator. The plastic cell does not require a separator since it has no free electrolyte. Graphic from [2]

impact factors and performance measures indicates the complexity of the Problem. One consequence of this complexity is, that by increasing the specific capacity of current anode materials has only a moderate impact on the specific capacity of the whole battery, while for potential future battery systems increasing the specific capacity of the anode might be mandatory in order to out outperform state of the art lithium-ion batteries. In the following a short overview on state of the art lithium-ion batteries will be given, followed by some prominent examples for potential future lithium-ion battery systems.

As every electrochemical cell, lithium-ion battery cells consist of two electrodes and an electrolyte. Additionally to this, current collectors, which provide an electrical connection of the electrodes to the battery connectors, are required because lithium-ion batteries are sensitive to air and moisture. Furthermore lithium-ion batteries typically use a separator, which ensures a spacial separation of the anode and the cathode. A schematic representation of typical lithium ion batteries can be seen in figure 1.1. Both electrodes typically consist of host material particles mixed with carbon black and some polymer binder. Nowadays several different host material particles are used in the cathodes. The most common ones are transition metal oxides e.g. $LiMn_2O_4$, $LiCoO_2$, $LiNiO_2$, which can reversibly store a lithium equivalent of roughly $150\,mAh/g$ and are operated at a potential range of 3 to 4.5 V vs. Li/Li^+. Recently $LiFePO_4$ has become more popular in lithium-ion batteries, because it offers a significantly higher power density and higher energy storage efficiency at only slightly lower capacities. For the anodes, almost all currently available lithium-ion batteries use graphite, which can reversibly store 1 lithium atom per 6 carbon atoms corresponding to a specific capacity of $340\,mAh/g$ (in the charged state). Lithium uptake and release appears in the range of 0 to 0.3 V vs. Li/Li^+. The electrolytes used in commercial lithium-ion batteries are very diverse. Typically they consist of mixtures of organic solvents, e.g. ethylene carbonate, diethyl carbonate, dimethyl carbonate etc., that contains a lithium salt e.g. $LiPF_6$, $LiAsF_6$. In some cases also Lithium ion conductive polymers are used. For the current collector at the anode side of the electrode it is very common to use copper, whereas at the cathode side aluminium is typically used. Finally there is the separator, a porous, non conductive foil, which is typically made from polyethylene or polypropylene.

One of the most difficult challenges for future lithium-ion batteries is to further increase the energy

density. In principle there are two possibilities to create batteries with a higher energy density. The first one is to increase the operating voltage and the second one is to increase the capacity of the battery. Increasing the operating voltage is currently limited by the electrolyte which do not offer a higher potential window, whereas the energy density is at the moment mainly limited by the specific capacity of the electrode materials especially of the cathode material. Replacing currently used graphite anodes by the theoretically superior metallic lithium (specific capacity of roughly 3800 mAh/g), while sticking to currently used cathode materials, would increase the specific capacity of the battery by less than 40%. If on the other hand sulphur, which is one of the most prominent alternatives for the cathode, is used as the cathode material the theoretical energy density can be increased by more than 500% when swiching from carbon to metallic lithium anodes. In the recent past several studies showed well performing lithium sulphur cathodes. Hence the demand for anode materials with higher capacities than graphite is increasing as well.

Even though it is theoretically superior to all alternatives, the usage of metallic lithium for hundreds of cycles in secondary (rechargeable) lithium batteries has considerable safety issues and lacks cycling stability [4]. Therefore focus has been put to materials that are able to store higher amounts of lithium than carbon. There are numerous possible materials (see [5, 6]) that can store lithium at intercalation sites or form alloys with it. Especially some of the alloy electrodes show very promising results. One very prominent example is silicon, which is able to store up to 4.4 lithium atoms per silicon atom [5] corresponding to a specific charge of about 2000 mAh/g. The drawback of alloy anodes is the huge volume change that appears during lithiation (lithium uptake) which can reach several 100% (in case of silicon 323% [5]). Such a huge change in volume induces considerable problems with regard to the stability of the electrode like crack formation, delamination or pulverisation [6]. It is expected, that these mechanical failure mechanisms are the limiting factor for the cycling stability of alloy electrodes [6]. To overcome these problems, the introduction of nanostructured electrode materials seems to be a promising attempt, because the diffusion length is reduced and the deformation is facilitated, which reduces the stress and stress gradients during lithiation and delithiation [7].

Additionally to reducing bulk stresses, the introduction of nanostructures strongly increases the impact of the surface. This includes surface stress, surface tension, as well as the electrocapillary effect. The impact can be in such a way that it increases the stability of electrode particles by counteracting the diffusion induced stress [8] or by reducing the maximum tensile stress [9], on the other hand it can increase the radial tensile stress in hollow particles and therefore promote failure at the inner surface [9] and in this way reduce the cycling performance of electrodes, making it important to understand and measure these effects. Investigating the coupling of electrochemistry and mechanics can be done either by measuring the change in electrode potential upon elastic deformation or by measuring electrochemically induced stresses. Both effects are correlated to each other, as will be discussed in chapter 3. In literature some studies can be found that investigate electrochemically induced stresses in lithium alloy electrodes. Among them there are studies measuring the stress evolution upon electrochemical cycling of silicon [10], tin [11] and gold [12] electrodes by using a substrate bending method. Unfortunately substrate bending experiments are sensitive to surface and bulk effects in a similar manner, hence the aforementioned studies are not able to directly separate surface and bulk effects. Another study by Nadimpalli *et al.* estimates the electrocapillary effect by investigating the stress evolution in copper thin films. The authors associate instantaneous changes of the cantilever curvature to the electrocapillary effect and all other changes the formation of the solid electrolyte interface (SEI). Their result indicates a surface stress of -2 N/m upon charging and -24 N/m upon the formation of the SEI. It has to be mentioned, that lithium and copper do form a substitutional solid solution for lithium concentration of up to $\approx$ 15%, hence the values are not fully trustworthy. In fact, results of the thesis show the existence of a bulk effect in gold thin films which is able to promote similar "instantaneous" changes of the substrate bending and there are indications, that the same effect is active in copper thin film electrodes.

Regardless of the high amount of research spent on lithium-ion batteries, the interactions of electrochemistry and mechanics is not fully understood for lithium alloy electrodes. The importance of this coupling was shown e.g. by Gao and Zhou [13], who evaluated the impact of the electro-chemo-mechanical coupling on the formation of cracks or by Biener *et al.* who showed the impact of the electrocapillary effect on the macroscopic dimensions of nanoporous gold[14]. Hence it is an important aspect, worth looking into. The fact that surface and bulk stresses appear at the same time and that both interact with the chemical potential, were the motivation for developing a method to separate both contributions. This is important, because both contributions are potentially critical for the cycling stability, but depend differently on the sample geometry. The impact of the surface stress increases with decreasing particle size, whereas the bulk stress tends to decrease with decreasing particle size.

For investigating the coupling of electrochemistry and mechanics, dynamic electro-chemo-mechanical analysis (DECMA), which directly measured the potential strain coupling parameter, was chosen. This method offers the possibility to measure the potential strain coupling parameter (PSCP) at an almost arbitrary frequency, independent from the characteristic time for cycling. Especially in lithium electrolytes, which are electrochemically unstable with respect to lithium and typical lithium anodes, the choice of characteristic time can have the advantage of reducing the impact of decomposition processes.

DECMA alone is not sufficient for separating surface and bulk contributions, because by design it does not distinguish surface and bulk effects. Hence a method for separating real and apparent surface stresses changes was required, and a strategy was developed. This strategy is based on the interplay of the PSCP with the tilting angle dependent lattice parameter. With this strategy it became possible to separate surface and bulk contributions to the PSCP as well as estimating the real and apparent surface stress changes upon electrochemical cycling.

For being able to apply the measurement strategy, a DECMA stage suitable for operation inside a glovebox with lithium electrolyte and an in-situ electrochemical cell were required. Design and test results of both devices is shown in section 5.2. The interrelation of the results of both measurements is calculated according to a model of the electrode. With this model it was possible to separate surface and bulk contributions to the PSCP of a gold model electrode, showing, that the developed strategy actually works. Further analysis, of the results allowed to draw conclusions with regard to the bulk mechanism responsible for the stress generation.

Major parts of this thesis, including the main results were published in [15].

2 State of the art

2.1 The evolution of stress in thin films

Stress in thin films is a widely investigated subject. A detailed summary of the most important mechanisms, which this part is based on, can be found in [16]. Typically the stress in thin films evolves during film growth. In the following several possible mechanisms for stress evolution in polycrystalline thin films as discussed by Koch [16] will be outlined. Additionally short comments will be given on whether a similar mechanism could appear due to accretion of lithium in a flat polycrystalline gold film.

- Small-angle grain boundaries: During the formation of thin films, especially for films grown by columnar grains, many small angle grain boundaries can be found. The interatomic forces at the grain boundaries tend to close any existing gap and thereby strain the surrounding grains in tension. The magnitude of the effect depends inversely on the average grain size. No new small angle grain boundaries should form due to uptake of lithium, hence no corresponding mechanism is expected to appear during electrochemical cycling.

- Domain walls: Domain walls are a special kind of grain boundaries, which appear e.g. for epitaxial Volmer-Weber systems. Volmer-Weber systems are systems where in the beginning of deposition small islands form that upon film growth grow together to form a film. Since the position of the islands is fixed by the substrate, coalescing islands may be improperly spaces. Atoms closing the gap between the coalescing islands may obtain a higher number of nearest neighbour bonds by immersing in the respective deepest layer. A corresponding effect in average leads to a compressive stress. The gold films used in the thesis at hand are not grown in an epitaxial way, hence domains walls should not be present, hence no corresponding effect is expected.

- Recrystallisation process: Since recrystallisation typically leads to a reduction of defects it is accompanied by shrinkage of the stress free dimensions which is typically compensated by a tensile strain. During the investigation done in the thesis at hand no recrystallisation is observed hence a corresponding effect is not expected.

- The lattice expansion mechanism: The lattice expansion mechanism describes the vanishing of the surface stress upon growing together of islands. As long as islands are separated, the surface stress acts on them and typically induces a compressive stress. When islands grow together the surface vanishes, but some portion of the strain stays, because due to the adhesion to the substrate, relaxation is hindered. This effect is linked to the growing together of islands, hence no corresponding effect should appear during the measurements presented in this thesis.

- Impurities: During deposition it is possible, that impurities are incorporated in the film and induce strains. The investigations presented here are not linked to the growth of films, hence no corresponding effect is expected to contribute to the results.

- Misfit stress: Misfit stress appears for epitaxial growth of thin films. Since the lattice of the substrate and the lattice of the film are usually not identical, epitaxial growth typically requires the film to be strained at the interface. During the investigation done for the thesis at hand, no interface between two different crystals is formed, hance no corresponding effect is expected to influence the measurement.

- **Solid state reactions and/or interdiffusion:** Due to the contact of the thin film and the substrate, interdiffusion and solid state reactions are possible. Commonly interdiffusion and solid state reactions are accompanied by significant stress generation. The actual stress evolution due to both effects can be rather complex. For the system at hand, interdiffusion between substrate and sample are of no concern, but diffusion of lithium into the gold film has to be considered, whereas diffusion of gold out of the film is of no concern. Solid state reactions between gold and lithium are known to appear below a certain electrode potential but should not appear in the potential range under investigation.

- **Adatom Insertion into grain boundaries:** Another mechanism, which can induce stress in thin films during growth is adatom insertion. The increase of the surface chemical potential during deposition induces atoms to flow into grain boundaries and thereby induce a compressive stress in the film [17]. This stress relaxes when the deposition is interrupted. A similar chemical potential difference might exist for lithium gold films. At electrode potentials, where no solid state reaction is thermodynamically possible, the chemical potential within the grain boundaries might already allow lithium insertion. A corresponding effect would induce a compressive stress as well, but might not relax upon interrupting the deposition, because the chemical potential difference could persists.

2.2 The origin of stress in lithium alloy electrodes

The following part is based on a review on stress in lithium-ion battery electrodes by Mukhopadhyay and Sheldon [6]. An overview is shown in figure 2.1.

The source of stress can be either an internal stress or an external stress. An example for external sources is the packing. Since external sources are not of concern for the thesis at hand, they will not be discussed any further.

Internal sources on the other hand can be quite diverse. Many internal sources are correlated to volume changes upon lithiation and delithiation. An important source are physical constraints e.g. form current collectors, other host as well as inactive particles and the SEI. Additionally there is the diffusion induced stress due to changes of the lattice parameter with lithium concentration for lithiation in a single phase regime. In a two phase regime there is always a phase boundary which induces a mismatch stress, which is not related to the volume change. Besides lithiation induced stresses, also surface stresses do occur. Such surface stresses can for example be correlated to the SEI, the electrolyte or the deposition of e.g. lithium on the surface[1].

Depending on the mechanism different aspects define the magnitude of stress in the volume. For physical constraints the architecture of the electrode is very important. A porous electrode for example has much weaker physical constraints than a massive thin film on a substrate. Diffusion induced stresses typically depend on the rate of lithiation/delithiation, and the particle size of the host material. The phase boundary induced stress is mainly correlated to the mismatch of the phases and therefore the chemical composition. For surface stresses naturally the surface to volume ratio and the chemical composition of the surface as well as the SEI/electrolyte are the main impact factors. In general the stress resulting from either one of those sources is inhomogeneous throughout the electrode material and changes during cycling.

Surface stress changes in lithium-ion battery anodes are usually associated with the formation of the solid electrolyte interface [18, 12]. In case of gold electrodes underpotential deposition of lithium changes the surface stress as well [12]. Measurements by Tavassol *et al.* indicate a positive surface stress due to the SEI formation and a negative surface stress due to underpotential deposition of lithium on the gold surface [12].

---

[1]surface stresses are not considered in the review [6]
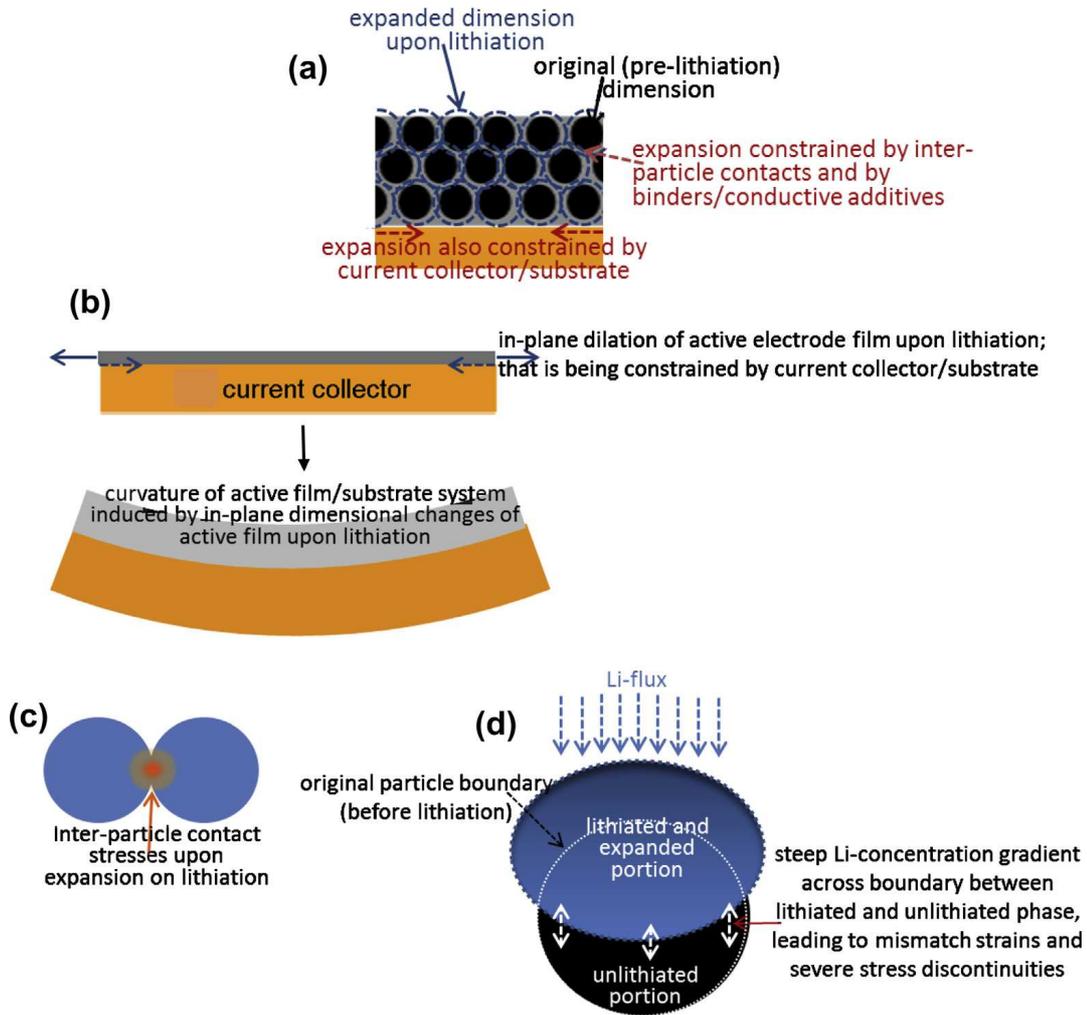
Figure 2.1: Illustration of sources of stress in lithium-ion battery electrodes by [6]. a) physical constraints in a typical electrode alignment with host material powder held together by carbon black and binder on a current collector. b) physical constraints in a thin film electrode on a current collector, c) inter-particle contact due to volume expansion, d) stress due to mismatch strains evolving during lithium induced phase transformations.

2.3 The interaction of electrochemistry and mechanics in lithium-ion electrodes

The interaction of electrochemistry and mechanics works in two ways. On the one hand, electrochemical cycling can induce stresses, on the other hand the elastic energy contributes to the chemical potential, visible by changes of the electrode potential upon changes of the stress. Both effects have been measured in literature.

Electrochemically induced changes of the surface stress (the electrocapillary effect) are typically measured by substrate bending experiments. When done properly, these measurements give quite precise values for changes of the surface stress as long as bulk effects do not contribute. Battery electrodes in general do not satisfy this requirement. Hence it is little surprising that for lithium-ion battery electrodes the electrocapillary effect has rarely been considered in experimental studies. A noteworthy exceptions is the work by Nadimpalli *et al.* [19] who estimated an upper bound for the electrocapillary effect for copper electrodes by measuring instantaneous changes of the substrate

bending upon applying potential steps.

For measuring bulk stresses due to the uptake of lithium most studies used substrate bending experiments as well. Such measurements provide values for a tangential stress, which, in contrast to measurements in most other electrochemical systems, are assigned to bulk effects. Consequently an electrocapillary effect would be a measurement error for such an interpretation.

In contrast to electrochemically induced stresses, only few studies investigate the elastic energy contribution to the electrode potential in lithium ion battery electrodes. One of them was done be Ichitsubo, who investigated lithium-tin electrodes. One of their findings was that in a two phase regime during lithiation of tin electrodes the elastic energy contribution to the electrode potential can be as high as 20 mV [20]. Another study by Sethuraman investigated the elastic energy contribution to the electrode potential of a lithium silicon alloy electrode by measuring the change in electrode potential upon mechanical relaxation. Their results indicate that the electrode potential changes for 100 to 125 mV/GPa of planar stress, depending on the state of charge. The observed stress levels are in the range of one GPa. Hence their study points towards an elastic energy contribution to the electrode potential of up to -125 mV [21]. The study by Ichitsubo [20] as well as the one Sethuraman [21] measure the electrode potential and, in case of Sethuraman, the planar stress during mechanical relaxation at a certain state of charge and draw there conclusions from relaxation induced changes of the electrode potential.

2.4 Literature results on the system under investigation

2.4.1 The gold-lithium system

In this work, thin gold films are used as model lithium alloy electrodes. In the following properties of the gold-lithium system are presented. Equilibrium crystallographic information of the gold-lithium system is summarised in the binary alloy phase diagram shown in figure 2.2. The binary alloy phase diagram contains several solid solutions as well as several intermetallic phases. At equilibrium gold and lithium form a substitutional solid solution for low lithium concentrations, whereas for lithium concentrations higher than $\approx 40\%$ intermetallic phases form. The crystallographic parameters of the different phases at room temperature are summarised in Table 2.1

Electrochemical reactions of gold electrodes in lithium-salt containing electrolyte can be diverse. The most common surface reactions were summarised by Aurbach *et al.* [24] and are displayed in figure 2.3. Electrochemical alloy formation of gold and lithium at room temperature was measured for example by Kulova *et al.* [25]. Some of their results are displayed in figure 2.4 and prove alloy formation at room temperature for films with a thickness of 200 nm.

Another investigation by Renner *et al.* [26] showed the formation of gold lithium alloys upon electrochemical alloying by high energy X-ray diffraction. Besides several not well specified phases also the α-Au-Li Phase was observed during alloy formation. Furhtermore it was observed, that upon alloy formation the crystal broke up to nano-crystals with a characteristic size of approximately 15 nm.

2.4.2 The electrolyte

In this work a 1 molar solution of $LiPF_6$ in a 1:1 mixture of ethylene carbonate (EC) and dimethyl carbonate (DMC) is used. This electrolyte is commercially available under the name LP30 and used in lithium-ion batteries. Both organic components are known for being reduced by lithium. The decomposition starts at a potential of 1.36 V for EC and 1.32 V for DMC vs. Li/Li^+ on gold surfaces [27]. Furthermore $LiPF_6$ is thermodynamically unstable, which can trigger several reactions. A list of possible reactions within this electrolyte can be found in [28]. Typical decomposition products are Li_2CO_3, $ROCO_2Li$, $(CH_2OCO_2Li)_2$, LiF and several others [28]. Most of these reaction products are
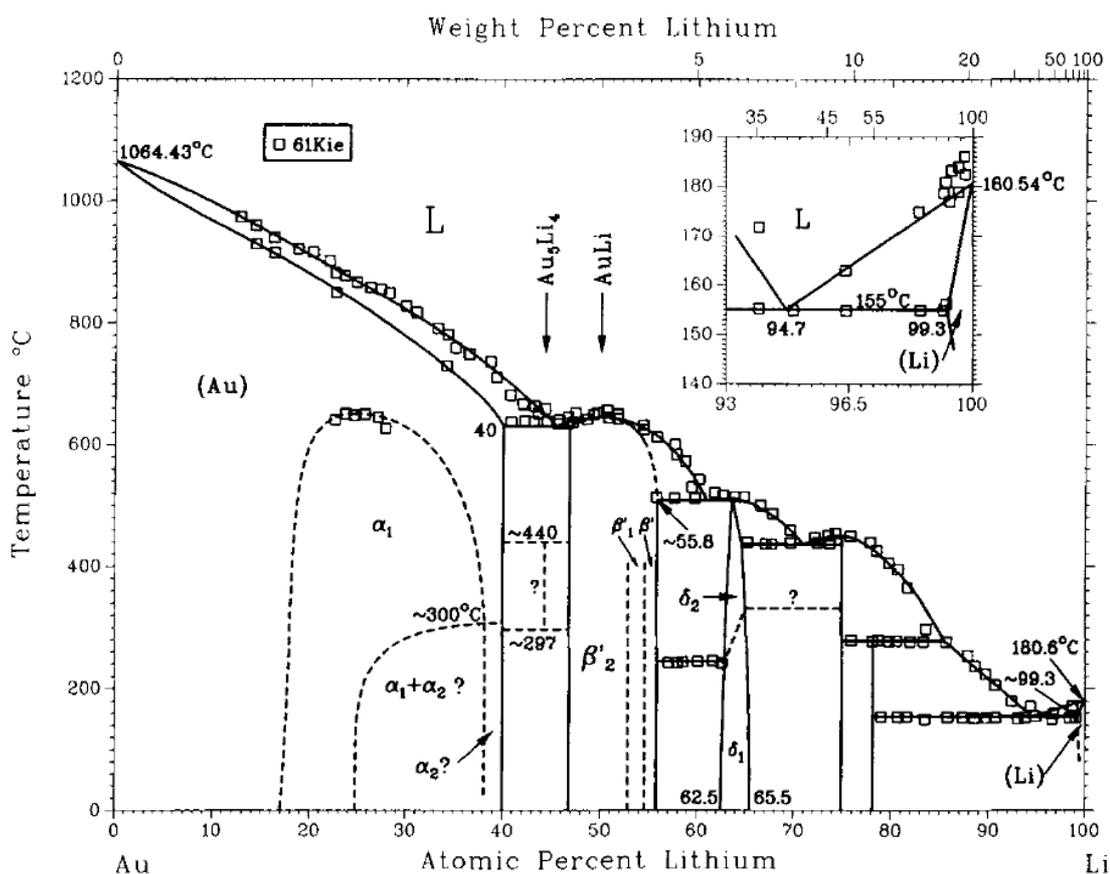
Figure 2.2: The Gold-lithium binary alloy phase diagram as measured by Kienast and Verma [22] and summarised by Pelton [23]. For lithium concentrations up to $\approx 40\%$ gold and lithium form a substitutional solid solution, where two ordered phases may occur. For higher lithium concentrations several intermetallic phases can be found. The single phase with the highest lithium concentrations is Au_4Li_{15}. A list of all room temperature phases can be found in table 2.1. Graphic after [23]

solid under ambient conditions and to some extent soluble in EC and DMC [29]. Regardless of the complexity of the decomposition reaction, the electrode surface is passivated after a certain time by the reaction products, which form a sufficiently stable and lithium ion conductive solid electrolyte interface.

2.5 Grain boundary reactions

Grain boundaries are of significant interest for several aspects associated with lithiation and delithiation. In the following some properties of grain boundaries, which are important for the thesis at hand, are introduced.

It is well established that the diffusion in grain boundaries can be several orders of magnitude higher than diffusion within the ordered lattice, where less oriented grain boundaries, i.e. non-specific high angle grain boundaries, typically allow higher diffusion rates [30]. Consequently grain boundaries will increase the kinetics of lithiation especially in the single phase regime, where no phase boundaries are present.

Table 2.1: Gold-lithium phases and crystallographic properties as measured by Kienats and Verma [22].

Phase	% Li	Pearson Symbol	Prototype	a (Å)	b (Å)	c (Å)
Au	$0 \rightarrow 17$	cF4	Cu			
Au	0	cF4	Cu	4.0784	...	...
Au	15.8	cF4	Cu	4.043	...	...
Au	39.2	cF4	Cu	3.968	...	...
α_1	$17 \rightarrow 25$ [a]	cP4	$AuCu_3$			
α_1	33.8 [c]	cP4	$AuCu_3$	3.973	...	...
α_2 [b]	$39 \rightarrow 40$ [a]	Complex	...			
Au_5Li_4	44.4	Hexagonal	...	8.1	...	7.0
β_2'	$47 \rightarrow 53$ [a]	oP2	...			
β_2'	51.8	oP2	...	3.3	3.21	2.80
β_1'	$53 \rightarrow 55$ [a]	tP2	...			
β_1'	54	tP2	...	3.23	...	2.83
β'	$55 \rightarrow 56$	cP2	CsCl			
β'	55	cP2	CsCl	3.098	...	...
δ_1	$62.5 \rightarrow 65.5$	hP9	...	7.23	...	2.7(7)
$AuLi_3$	75	cF16	Cu_3Al	6.302	...	...
Au_4Li_{15}	79	cI76	$Cu_{15}Si_4$	10.833	...	...

[a] uncertain composition range
[b] uncertain existence
[c] measured in a potential two phase region

A study by Baulieu *et al.* could show that the capacity of a material with a low affinity for lithium can be increased significantly by reducing the grain size. Their conclusion was that the specific capacity of grain boundaries can be much higher than the specific capacity of the bulk phase [31]. This difference is especially important, in case the grain boundaries are the source of the stress. A corresponding indication is the finding that during physical vapour deposition grain boundaries can be a source of stress due to deposition of material into the grain boundaries [32]. The sum of these findings suggests to treat grain boundaries separately when discussing the coupling of electrochemistry and mechanics.

2.6 Devices used in literature

2.6.1 Measurement of the potential-strain coupling parameter

A common way for investigating the interaction of electrochemistry and mechanics are substrate bending experiments. In these experiments the bending of a stiff substrate (e.g. glass) is measured. The results obtained in such a way can be used to calculate a tangential stress, which is then either associated with a surface or a bulk stress. In case of pure surface reactions, the derivative of the surface stress with respect to the excess charge density gives a PSCP of the surface (also called electrocapillary coupling parameter) [33]. The typical time scale of this measurement is in the range of minutes to hours (the time for one cyclic voltammetry (CV) cycle).

A direct method for measuring the PSCP of the surface was introduced by Gokhshtein [34]; the so called "estance method". In this method the electrode potential is varied at a resonance frequency of a massive electrode and the magnitude of vibration is recorded with a piezo element. This resonance
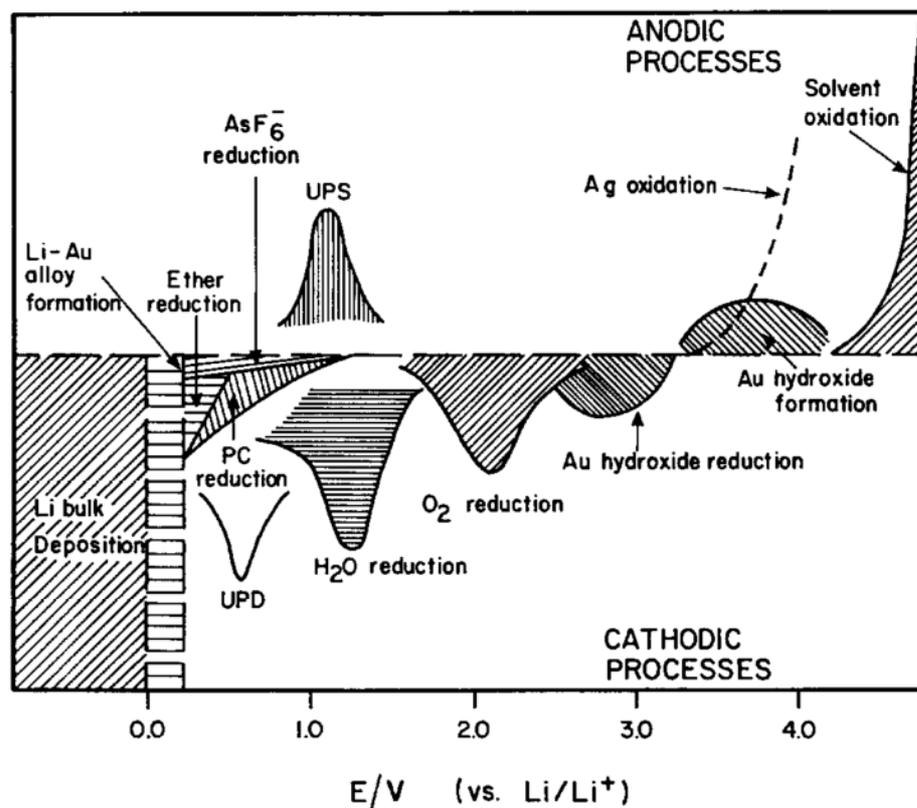
Figure 2.3: Potential features visible during electrochemical cycling of gold electrodes in lithium salt containing aprotic electrolytes. UPD stands for underpotential deposition and UPS for underpotential deposition stripping. Graphic from [24]

can be observed during electrochemical cycling and the results can be used to evaluate a potential dependent variation of the PSCP of the surface. By comparing the results to a reference signal, it should be possible to obtain absolute values for the PSCP of the surface. A drawback of this study is that it is not clear how the reference signal is obtained and that massive electrodes are required.

In the recent past a new setup was introduced by colleagues (some formerly) working in the group Institute of Materials Physics and Technology at the Hamburg University of Technology. This method uses the Maxwell relation presented in equation (3.8), which relates the change in electrode potential with strain to the change in surface stress with surface charge density. The device used by Smetanin *et al.* [35] as well as Deng *et al.* [36] is able to apply strain variations at a frequency of up to 100 Hz. The strain is evaluated from the measured elongation of the piezo actuator and the sample dimensions.

2.6.2 In-situ electrochemical cells used in literature

In-situ electrochemical cells for lithium-ion battery electrodes are widely used and are even commercially available. Commercial cells are typically designed for investigating electrodes consisting of host material powder mixed with carbon black and binder. Due to their design, such cells are not suitable for the measurements performed in this work, because they typically do not offer an arbitrary incidence angle or do not offer a sufficient fixation of the position of a thin film electrode.

A very interesting cell was designed by Renner *et al.* [26], which was used for investigations of thin films under gracing incidence in-plane diffraction conditions using high energy synchrotron radiation. With this cell they were able to observe the evolution of several gold-lithium phases during
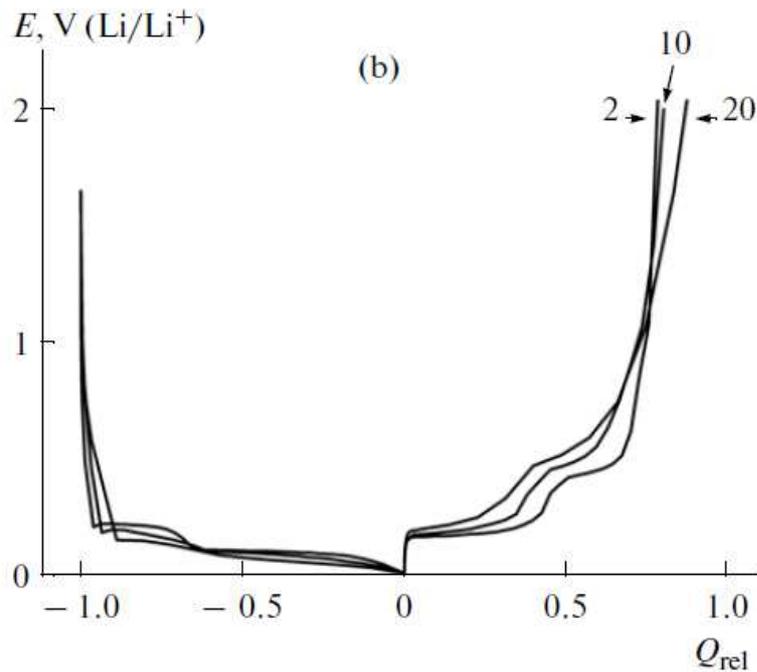
Figure 2.4: Electrochemical lithiation and delithiation curves of a 200 nm thick gold film measured at a constant current density of 33 $\mu A/cm^2$ in 1 molar $LiClO_4$ in a 7:3 mixture of propylene carbonate and dimethoxyethane measured by [25]. During lithiation all curves show a fast drop of the potential at the beginning, corresponding either to a single phase regime or purely capacitive charging. This drop is followed by two regions with almost constant potential, corresponding to phase transition regimes. The two regimes are separated by a short drop of potential corresponding to another single phase regime. During delithiation the behaviour is quite similar, but the potentials are shifted to higher values. Graphic copied from [25]

electrochemical lithiation. This cell was not copied, because it is not clear, whether their cell supports out-of-plane diffraction, whether diffraction with lower energy synchrotron radiation is possible and because the design is rather complex.

3 Theory

3.1 Electrochemistry

This section follows the book "Electrochemical methods Fundamentals and applications 2nd edition" by Allen J. Bard and Larry R. Faulkner [30].

Electrochemistry deals with the interrelation of electricity and chemistry. Many electrochemical studies investigate chemical changes due to the passage of current or chemically produced electrical energy. Major concerns in electrochemical systems are factors that contribute to the charge transfer across the electrode-electrolyte interface. This interface is where an electric current (in the electrode) is transferred into an ionic current (in the electrolyte).

3.1.1 The electrochemical cell and electrochemical reactions

Passage of currents requires an electric circuit. In terms of electrochemistry, this corresponds to an electrochemical cell, which consists of at least two electrodes and one electrolyte. These components are required in order to induce or measure an electric current or voltage in an electrochemical environment (see figure 3.1 left). Another consequence of the requirement of an electric circuit is that it is only possible to measure a potential difference (voltage) between two electrodes. The absolute electrode potential, the work required to bring a unit positive charge from infinitely far away into the interior of the electrode, can only be estimated. Therefore it is very common to measure the potential of the electrode of interest, the working electrode, with respect to an electrode with stable potential, the reference electrode. The usage of a reference electrode is typically done in a three electrode electrochemical cell as illustrated in figure 3.1 right. In case the current in the electrochemical cell is not vanishing, the electrochemical cell is called either galvanic cell (the reaction occurs spontaneously; e.g. battery during discharging), or electrolytic cell (the reaction is forced by an external power supply; e.g. battery during recharging).

Electrodes consist of materials that provide electronic conductivity via electrons or holes, like metals, carbon or semiconductors. Electrolytes on the other hand provide conductivity via ions, without electronic conductivity. The most common electrolytes are liquids containing ions (e.g. salts dissolved in solvents). Less common electrolytes include molten salts (e.g. ionic liquids), solid electrolytes and ionically conductive polymers.

At equilibrium the free charge carriers of the electrode and the electrolyte will prevent gradients of the electric potential in the bulk of the phase. As a consequence, the potential gradients are limited to the vicinity of the interfaces, which typically leads to high electric fields at the interface. It can be expected that these high electric fields affect the behaviour of charge carriers at the interface, making the interface one of the most interesting aspects of the electrochemial cell. Consequently most electrochemical experiments focus the reactions happening at one of the interfaces and their dynamics. In order to omit influences from the second interface on the measurement, the potential is measured again with respect to a reference electrode. In order to provide a constant potential of the reference electrode, it is built in such a way that the composition of the electrode and the surrounding electrolyte is stable. With this configuration it is provided that the absolute potential of the reference electrode does not change as well. There are different conventions for the sign of the currents measured during electrochemical experiments. In this work cathodic currents are taken negative and anodic ones positive (see
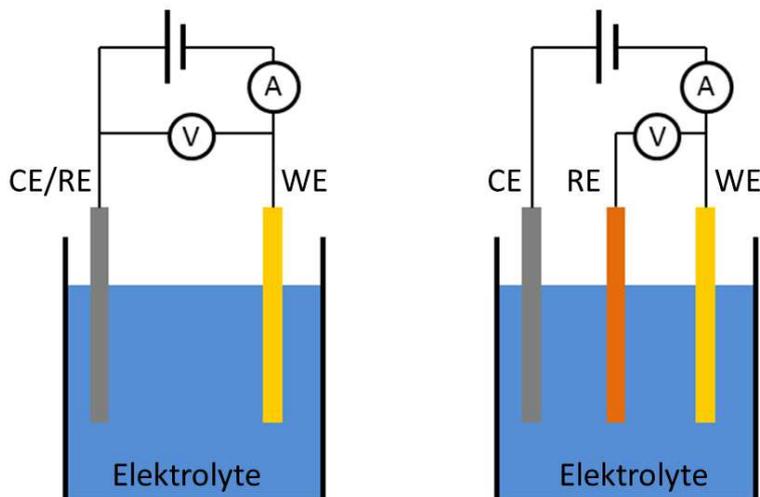
Figure 3.1: Left: Two electrode electrochemical cell, where the counter and reference electrode are the same electrode. Right: Three electrode electrochemical cell, with separate counter- and reference electrodes. The working electrode (WE) is typically the electrode of interest. Its electrode potential is measured against the reference electrode (RE). For electrochemical cycling a voltage is applied/current measured between the counter electrode (CE) and the working electrode.

figure 3.2).

The potential difference between the different phases (electrode/electrolyte) is a measure for the different electron energies. This difference in energy defines the direction and magnitude of the charge transfer across the interface. By controlling the electrode potential with respect to a reference electrode one controls the energy of electrons within the working electrode. Applying a more negative potential increases the energy of the electrons in the electrode. If the energy of the electrons in the electrode is lifted above the energy level of a vacant molecular orbital of a molecule in the electrolyte, electrons can pass the interface and reduce the molecule by occupying its vacant orbital. The resulting flow of electrons from the electrode to the electrolyte is called a reduction or cathodic current. In the opposite case, when the energy of the electrons in the electrode is reduced by shifting the electrode potential to more positive values, it can be dropped below the energy of an occupied molecular orbital of a molecule in the electrolyte. In this case the electron can "jump" from the molecular orbital to the electrode and oxidise the molecule by doing so. Such a flow of electrons from the solution to the electrode is called an oxidation or anodic current (see figure 3.3).

The number of electrons passing the interface is directly correlated to the number of atoms/- molecules that is reduced or oxidised. Since every electron carries a charge of $\approx 1.60 \cdot 10^{-19}$ C, the amount of consumed/generated reaction product (in moles) is correlated to the transferred charge by Faraday's law: 96485 C of electrons passing the interface leads to 1 mol of reaction product in a 1-electron process.

Besides processes that require electrons to pass the interface (Faradaic processes), nonfaradaic processes occur at the interface as well. They appear when electron transfer across the interface is unfavourable. Causes for nonfaradaic processes include e.g. adsorption and desorption reactions as well as changes of the electrode-electrolyte interface. In a potential range, where electrode reactions occur, faradaic and nonfaradaic reactions appear at the same time.
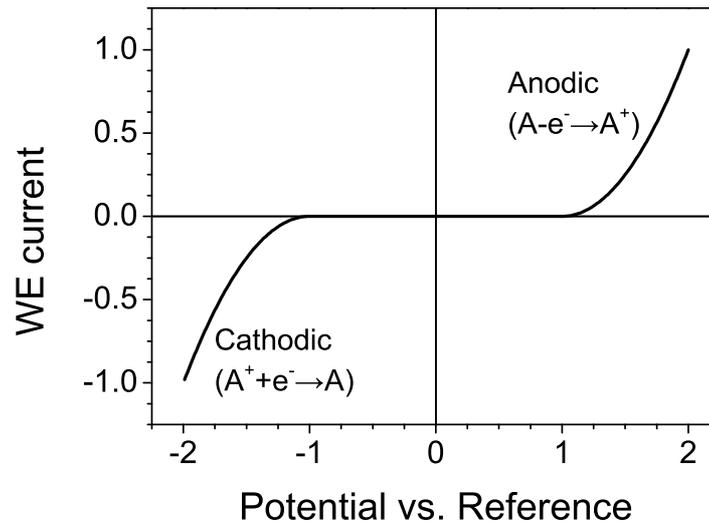
Figure 3.2: Schematic representation of steady-state cathodic and anodic currents according to the sign convention used in this work. (Inverse to the one used in [30])

3.1.2 Reaction rates

Electrode processes happen at the electrode-electrolyte interface. Hence the reaction rate typically depends on the surface area of the electrode [30]:

$$\text{Rate} = \frac{i}{n_e F} \tag{3.1}$$

where i is the current density and n_e is the stoichiometric number of electrons involved in the reaction.

This reaction rate is governed by several contributions:
- Mass transfer to/from the interface
- Electron transfer to the surface of the electrode
- Electron transfer across the interface
- Chemical reactions following the oxidation/reduction reaction
- Other surface reactions (e.g. adsorption, desorption)

Any current in an electrochemical cell is correlated to an electric field configuration which differs from the current free case. A common simplified representation of an electrode reaction is done by an equivalent circuit, where every reaction step has its own impedance. In general these impedances depend on the electric field as well as the current density. A further simplification can be made by taking the impedance constant for small deviations of the electric field.

3.1.3 The electrical double layer

A common model for the solution side of the electrode-electrolyte interface in liquid electrolytes (excluding molten salts) is that it consists of several "layers". The layer closest to the electrode surface is called the inner Helmholtz plane (IHP). Only specifically adsorbed ions and solvent molecules are able to approach the electrode as close as the IHP. Solvated ions, on the other hand are surrounded by solvent molecules, which prevents these ions from approaching the electrode further than a certain distance. The plane formed by this distance from the electrode surface is called the outer Helmholtz
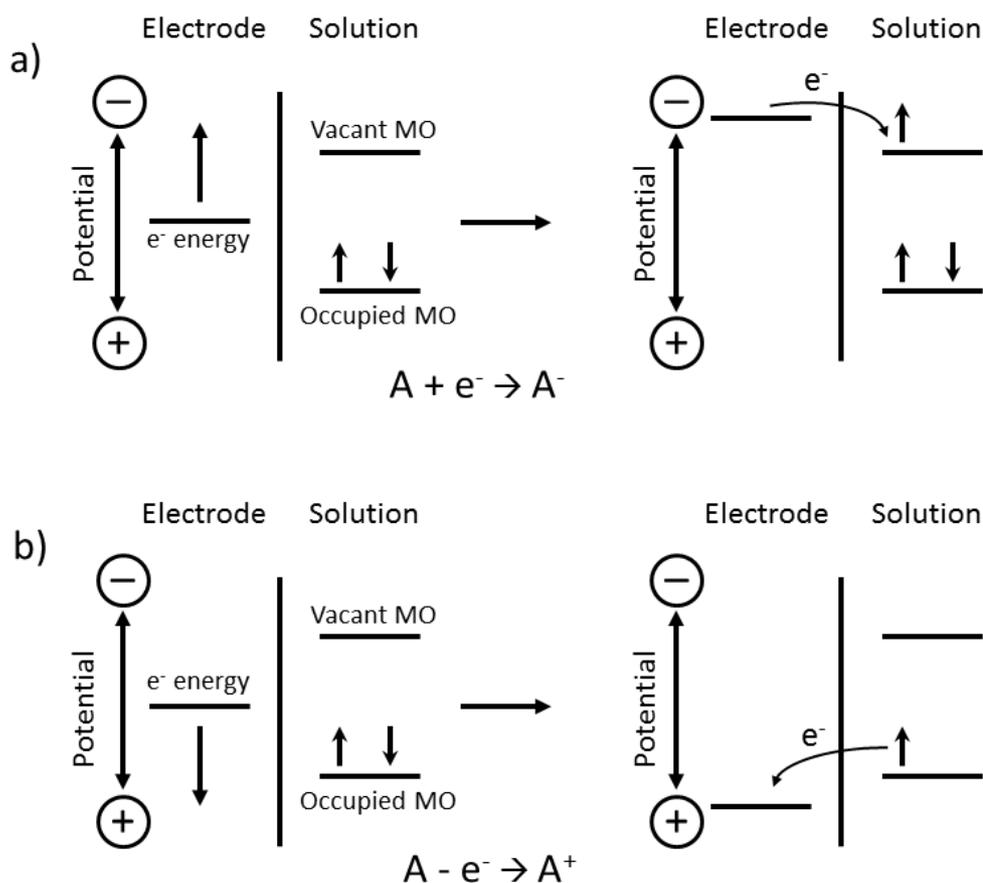
Figure 3.3: a) electronic representation of a reduction process of species A in solution; cathodic current. The electron energy is lifted above the energy level of the lowest vacant molecular orbital of a molecule in the solution, which leads to an electron transfer from the electrode to the vacant molecular orbital. b) oxidation reaction of species A in solution; anodic current. The electron energy in the electrode is reduced below the energy of the highest occupied molecular orbital of a molecule in the solution, which leads to a passage of electrons from the solution to the electrode. Graphic adapted from [30]

plane (OHP). Finally, the layer reaching from the OHP to the bulk of the solution is called the diffuse layer. An important magnitude of the layers is the charge they carry per area of the interface, the excess charge density. This electrolyte excess charge density sums up the charge density of the IHP q^i and the diffuse layer q^d, which includes the OHP. At equilibrium the excess charge density on the electrolyte side q^s is compensated by an excess charge density on the electrode side of the interface q^m:

$$q^s = q^i + q^d = -q^m \tag{3.2}$$

3.1.4 Reversibility

"'Reversible"' has several meanings in electrochemistry. In the thesis at hand the definitions of Bard and Faulkner [30] are used, who distinguish Chemical reversibility, thermodynamic reversibility and
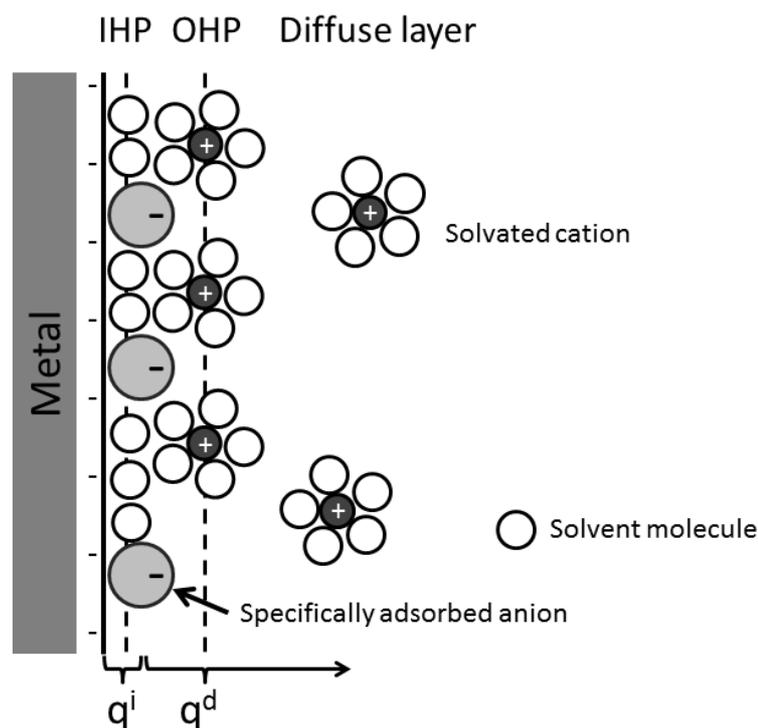
Figure 3.4: Model of the interface for specifically absorbed anions at the inner Helmholtz plane (IHP) and solvated cations in the outer Helmholtz plane (OHP) as well as in the diffuse layer. q^{i} represents the surface charge density of the IHP and q^{d} the surface charge density of the diffuse layer. Figure adapted from [30]

practical reversibility.

Chemical reversibility: Chemical reversibility denotes that upon reversing the cell current the cell reaction reverses and no new reactions occur. (Reversible reactions typically means chemically reversible reactions [1].)

Thermodynamic reversibility: Thermodynamic reversibility denotes a process that upon infinitesimal reversal of a driving force causes a reversal of the reaction. Such reversibility would require an infinite amount of time. Hence thermodynamic reversibility is only used for theoretical assumptions.

Practical reversibility: Practical reversibility denotes a process that is carried out close enough to thermodynamic equilibrium so that thermodynamic equations apply with a desired accuracy. (It can be regarded as the experimental equivalent of thermodynamic reversibility [1].)

3.2 Thermodynamics of electrodes

The thermodynamic description of an electrochemical cell presented in this section is based on "'Electrocapillarity of Solids and its Impact on Heterogeneous Catalysis'" of "'Electrocatalysis; Theoretical Foundations and Model Experiments, Volume 14'" [33], the study "Balance of Force at Curved Solid Metal-Liquid Electrolyte Interfaces" by Weissmüller and Kramer [37] and the theory on the thermochemical equilibrium of linear elastic solids under stress which was introduced by Larché and Cahn [38].

In order to investigate electrochemical reactions it is meaningful to describe the electrochemical

---

[1] Author's comment

half cell consisting of the electrode of interest and the surrounding electrolyte up to a distance far enough from the electrode surface to provide that the diffuse layer is fully included in the half cell, independent on the state of the electrode. The controllable variables of the system are the external pressure and the temperature, both of which are held constant, the strain of the electrode and the charge transfer to the electrode.

Since the temperature is held constant, the thermodynamic potential of choice is the free energy $\mathscr{F}$. In order to investigate surface reactions, it is meaningful to treat the electrode surface separately. Consequently the surface is neither part of the electrode bulk nor of the electrolyte. Hence the free energy $\mathscr{F}$ of the half cell can be written as:

$$\mathscr{F} = \mathscr{F}_{\text{L}} + \mathscr{F}_{\text{I}} + \mathscr{F}_{\text{B}} \tag{3.3}$$

where $\mathscr{F}_{\text{L}}$ is the free energy of the electrolyte, $\mathscr{F}_{\text{I}}$ is the free energy of the interface and $\mathscr{F}_{\text{B}}$ is the free energy of the electrode bulk. Since the only controllable non constant variables of the system are the charge and the strain of the electrode, the free energy of the system at thermodynamic equilibrium can only depend on those two varables: $\mathscr{F} = \mathscr{F}(Q, \varepsilon_{ij})$.

In order to account for inhomogeneities within the phases, free energy densities are used, so that the free energy of the half cell can be written as[39]:

$$\mathscr{F} = \int_{\text{L}} \Psi_{\text{L}} dV_{\text{L}} + \int_{\text{B}} \Psi_{\text{B}} dV_{\text{B}} + \int_{\text{S}} \psi dA_{\text{S}} \tag{3.4}$$

where Ψ_{L} is the free energy density of the electrolyte, Ψ_{B} is the free energy density of the electrode bulk, ψ is the surface free energy density (per area) of the electrode surface. V_{B}, V_{L} and A_{S} are the volume of the bulk, the volume of the liquid and the surface area of the electrode respectively. In this theory elastic deformation is explicitly allowed. When measured in laboratory coordinates, elastic deformation changes densities without rearranging the lattice. In order to omit this change in densities it is meaningful to measure all values of the solid phases in a reference state. The corresponding coordinates are called Lagrangian coordinates.

For further evaluations it is assumed, that the electrolyte is a liquid electrolyte. Consequently the solid-electrolyte interface (SEI), which typically forms on the surface of the anode in the system under investigation is only accounted for as a potential source of surface stress. A further description of the SEI is beyond the scope of this thesis. Additionally it will be assumed, that the temperature is constant while the external pressure is assumed zero, hence $s\partial T = 0$ and dependencies on the external pressure as described in [37] are not included in this evaluation. Under these assumption $\Psi_{\text{L}} = \Psi_{\text{L}}(\rho_i)$, where ρ_i are the densities of the components i in the electrolyte. The free energy of the bulk electrode $\Psi_{\text{B}} = \Psi_{\text{B}}(\rho_{i,e}, \varepsilon_{ij})$ and the surface free energy density can be written as $\psi = \hat{\psi}(\Gamma_i, \mathbb{E})$, where $\mathbb{E}$ is the tangential elastic strain tensor at the surface of the electrode and Γ_i is the superficial excess per area measured in Lagrange coordinates of species i, which includes adsorbed atoms/ions as well as extra ions in the diffuse layer.

In order to evaluate the interaction of electrochemistry and mechanics in more detail, it is meaningful to treat surface and bulk mechanisms independently and to evaluate their dependency on each other in a later stage. Since this last step, evaluating the interaction of electrochemistry and mechanics due to surface and bulk effects, was done by the author of this thesis, it is presented discussed in a later part of this thesis (see section 4.2).

3.2.1 The electrocapillary coupling

The electrocapillary coupling describes the interaction of electrochemistry and mechanics for surface mechanisms. For this evaluation it will be assumed, that the bulk electrode is inactive and that no

exchange of matter with the bulk is possible. Furthermore it is assumed, that the chemical potentials μ_i are constant for any given state of strain, which provides, that Γ_i and the surface charge density q are montonous functions of the electrode potenital E. Under these assumptions the free energy of the surface $\hat{\psi}(\Gamma_i, \mathbb{E})$ can be written as $\hat{\psi}(\Gamma_i, \mathbb{E}) = \overline{\psi}(q, \mathbb{E})$. Hence the fundamental equation of the surface free energy can be written as:

$$\mathrm{d}\overline{\psi} = E\mathrm{d}q + \mathbb{S}\mathrm{d}\mathbb{E} \tag{3.5}$$

where $\mathbb{S}$ is the surface stress tensor.

A further simplification can be made for surfaces with a sufficiently high (threefold or higher) symmetry, for which the surface stress is isotropic [40]. This requirement is satisfied e.g by (111) oriented surfaces. In this case $\mathbb{S}\mathrm{d}\mathbb{E} = f\mathrm{d}e$ where $\delta e = \delta \tilde{A}/\tilde{A}$ equals the change in physical surface area $\tilde{A}$ and $f = \mathrm{Tr}\mathbb{S}/2$ is the scalar surface stress. In this case the fundamental equation simplifies to [39]:

$$\mathrm{d}\psi(q, e) = E\mathrm{d}q + f\mathrm{d}e \tag{3.6}$$

This fundamental equation can be used to derive a Maxwell relation, which interrelates the change in electrode potential with elastic strain to the change in surface stress with superficial charge density [39]:

$$\frac{\partial^2 \psi}{\partial e \partial q} = \frac{\partial^2 \psi}{\partial q \partial e} \tag{3.7}$$

which corresponds to [39]

$$\left.\frac{\mathrm{d}f}{\mathrm{d}q}\right|_e = \left.\frac{\mathrm{d}E}{\mathrm{d}e}\right|_q := \varsigma^{\mathrm{s}} \tag{3.8}$$

where ς^{s} is the PSCP of the surface (also referred to as the electrocapillary coupling parameter). For a process of electrosorption of one species the change in superficial excess of the species and the superficial charge density are correlated by: $\mathrm{d}q = -zF\mathrm{d}\Gamma$. For this case ς^{s} can be written as [39]:

$$\varsigma^{\mathrm{s}} = \frac{-1}{zF}\left.\frac{\mathrm{d}f}{\mathrm{d}\Gamma}\right|_e \tag{3.9}$$

3.2.2 The dynamic electro-chemo-mechanical analysis

The dynamic electro-chemo-mechanical analysis (DECMA) is a method to directly measure $\left.\frac{\mathrm{d}E}{\mathrm{d}e}\right|_q$. For this purpose an electrode is strained cyclically with time t so that:

$$e = \hat{e}\sin(\omega t) \tag{3.10}$$

where $\hat{e}$ is the amplitude of strain and ω is the circular frequency. For an ideally polarisable electrode at open circuit conditions this leads to a variation of the electrode potential according to [39]:

$$E = \hat{E}\sin(\omega t) = \varsigma^{\mathrm{s}}\hat{e}\sin(\omega t) \tag{3.11}$$

where $\hat{E}$ is the amplitude of potential variation. This correlation can now be used to evaluate ς^{s}

3.2.3 The electro-chemo-mechanical coupling of the bulk

In this part, the interaction of electrochemistry and mechanics is discussed at the absence of surface mechanisms. As mentioned earlier, the electrode bulk is charge free, hence uptake of ions from the electrolyte requires the uptake of charge in order to preserve charge neutrality:

$$0 = \mathrm{d}Q_{\mathrm{B}} + z_i F\mathrm{d}N_i \tag{3.12}$$

where N_i is the number of ions of species i entering the bulk and Q is the net electronic charge transferred to the bulk. The sum convention (summing up over indices occurring twice) is used throughout this thesis. At equilibrium the mean driving force for the migration of ions in the whole electrolyte has to vanish. Consequently the change in electrode potential due to elastic strain is linked to a change of the chemical potential [39] according to:

$$\frac{d\mu_{Act}}{d\varepsilon_{ij}} = -Fz \left. \frac{dE}{d\varepsilon_{ij}} \right|_{\varepsilon_{kl \neq ij}} \tag{3.13}$$

where μ_{Act} is the chemical potential of the active material (Active material refers to the ions/atoms that can pass the electrode/electrolyte interface.).

The impact of stress on the chemical potential in liner elastic solids was discussed by Larché and Cahn who distinguished two different cases: Substitutional and interstitial binary alloys. The difference between substitutional and interstitial binary alloys as discussed by Larché and Cahn are twofold. The first difference is the solubility. For the interstitial solid solution the theory requires that only one component is soluble, while for the substitutional solid solution it is presumed, that both components are soluble. The second difference is the way the strain state is measured. For the interstitial solid solution, the strain is a measure for the deviation of the lattice of the insoluble material from the reference state, while for the substitutional solid solution the strain (in the following called lattice strain) measures the deformation of the mathematical lattice, where every lattice place can be occupied by either component (neither replacing atoms nor addition of lattice places corresponds to strain for this definition). A consequence of those two definitions is, that the dependency of the chemical potential on the stress differs for both cases. For the interstitial solid solution at constant temperature it is [38]:

$$\mu_{int}(\rho_{Act}, \sigma_{ij}) = \mu_{0,int}(\rho_{Act}) - \frac{\partial \varepsilon_{ij}^{sf}}{\partial \rho_{Act}} \sigma_{ij} - \frac{1}{2} \left(\frac{\partial C_{ijkl}}{\partial \rho_{Act}} \sigma_{ij} \right) \sigma_{kl} \tag{3.14}$$

where $\mu_{0,int}(\rho_{Act})$ is the chemical potential of the active material in the reference state, ρ_{Act} is the density of the active material and C_{ijkl} is the usual compliance tensor.

For the substitutional solid solution, where both components are soluble, the density of each component depends on the chemical potentials of both components. This is because every lattice place can be occupied by any of the two species. Hence it is meaningful to define an "exchange potential" μ_{ex}, which is defined by [38]:

$$\mu_{ex} = \left(\frac{\partial \Psi_B}{\partial \rho_1} \right)_{\rho_2, T, \varepsilon_{ij}} - \left(\frac{\partial \Psi_B}{\partial \rho_2} \right)_{\rho_1, T, \varepsilon_{ij}} \tag{3.15}$$

where the ρ_i are the concentrations of component i. This exchange potential depends on the stress according to [38]:

$$\mu_{ex}(\rho_1, \sigma_{ij}) = \mu_{0,ex}(\rho_1) - \frac{\partial \varepsilon *_{ij}^{sf}}{\partial \rho_1} \sigma_{ij} - \frac{1}{2} \left(\frac{\partial C_{ijkl}}{\partial \rho_1} \sigma_{ij} \right) \sigma_{kl} \tag{3.16}$$

where $\varepsilon *_{ij}^{sf}$ is the lattice strain. This equation states, that the exchange chemical potential depends on the stress in a similar way than the chemical potential of the active material in an interstitial solid solution.

It has to be emphasised, that the case for a binary substitutional solid solution is independent on the number of lattice sites and therefore the overall volume. Hence the energy for changing the number of lattice sites is not included in this evaluation. Consequently equation (3.16) is not suitable

for describing the chemical potential of a substitutional alloy, when the concentration is linked to the number of lattice places and the energy for creating a new lattice place is not vanishing.

3.2.4 The potential-strain coupling parameter of the bulk

A theory on the change in electrode potential with elastic strain for interstitial uptake of active material has been developed by Viswanath and Weißmüller [41]. They used the palladium hydrogen system as a model system. For this system two cases have to be distinguished. The first one is adsorption in a thin superficial layer, and the second one is homogeneous bulk absorption. For both cases a PSCP was calculated, where the one for adsorption is called electrocapillary coupling parameter and the one for absorption is the apparent electrocapillary coupling parameter.

For evaluating the PSCP of the bulk, first the stress free strain, and in a second step a surface stress, which promotes an equivalent strain was calculated. From the dependency of this equivalent surface stress on the amount of hydrogen, which is correlated to a charge transfer, the PSCP for superficial adsorption and bulk absorption was obtained. The main difference between adsorption and absorption are the different physical constraints. For the superficial adsorption the strain parallel to the surface ($\varepsilon_\parallel$) and the stress normal to the surface ($\sigma_\perp$) are taken as constant, whereas for bulk absorption, all strains are taken constant. Under these constraints, the corresponding PSCPs can be calculated by [41]:

$$\varsigma^{\text{ab}} = \frac{9K\widehat{\eta}\Omega}{2zq_0} \tag{3.17}$$

$$\varsigma^{\text{ad}} = \frac{3K\widehat{\eta}\Omega}{zq_0}\frac{1-2\nu}{1-\nu} \tag{3.18}$$

where the PSCP of superficial adsorption is ς^{ad} and the one for bulk absorption ς^{ab}. K and ν are the bulk modulus and the Poisson's ratio of the sample, z is the valency of the active material[1], q_0 is the elementary charge and $\widehat{\eta}$ is the strain-concentration coefficient defined by $a = a_0(1 + \widehat{\eta}N_{\text{active}}/N_{\text{host}})$, where N_{active} is the amount of active material (Hydrogen) and N_{host} is the amount of host material (Palladium).

In the Appendix it is shown, that for an isotropic material in the stress free state, the right hand side of equation (3.18) equals:

$$\frac{3K\widehat{\eta}\Omega}{zq_0}\frac{1-2\nu}{1-\nu} = -\frac{1}{Fz}\frac{\mathrm{d}\mu_{\text{int}}}{\mathrm{d}(\varepsilon_{11}+\varepsilon_{22})}\bigg|_{\sigma_{\text{ij}}=0} \approx -\frac{1}{Fz}\frac{\mathrm{d}\mu_{\text{int}}}{\mathrm{d}(\varepsilon_{11}+\varepsilon_{22})} \tag{3.19}$$

The approximation is exact in case the compliance values are independent on the concentration $\partial C_{\text{ijkl}}/\partial\rho_{\text{Act}} = 0$ On the other hand, when the material is not in the stress free state, an additional term appears, which is proportional to the stress and the change in compliance values with active material concentration. This dependency will be discussed in more detail in 4.1.1.

3.3 Lithium alloy electrodes

This part is based on the chapter "Lithium Alloy Anodes" of "Handbook of Battery Materials: Second Edition" [4] The parts on diffusion are based on chapter 5 of the book "Physical metallurgy, 5th edition" by Balogh and Schmitz [42].

Lithium alloy electrodes are treated as one of the most promising anode materials for future generations of lithium batteries. Their main advantage is that they offer a solid matrix, which prevents

---

[1]The original version of the formula does not contain z, because it was set to the valency of hydrogen, which is 1.

shape changes of the anode (an important drawback of lithium metal anodes) and still offer a very high specific as well as volumetric capacity at a low potential vs. Li/Li$^+$.

At thermodynamic equilibrium the electrode potential follows the Gibbs phase rule. This phase rule states that the electrochemical potential changes with composition in a single-phase region and is constant in a two-phase region, as long as temperature and pressure are constant.

3.3.1 Crystallographic aspects

The incorporation of active material into a crystalline electrode at thermodynamic equilibrium can happen in two ways. Either by changing the composition in the pre-existing phase by solid solution or by the formation of a new phase, with a different structure. In many systems (e.g. the gold-lithium system under investigation in this thesis) single-phase as well as binary phase regions can be found. The formation of a new phase can be described as a reconstruction reaction. In this case the addition of active material goes along with the nucleation and growth of a new phase with a higher share of active material. If the two phases are locally at equilibrium, the composition of their mutual interface does not change during the reaction, hence the electrode potential is constant.

The second way how the active species can incorporate the host materials is interstitial insertion. In this case the active species is rather mobile and a single phase solid solution is formed. Furthermore it has been observed that in some systems substitutional solid solutions can form upon the uptake of active material [43]. This case mainly differs from the interstitial insertion case by the different diffusion mechanism with the consequence of significantly smaller diffusion constants. [2]

3.3.2 Kinetic aspects

Additionally to high capacities, the kinetics of electrode reactions need careful considerations as well. In lithium alloy anodes, the kinetics is typically governed by the diffusion of lithium into the host material. In crystalline structures, diffusion is based on point defects [42]. Two cases have to be distinguished: Diffusion of interstitial and diffusion of substitutional atoms. In case the solute atom (in electrochemical terminology: active material atom) is located at an interstitial site and the concentration of solute atoms is sufficiently low, the neighbouring interstitial site will be empty and the solute atom can easily "jump" to the next interstitial site. Due to elastic distortions from interstitial atoms usually only small atoms like hydrogen, oxygen or carbon occupy interstitial sites at thermal equilibrium. In metals and especially alloys it is more common that for low concentrations the solute atom occupies a lattice place to form a substitutional solid solution. In this case the typical diffusion mechanism is a vacancy mechanism.

A third, but very rare case is self-interstitial diffusion. It can only be observed in heavily deformed materials or after irradiation. In this case some host atoms occupy (thermodynamically unfavourable) interstitial sites and "push" atoms from a lattice place to a self-interstitial site.

The most simple case for describing diffusion assumes a dillute solution [42]:

$$\frac{\partial}{\partial x}\mu = \frac{\partial}{\partial x}(\mu_0 + k_\mathrm{b}T\ln c) \tag{3.20}$$

where k_b is the Boltzmann constant and T is the temperature. This case leads to Fick's first law [42]:

$$j = -D\frac{\partial c}{\partial x} \tag{3.21}$$

---

[2]The formation of a substitutional solid solution has not been considered in [4], besides the fact that some studies on lithium-magnesium and lithium silver alloy anodes can be found in literature, both of which form substitutional solid solutions in a wide potential range [43].

where j is the flux density of atoms, D is the diffusion coefficient, c is the concentration and x is the spacial coordinate. Adding driving forces other than entropy leads to the drift-diffusion equation [42]:

$$j = -D\frac{\partial c}{\partial x} + \frac{D}{k_b T}F \qquad (3.22)$$

where F can be any driving force. For uptake of active material it has to be considered, that the chemical environment enhances the diffusion. In order to account for this enhanced diffusion the chemical diffusion coefficient D_{chem} can be used, , which is related to the self-diffusion coefficient (D_{self}) by [4]:

$$D_{chem} = WD_{self}; \qquad W = \frac{d \ln \alpha_i}{d \ln c_i} \qquad (3.23)$$

where W is an enhancement factor, α_i and c_i are the activity and concentration of species i. This chemical diffusion coefficient can be quite high (e.g. 1.8 to 5.9 e-7 cm^{2}s$^-$1 in Li$_{4.4}$Sn at ambient temperature [4], in comparison to $\approx$5e-11 for Pb in Sn as estimated by [44]) and strongly dependent on the lithium concentration in lithium alloys.

3.3.3 Diffusion and microstructure

Structural defects in crystalline solids (e.g. dislocations and grain boundaries) often show enhanced diffusion. This enhanced diffusion is especially known in pure metals. In fact, the diffusion coefficient in dislocations and grain boundaries can be several orders of magnitude higher than the diffusion coefficient in the ordered regime, where the relative difference is becoming bigger at lower temperatures [42]. Due to the high diffusion coefficient, defects in some cases allow short circuit transport of atoms.

Additionally the equilibrium of active material concentration at grain boundaries and dislocations typically differs from the equilibrium concentration within the ordered lattice. In case the diffusion coefficient is concentration dependent, this difference contributes to the difference in the chemical diffusion coefficient as well.

3.4 X-ray diffraction

This section is based on the book "X-ray diffraction" by B.E. Warren [45]. Even though x-ray scattering does not follow classical electrodynamics, unmodified scattering (wavelength is conserved) is described well by classical theory. The theory presented in this section is based on classical electrodynamics.

A fundamental equation of x-ray diffraction is Bragg's law, which states that for a periodic repetition of crystal planes, scattered x-rays show constructive interference if:

$$m\lambda = 2d\sin(\Theta) \qquad (3.24)$$

where m is a natural number, λ is the wave length, d is the distance between the planes and Θ is the angle between the planes and the primary x-ray beam. For more complex evaluations, it is convenient to use the reciprocal lattice, which will be introduced in the following.

3.4.1 Crystal axis and reciprocal lattice

An ideal crystal is built from a periodically repeating alignment of atoms or molecules. Hence it is possible to describe a crystal by a volume that repeats itself. This repetition can be described by three vectors $\vec{a}_1, \vec{a}_2, \vec{a}_3$. The volume of the parallelepiped formed by these vectors is called the unit cell. Each

atom/molecule within the unit cell has a certain position r_n with respect to the origin of the unit cell. Using the periodicity of the crystal, it is possible to describe all sets of equidistant planes by means of the intercepts of the planes and the crystallographic axis, where one plane passes through the origin and the next plane intercepts at $\vec{a}_1/h, \vec{a}_2/k, \vec{a}_3/l$. Due to the periodicity of lattice, the h, k, l (also called the Miller indices) have to be integers.

Bragg's equation (3.24) contains the orientation and the spacing of the planes. A simple description of these two properties can be done by a vector $\vec{H}_{hkl}$, which is normal to the planes and its length is proportional to the reciprocal distance of the planes. For the definition of these vectors the reciprocal vectors $\vec{b}_1, \vec{b}_2, \vec{b}_3$ are used where:

$$\vec{b}_1 = \frac{\vec{a}_2 \times \vec{a}_3}{\vec{a}_1 \cdot \vec{a}_2 \times \vec{a}_3}, \qquad \vec{b}_2 = \frac{\vec{a}_3 \times \vec{a}_1}{\vec{a}_2 \cdot \vec{a}_3 \times \vec{a}_1}, \qquad \vec{b}_3 = \frac{\vec{a}_1 \times \vec{a}_2}{\vec{a}_3 \cdot \vec{a}_1 \times \vec{a}_2} \qquad (3.25)$$

Then $\vec{H}_{hkl}$ is:

$$\vec{H}_{hkl} = h\vec{b}_1 + k\vec{b}_2 + l\vec{b}_3 \qquad (3.26)$$

For this definition $\left|\vec{H}_{hkl}\right|$ equals $1/d_{hkl}$. Using $\vec{H}_{hkl}$ Bragg's law can be written in vector form:

$$\frac{\vec{s} - \vec{s}_0}{\lambda} = \vec{H}_{hkl} \qquad (3.27)$$

where $\vec{s}_0$ is the unit vector in the direction of the primary beam and $\vec{s}$ is the unit vector in the direction of the scattered beam. A graphical representation of equation (3.27) is displayed in figure 3.5. In
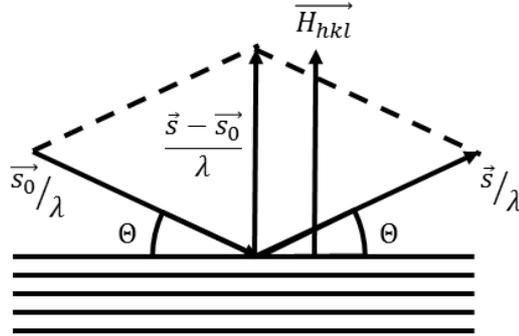

Figure 3.5: Graphic representation of Bragg's law using $\vec{H}_{hkl}$. Graphic adapted form [45]

case the unit cell is not the smallest unit cell possible, some of the reflexes do not appear. For a face-centred cubic bravais lattice (where all positions are occupied by the same species of atoms) it can be calculated that only combinations of (hkl) where all h,k,l are either even or uneven, but not mixed, lead to reflexes. (E.g. the (111) reflex is visible, but the (100) and the (110) "reflexes" do not appear.)

3.4.2 Powder diffraction method

Powder in the x-ray sense refers to a sample with many randomly oriented crystals, so that the Bragg equation for any combination of *hkl* is satisfied. Due to the random distribution of crystallographic orientations, the reflected beam has one degree of freedom. As a consequence the reflected beams form cones, where the central axis equals the direction of the primary beam. The opening angle of these so called Debye cones is $2\Theta(hkl)$.

There are some systematic errors for diffractometer recordings. Table 3.1 lists the possible sys-

tematic errors and their impact on the powder pattern recorded. These errors shift the peak position. Additionally they lead to peak broadening. The total peak width due to these errors is called the instrumental broadening, which can be corrected by conducting reference measurements.

Table 3.1: Systematic errors for a diffractometer recordings

Error	impact
Displacement of the sample surface from the center	$\frac{\Delta d}{d} = \frac{\Delta y}{R}\cos^2(\Theta)$
Imperfect focusing	$\frac{\Delta d}{d} = \frac{\Delta y}{R}\cos^2(\Theta)$
Penetration of the Beam	$\frac{\Delta d}{d} = \frac{\Delta y}{R}\cos^2(\Theta)$
An error in the zero value of 2Θ	$\frac{\Delta d}{d} = K\cos(\Theta)$
Axial divergence	$\frac{\Delta d}{d} = \frac{h^2}{8R^2}$

where Δy is the distance of the scattering event from the ideal position of the scattering event, R is sample-detector distance and h is the distance along the slit

3.4.3 Peak broadening

Besides the instrumental broadening, properties of the sample like particle size, inhomogeneous strains and twin faulting can lead to a peak broadening as well. Hence the peak width can be used to analyse the sample. In order to do so, a correction of the instrumental broadening is required and the different contributions to the peak broadening need to be separated. How this can be done is described in the following part.

The measured peak is a convolution of the instrumental function and the peak function:

$$h(x) = 1/A \int g(z)f(x-z)\mathrm{d}z \tag{3.28}$$

where $f(x-z)$ is the sample broadening function, A is the area of the $f(x-z)$ curve, $h(x)$ is the measured peak intensity at position x and $g(z)$ is the instrumental broadening function. The contribution of the instrumental peak broadening to the overall peak broadening depends on the peak shape. Typically diffraction peaks are well described by a convolution of a Gaussian and a Cauchy shaped peak. For pure Gaussian or Cauchy shaped peaks the instrumental contribution can easily be calculated by [45]:

$$\text{Gaussian shape}: \quad B^2(h) = B^2(g) + B^2(f) \tag{3.29}$$
$$\text{Cauchy shape}: \quad B(h) = B(g) + B(f) \tag{3.30}$$

where $B(h)$, $B(g)$ and $B(f)$ are the peak breaths of $f(y)$, $g(z)$ and $h(x)$ respectively. Since real peaks are never pure Gaussian nor pure Cauchy peaks, but always convolutions of both, a correction is more difficult. A possibility for correcting instrumental broadening was introduced by Stokes (known as the Stokes correction). For this purpose the complex peak functions of $f(y)$, $g(z)$ and $h(x)$ are used:

$$f(y) = \sum_n F(n)\exp^{-2iny/a} \tag{3.31}$$

$$g(z) = \sum_{n'} G(n')\exp^{-2in'z/a} \tag{3.32}$$

$$h(x) = \sum_{n''} H(n'')\exp^{-2in''x/a} \tag{3.33}$$

where $F(n)$, $G(n')$ and $H(n'')$ are the Fourier coefficients of $f(y)$, $g(z)$ and $h(x)$. The Fourier coefficients of the measured peak function and the instrumental broadening can be used to calculate the Fourier coefficients of the sample peak function $f(y)$ by:

$$F(n) = \frac{H(n)}{G(n)} \qquad (3.34)$$

The sum of all Fourier coefficients contains all information of the sample peak. Due to the amount of work, this correction of peak broadening is typically done by a computer program.

A method for separating particle size and strain contributions to the peak broadening was introduced by Warren and Averbach [46]. It is based on the analysis of the cosine Fourier coefficients (A_n) of the peak with increasing indexing. Their calculations show that the A_n can be written as a multiplication of size and a distortion coefficient ($A_n = A_n^S A_n^D$), where A_n^S depends on the domain size in the direction of the scattering vector and A_n^D depends on the distortion in the direction of the scattering vector and on h_0^2 [3] according to [45]:

$$\ln A_n(h_0^2) = \ln A_n^S - 2\pi^2 h_0^2 < Z_n^2 > \qquad (3.35)$$

where Z_n is a measure for the distortion along the direction of the scattering vector and defined via: $< \varepsilon_L > = h_0 Z_n / L$, where $< \varepsilon_L >$ is the average strain along the length $L = nh_0$. This equation can be used to obtain the A_n^S and $2\pi^2 h_0^2 < Z_n^2 >$ values by plotting the $A_n(h_0)$ values of at least two peaks against h_0^2. In this Plot the linear extrapolation of the $A_n(h_0^2)$ to $h_0^2 = 0$ gives the A_n^S values and the slopes equal $-2\pi^2 < Z_n^2 >$.

The value n in the Fourier coefficients is a measure for the number of unit cells in the column, hence nd_{hkl} is a measure for the column length. For convenience, the size coefficients are given as A_L^S, where $L = nd_{hkl}$. These A_L^S values can now be used to calculate an area and volume average column length. The volume average volume length is simply twice the area under the A_L^S vs. L curve and the area average column length can be obtained by extrapolating the A_L^S vs. L curve for low L to the L axis, where the intercept is the area average column length [47].

$$< L >_{\text{vol}} \quad = 2 \int_0^\infty A_L^S(L) \mathrm{d}L \qquad (3.36)$$

$$< L >_{\text{area}} \quad = \frac{-A_L^S}{\lim_{L \to 0}(\mathrm{d}A_L^S / \mathrm{d}L)} \qquad (3.37)$$

---

[3]For cubic lattices ($h_0^2 = h^2 + k^2 + l^2$)

4 Thermodynamic calculations and models

4.1 The potential-strain coupling parameter in substitutional solid solutions

The PSCP of substitutional solid solutions has not been evaluated so far. As discussed in the earlier, the PSCP of the bulk equals the change of the chemical potential with elastic strain. The chemical potential for substitutional solid solutions as discussed by Larché and Cahn only treats replacements of atoms and not addition of atoms to newly created lattice places. For the system discussed in the thesis at hand, this is not sufficient, because lithium is added to the gold sample and does not replace it. Therefore the lithium concentration is directly linked to the number of lattice places.

In order to evaluate the impact of stress on the chemical potential for adding lithium to the sample, a meaningful definition of the strain is required, which links the lithium concentration to the number of lattice places. A possible definition which satisfies this requirement is, that the strain is measured with respect to the insoluble gold atoms. Deposition at the surface is not included in this definition, satisfying that only bulk mechanisms are discussed at this point. This definition of the strain equals the definition used by Larché and Cahn for interstitial solid solutions, hence the chemical potential for interstitial solid solutions has to be equal to the chemical potential for uptake of atoms in a substitutional alloy μ_{up}:

$$\mu_{\mathrm{up}}(\rho_{\mathrm{Act}}, \sigma_{ij}) = \mu_{0,\mathrm{up}}(\rho_{\mathrm{Act}}) - \frac{\partial \varepsilon_{ij}^{sf}}{\partial \rho_{\mathrm{Act}}} \sigma_{ij} - \frac{1}{2} \left(\frac{\partial C_{ijkl}}{\partial \rho_{\mathrm{Act}}} \sigma_{ij} \right) \sigma_{kl} \tag{4.1}$$

Using the finding, that the chemical potential for substitutional uptake equals the chemical potential for interstitial uptake allows to adapt the findings for interstitial uptake to fit substitutional uptake. Viswanath and Weißmüller evaluated the PSCP for interstitial uptake of hydrogen at the stress free state [41]. According to their evaluation, the PSCP for interstitial uptake depends on the change in lattice parameter with active material concentration ($\widehat{\eta}$; see equation (3.17) and (3.18)). This definition requires a direct correlation of the stress free strain and the lattice parameter, which is satisfied for interstitial solid solutions, but not for substitutional solid solutions. In order to apply the theory of Viswanath and Weißmüller to substitutional uptake a more general definition of η, which is able to describe the strain upon uptake of lithium but does not change in magnitude for interstitial solid solutions, is required. This can be done by defining η as a local, stress free strain due to the addition of active material. An η which satisfies the requirement can be defined by:

$$\eta = \frac{N_{\mathrm{host}}}{2} \left. \frac{\mathrm{d}e^{\mathrm{sf}}}{\mathrm{d}N_{\mathrm{active}}} \right|_{\sigma_{ij}} \tag{4.2}$$

where e^{sf} is the stress free planar strain which equals the sum of the strain components parallel to the film $e^{\mathrm{sf}} = \varepsilon_{11}^{\mathrm{sf}} + \varepsilon_{22}^{\mathrm{sf}}$. Using this definition of η instead of $\widehat{\eta}$ allows to use the results evaluated for interstitial solid solutions for substitutional uptake of active material.

4.1.1 The effect of stress

In the following the effect of stress on the PSCP is discussed. For the sake of simplicity uni-axial deformation in 11 direction is presumed for evaluating the effect of stress on the PSCP. Using the equality of forces at equilibrium according to equation (3.13) leads to a change in electrode potential with uni-axial strain according to:

$$\frac{\mathrm{d}\mu_{\mathrm{up}}}{\mathrm{d}\varepsilon_{11}} = \frac{\mathrm{d}\mu_{\mathrm{int}}}{\mathrm{d}\varepsilon_{11}} = -Fz\left.\frac{\mathrm{d}E}{\mathrm{d}\varepsilon_{11}}\right|_{\varepsilon_{ij\neq 11}} \tag{4.3}$$

The chemical potential for substitutional uptake of active material depends in a similar way on the stress as the chemical potential for interstitial uptake of active material. Hence the following evaluations should fit both cases. Both chemical potentials contain a term which depends on the change of the compliance tensor with concentration and the stress state. Consequently the change of electrode potential due to uni-axial strain can be calculated to be (see Appendix 10.1):

$$\left.\frac{\mathrm{d}E}{\mathrm{d}\varepsilon_{11}}\right|_{\varepsilon_{ij\neq 11},q} = \frac{1}{Fz}\left(\frac{\partial\varepsilon_i^{\mathrm{sf}}{}_j}{\partial\rho}C_{ij11} + \frac{\partial C_{ijkl}}{\partial\rho}C_{ij11}\sigma_{kl}\right) \tag{4.4}$$

Simple transformations lead to:

$$\left.\frac{\mathrm{d}E}{\mathrm{d}\varepsilon_{11}}\right|_{\varepsilon_{ij\neq 11},q} = \frac{\eta_{ij}C_{ijkl}\Omega}{zq_0} + \frac{\partial C_{ijkl}}{zq_0\partial c}C_{ij11}\sigma_{kl} \tag{4.5}$$

where $c = N_{\mathrm{active}}/N_{\mathrm{host}}$. For a homogeneous material under biaxial strain variations, which does not change its elastic properties, this derivative leads to equation (3.18), as shown in the Appendix 10.1. In case of non-constant elastic properties an additional term, which is proportional to the stress and the change in elastic properties with active material concentration, has to be added. The proportionality to the stress offers the possibility to estimate the stress free PSCP by interpolating $\frac{\mathrm{d}E}{\mathrm{d}e}|_q$ to zero stress.

4.2 The combined potential strain coupling parameter

The change in electrode potential with elastic strain depends on all charge-transfer dependent mechanisms active at the electrode potential under investigation. It has to be assumed that each mechanism has its own PSCP, giving rise to the question, how the measured PSCP depends on them. In the following this question is discussed assuming two mechanisms. In order to fit the problem at hand one mechanisms is a surface mechanism and the second one is a bulk mechanism. The evaluation itself does not require any assumption on whether the mechanisms are surface or bulk mechanisms. Consequently, similar estimations can be made for any two mechanisms. Furthermore it is not required that one mechanism is correlated to a single physical process, but can be correlated to a family of different processes as well. As in the example at hand, all surface processes are correlated to ς^s and all bulk processes to ς^b. Consequently the results can easily be extended to more than two contributions. Before evaluating the combined PSCP, the PSCP of the bulk needs to be defined in a meaningful way.

4.2.1 The potential-strain coupling parameter of the bulk

For being able to evaluate the interrelation of surface an bulk mechanisms in thin film electrodes, it is meaningful to define an scalar apparent surface stress, which satisfies the requirements of a planar stress state and has a similar effect on underlying material as a numerically equal real surface stress.

This requirement is satisfied by an apparent surface stress (f^{app}) defined by:

$$f^{\mathrm{app}} = \sigma_\parallel h \tag{4.6}$$

where $\sigma_\parallel = (\sigma_{11} + \sigma_{22})/2$ is the scalar stress in the plane of the film and h is the thickness of the film. In a similar manner the PSCP of the bulk (ς^{b}) can be written as:

$$\varsigma^{\mathrm{b}} \equiv \left. \frac{h\mathrm{d}\sigma_\parallel}{\mathrm{d}q^{\mathrm{app}}} \right|_{e,\sigma_\perp} = \left. \frac{\mathrm{d}E}{\mathrm{d}e} \right|_{q^{\mathrm{app}},\sigma_\perp} \tag{4.7}$$

where q^{app} is the apparent surface charge density, $e = \varepsilon_{11} + \varepsilon_{22}$ is the tangential elastic strain of the film.

4.2.2 The combined potential-strain coupling parameter

In case surface and bulk mechanisms are active at the same time, real and apparent surface stresses cannot be distinguished by DECMA. The same is true for the real and apparent surface charge density, hence the reaction of the electrode potential to elastic strain equals:

$$\left. \frac{\mathrm{d}E}{\mathrm{d}e} \right|_{q+q^{\mathrm{app}}} = \left. \frac{\mathrm{d}(f + f^{\mathrm{app}})}{\mathrm{d}(q + q^{\mathrm{app}})} \right|_e = \left. \frac{\mathrm{d}(f + h\sigma)}{\mathrm{d}(q + q^{\mathrm{app}})} \right|_e \tag{4.8}$$

The right hand side of this equation can be written as:

$$\left. \frac{\mathrm{d}(f + h\sigma)}{\mathrm{d}(q + q^{\mathrm{app}})} \right|_e = \left. \frac{\mathrm{d}(h\sigma)}{\mathrm{d}(q^{\mathrm{app}})} \frac{\mathrm{d}q^{\mathrm{app}}}{\mathrm{d}(q + q^{\mathrm{app}})} \right|_e + \left. \frac{\mathrm{d}(f)}{\mathrm{d}(q)} \frac{\mathrm{d}q}{\mathrm{d}(q + q^{\mathrm{app}})} \right|_e \tag{4.9}$$

Since the surface and the bulk need to be at the same electrical potential, we can write:

$$\frac{\mathrm{d}q^{\mathrm{app}}}{\mathrm{d}(q + q^{\mathrm{app}})} = \frac{C^{\mathrm{b}}}{C^{\mathrm{b}} + C^{\mathrm{s}}} \tag{4.10}$$

$$\frac{\mathrm{d}q}{\mathrm{d}(q + q^{\mathrm{app}})} = \frac{C^{\mathrm{s}}}{C^{\mathrm{b}} + C^{\mathrm{s}}} \tag{4.11}$$

where C^{b} is the capacity of the bulk and C^{s} is the capacity of the surface. In case of non-equilibrium conditions, C^{b} and C^{s} are the effective capacities of the bulk and the surface. In terms of capacities, equation (4.8) can be written as:

$$\left. \frac{\mathrm{d}E}{\mathrm{d}e} \right|_{q+q^{\mathrm{app}}} = \left(\left. C^{\mathrm{s}} \frac{\mathrm{d}E}{\mathrm{d}e_s} \right|_q + \left. C^{\mathrm{b}} \frac{\mathrm{d}E}{\mathrm{d}e_b} \right|_{q^{\mathrm{app}}} \right) \frac{1}{C^{\mathrm{s}} + C^{\mathrm{b}}} \equiv \varsigma^{\mathrm{c}} \tag{4.12}$$

Using the definitions of the surface and bulk PSCP (equation (3.8) and (4.7)) leads to:

$$\left. \frac{\mathrm{d}E}{\mathrm{d}e} \right|_{q+q^{\mathrm{app}}} = \left(C^{\mathrm{s}}\varsigma^{\mathrm{s}} + C^{\mathrm{b}}\varsigma^{\mathrm{b}} \right) \frac{1}{C^{\mathrm{s}} + C^{\mathrm{b}}} \equiv \varsigma^{\mathrm{c}} \tag{4.13}$$

The combined PSCP ς^{c} is an effective capacity weighted average of the surface and the bulk PSCP.

Equation (4.13) can in principle be used to separate surface and bulk contributions if the effective capacity of the surface and the bulk, as well as the combined PSCP and the PSCP of one contribution are known. In such a case the PSCP of the surface can be calculated to be:

$$\varsigma^{\mathrm{s}} = \frac{\varsigma^{\mathrm{c}}(C^{\mathrm{s}} + C^{\mathrm{b}}) - C^{\mathrm{b}}\varsigma^{\mathrm{b}}}{C^{\mathrm{s}}} \tag{4.14}$$

In an equivalent way the PSCP of the bulk can be calculated by:

$$\varsigma^{\text{b}} = \frac{\varsigma^{\text{c}}(C^{\text{s}} + C^{\text{b}}) - C^{\text{s}}\varsigma^{\text{s}}}{C^{\text{b}}} \tag{4.15}$$

4.3 The interrelation of the potential-strain coupling parameter and the lattice parameter

Real and apparent surface stresses can change the lattice parameter of a sample. Besides these, other contributions (e.g. change in composition) can have an impact on the lattice parameter as well. For distinction of elastic and compositional changes of the lattice parameter the orientation dependency can be used. In the following it is assumed that all changes of the lattice parameter are a result of an elastic deformation. For the sake of simplicity coherent deformation of sample and substrate is presumed.

Equation (4.8) links the real and apparent surface stress changes with charge density to the PSCP. By integration it is possible to calculate $\Delta(f + f^{\text{app}})$:

$$\Delta(f + f^{\text{app}}) = \int_0^{q + q^{\text{app}}} \varsigma^{\text{c}} \mathrm{d}(q + q^{\text{app}}) \tag{4.16}$$

The change in apparent surface stress on its own is linked to a planar stress in the sample by equation (4.6). According to linear elasticity a planar stress is related to a planar strain by $\sigma_\parallel = B\varepsilon_\parallel^e$ where $B = Y/(1 - \nu)$ is the biaxial modulus, which equals the Young's modulus (Y) devided by one minus the Poisson's ratio (ν) for materials with cubic symmetry. Hence the apparent surface stress change is parallel to the change in elastic strain and therefore lattice parameter ($\varepsilon^e = \frac{a - a_0}{a_0}$). For a real surface stress the change in lattice parameter can be calculated by a balance of forces:

$$f + \int_0^{z_{\text{max}}} \sigma_\parallel(z)\mathrm{d}z = 0; \text{ where } 0 < z < h_{\text{sample}} + h_{\text{substrate}} \tag{4.17}$$

$$\Rightarrow f = -\int B\varepsilon_\parallel \mathrm{d}z \tag{4.18}$$

where z is the coordinate along the thickness of the sample. This equation states, that surface stress changes are anti-parallel to changes of the in-plane lattice parameter and consequently have an anti-parallel impact as a numerically equal change of an apparent surface stress.

In order to make more qualitative statements, knowledge of the electrode and the substrate is required. In the following, three cases, schematically illustrated in figure 4.1, will be discussed in order to highlight the importance of the substrate and the principle difference between the interrelation of the PSCP and the lattice parameter for surface and bulk mechanisms. The three cases are:

1. A free standing thin film
2. A thin film with fixed planar dimensions (infinitely stiff substrate)
3. A thin film supported by a finitely stiff substrate.

All cases are calculated for homogeneous, purely planar strains (no bending) and homogeneous elastic properties using a model of the sample. This model consists of a polyimide foil substrate covered with a titanium adhesion layer and a gold thin film, where only the gold film (the sample), is subject to a stress free strain.
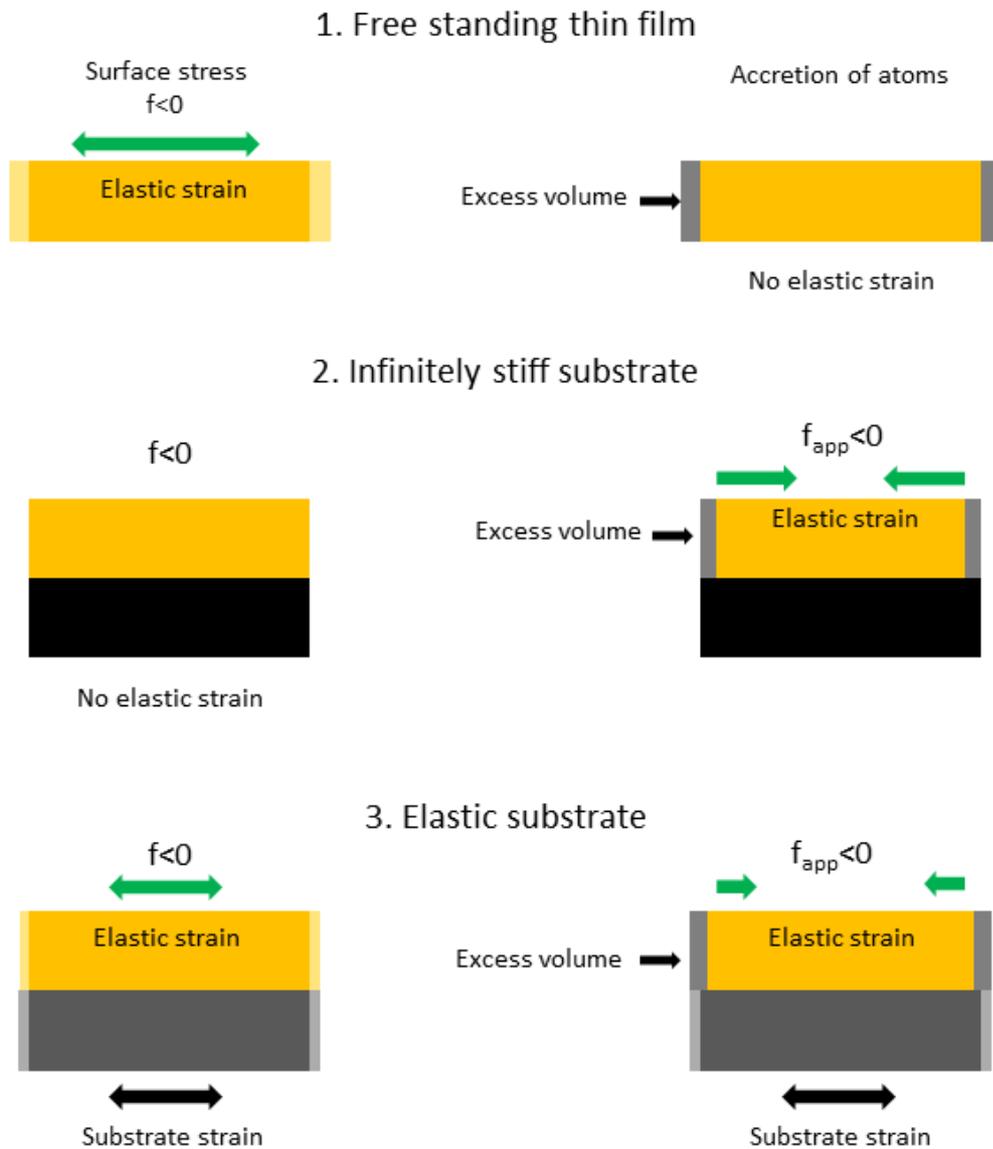
Figure 4.1: Schematic representation of the interaction of the surface stress and the apparent surface stress with elastic deformation of the sample depending on the substrate. 1. Free standing film: For a free standing film changes of the surface stress can induce an elastic deformation. A change in the stress free strain, indicated by the excess volume, can not induce an elastic strain. 2. Infinitely stiff substrate: For a thin film on an infinitely stiff substrate, changes of the surface stress cannot induce any elastic strain, but a stress free strain is counteracted by the substrate, which induces an elastic deformation of the sample. 3. Elastic substrate: A surface stress has to deform the sample as well as the substrate. An stress free strain of the sample, indicated by an excess volume, is counteracted by the substrate, which leads to an elastic deformation of the film and the substrate until a balance of force is established.

Idealised Case: Free Standing Thin Film Electrode

The apparent surface stress is a measure for a stress of the sample on the substrate due to a stress free excess in planar dimensions. Consequently, there cannot be any apparent surface stress without a substrate. On the other hand, a real surface stress can induce elastic strain on a free standing thin film sample. In case of pure planar deformations the elastic deformations can be calculated by:

$$f + B_{\text{Au}} h_{\text{Au}} \varepsilon_{\parallel}^{\text{e}} = 0 \tag{4.19}$$

$$\Rightarrow \quad f = -B_{\text{Au}} h_{\text{Au}} \varepsilon_{\parallel}^{\text{e}} \tag{4.20}$$

where B_{Au} is the biaxial modulus of the (gold) sample and h_{Au} is the thickness of the sample.

Idealised Case: Infinitely Stiff Substrate

This case significantly differs from the one mentioned before, because the overall strain cannot change. A direct consequence is that the surface stress cannot influence the lattice parameter. Equation (4.6) still needs to be satisfied. This leads to:

$$\varepsilon_{\parallel}^{\text{e}} = -\varepsilon_{\parallel}^{\text{sf}} = \frac{\sigma_{\parallel}}{B_{\text{Au}}} = \frac{f^{\text{app}}}{B_{\text{Au}} h_{\text{Au}}} \tag{4.21}$$

For an infinitely stiff substrate the elastic change of the in-plane lattice parameter is directly correlated to the apparent surface stress.

Idealised Case: Elastic Substrate

In this case the impact of the surface stress is very similar to the first case, except for the increased stiffness of the film due to the substrate. The strain induced by the surface stress can be calculated by:

$$f = -(B_{\text{Au}} h_{\text{Au}} + B_{\text{sub}} h_{\text{sub}}) \varepsilon^{e} \tag{4.22}$$

$$\Rightarrow \quad \varepsilon^{\text{e}} = \frac{-f}{B_{\text{Au}} h_{\text{Au}} + B_{\text{sub}} h_{\text{sub}}} \tag{4.23}$$

An apparent surface stress induces a stress on the substrate, which is thereby strained. Again using balance of forces leads to:

$$B_{\text{sub}} h_{\text{sub}} \varepsilon_{\text{sub}}^{\text{e}} = -f^{\text{app}} = -B_{\text{Au}} h_{\text{Au}} \varepsilon^{\text{e}} \tag{4.24}$$

The overall elastic strain can then be calculated by:

$$\varepsilon^{\text{e}} = \frac{-f}{B_{\text{Au}} h_{\text{Au}} + B_{\text{sub}} h_{\text{sub}}} + \frac{f^{\text{app}}}{B_{\text{Au}} h_{\text{Au}}} \tag{4.25}$$

This equation states that real and apparent surface stress changes strain the sample in inverse directions. Using that the overall strain needs to be equal in all layers ($\varepsilon^{\text{e}} + \varepsilon^{\text{sf}} = \varepsilon_{\text{sub}}^{\text{e}}$) allows to calculate the elastic strain form changes of the stress-free strain:

$$\varepsilon^{\text{e}} = \frac{-f}{B_{\text{Au}} h_{\text{Au}} + B_{\text{sub}} h_{\text{sub}}} - \varepsilon^{\text{sf}} \frac{B_{\text{sub}} h_{\text{sub}}}{B_{\text{sub}} h_{\text{sub}} + B_{\text{Au}} h_{\text{Au}}} \tag{4.26}$$

The elastic strain of the sample depends on the surface stress and on the stress free strain.

5 Experimental

5.1 Experimental methods

5.1.1 Magnetron sputtering

DC magnetron sputtering is a physical vapour deposition method. In this work it is used for the preparation of thin film samples. The principle of magnetron sputtering is that ions (in this work argon ions) are accelerated towards a target of a certain material. The impact of the ions on the target leads to the removal of atoms from the surface of the target into a gaseous state. These atoms travel to the substrate and condense there to form a film.

In more detail, the sputter-gun consists of an anode and a cathode, where the cathode is the target. By applying an electrical voltage (some hundred volts) between both electrodes, it is possible to ignite a plasma of (inert) gas ions and electrons. The only requirement for ignition of the plasma is that the pressure is low enough and that the electric field high enough. Because of the electric field, the positively charged argon ions are accelerated towards the target, whereas the electrons are accelerated towards the anode.

In magnetron sputtering, additionally to the electrical field, there is a magnetic field that forces the electrons to follow helix lines. The magnetic field is aligned in such way that it is parallel to the surface in a region slightly above the surface of the target. Due to this magnetic field, the electron density is strongly increased where the magnetic field is parallel to the surface. Hence more gas atoms will be ionised and the sputter rate below this area is strongly increased. This has the big advantage that it is possible operate at a lower pressure which leads to more homogeneous films.

5.1.2 Evaluation of the deposition rate

Optical ellipsometry was used for evaluating the deposition rate of the sputter device. Hence only a very basic overview on the topic will be given here. The device, which was used, consists of three parts, a "'Base-160"', an "'EC-400"' and an "'M-2000F"', all of which are from J.A. Woollam Co.®.

Optical ellipsometry uses the fact that thin films change the polarisation of an electromagnetic wave depending on the wavelength, the optical parameters of the material, the thickness and roughness of the film. As the optical materials parameters and the wavelength of the light are typically known [1], changes of the polarisation can be linked to thickness and eventually roughness of the film. This naturally works only as long as the film is optically transparent, and the reflection of the film-substrate interface is contributing to the measured signal. For metal films this is typically the case if the path of light within the metal is significantly smaller than the wavelength.

5.1.3 Sample characterisation

Sample characterisation was done by scanning tunnelling microscopy (STM) for investigating the surface profile and by electron backscatter diffraction (EBSD) for investigating the microstructure.

STM measures the tunnelling current between a sharp tip and the sample while moving the tip along the surface. The dependency of the tunnelling current on the distance from the tip to the sample

---

[1] All the required materials parameters were contained in the analysis software "Wvase32"

is used to evaluate the distance. The measurement can be done in two different ways: Either the tunnelling current is kept constant and the movement of the tip in the height coordinate is used to evaluate the height profile, or the height coordinate of the tip is kept constant and the tunnelling current is used to evaluate the height profile.

Electron backscatter diffraction (EBSD) is a method to investigate the crystal orientation using the diffraction patterns from backscattered electrons. Typically this method is used to analyse the backscattered electrons of an electron beam of a scanning electron microscope (like for the thesis at hand) or transmission electron microscope. Those backscattered electrons produce interference patterns, which are typical for the lattice of the sample, similarly to diffraction patterns of x-ray diffraction. Consequently it is possible to evaluate the crystal orientations from the patterns. Due to the localisation of the electron beam in both devices, EBSD can be used to locally investigate the microstructure of the sample. Nowadays EBSD is a very common method for sample characterisation and typically fully automated.

5.1.4 Dynamic-electro-chemo-mechanical analysis

The theoretical description of the measurement principle can be found in section 3.2.1 for single surface and bulk mechanisms. How two simultaneously active mechanisms contribute to the DECMA signal is evaluated in section 4.2. A detailed description of the DECMA-stage used in this work can be found in section 5.2.1. In the following some technical details are presented, which are necessary to calculate the PSCP from the measured values.

The measurement is performed by varying the uni-axial strain of a thin film sample on a substrate and recording the strain triggered variation of the electrode potential. The uni-axial strain is used to calculate the variation of the surface area, which is done by using the elastic properties of the substrate:

$$e = \varepsilon_{\mathrm{uni}}(1 - v_{\mathrm{sub}}) \tag{5.1}$$

where e is the elastic variation of the surface area, $\varepsilon_{\mathrm{uni}}$ is the uniaxial strain and v_{sub} is the poisson's ratio of the substrate. In order to evaluate the PSCP ς^{c} equation (3.11) is used. The variation of the potential is directly measured by the lock-in amplifier, whereas the area strain variation is calculated from the measured uniaxial strain variation according to equation (5.1). According to equation (3.11) the variation of the electrode potential should be in-phase with the variation of the strain, while phase shifts of both signals are indications for a damped signal. Hence only the in-phase variations of the potential are used for evaluating the PSCP, while out-of-phase variations are only used to estimate whether the signal is significantly damped:

$$\mathrm{Re}\varsigma^{\mathrm{c}} = \frac{\mathrm{Re}\hat{E}}{\hat{e}} \tag{5.2}$$

The measurement needs to be performed at a constant charge density (measured in the reference state). In order to perform the measurement during electrochemical cycling, it is mandatory that within the characteristic time of the strain variation, the charge transfer is negligible. This situation can be accomplished by introducing a resistor between the electrical source (potentiostat) and the sample. If this resistor is big enough, the measurement error is negligible. In this configuration, the potential variation is measured at the sample side of the resistor and the electrode potential on the poteniostat side of the resistor (a detailed wiring diagram is shown in figure 5.3). A side-effect of the resistor for decoupling the electrode from the potentiostat is that, for non vanishing currents, there is a potential decay along the resistor. Hence the potential at the potentiostat differs from the potential at the electrode. This

difference can be corrected by [36]:

$$U_{\text{sample}} = U_{\text{potentiostat}} - R * I \qquad (5.3)$$

Additionally the resistor influences the potenital variation (dU/dt) at the sample. In general the current measured during electrochemical cycling depends on the potential and the change in potential ($I = I(U, dU/dt)$). It is possible to estimate the maximum deviation of the actual current from a current expected for a constant scan speed during potential scans by assuming purely capacitive behaviour:

$$I_{\text{corr}} \approx I \frac{dU_{\text{potentiostat}}}{dU_{\text{sample}}} \qquad (5.4)$$

This equation allows to evaluate an upper bound for the error due to the scan speed deviation.

5.1.5 In-situ x-ray diffraction

A short description of the theoretical background of X-ray diffraction is shown in section 3.4.

X-ray diffraction is a powerful tool for investigating periodic structures, like crystalline solids. The principle of the measurement is based on the interference of x-rays scattered at periodic structures. The orientations that show constructive interfearence are correlated to the periodicity of the structure according to Bragg's law (see equation (3.27)). A very common method for investigating materials, which is used in this work as well, is the powder diffraction method. In case many different orientations of the sample material are investigated at the same time, constructive interference has one degree of freedom, which is rotation along the primary beam. Hence directions of constructive interference of a certain periodicity results in a cone, the so called Debye cone. By evaluating the opening angle of the debye cones, it is possible to calculate the distance of the scattering planes ($d_{(hkl)}$).

5.2 Custom made experimental devices

Two custom made devices were used for the main measurements of this thesis. The first one is an electro-chemo-mechanical analysis stage for operation inside a glove-box and the second one is an in-situ electrochemical cell for microstructural characterisation during electrochemical cycling in lithium-ion electrolytes.

5.2.1 The dynamic electro-chemo-mechanical analysis stage

The design of the DECMA stage built for this work was inspired by the one used by Smetanin *et al.* [35, 48]. In the following the mechanical, electrical and electrochemical setup of the device are presented separately.

The mechanical setup was redesigned in order to fit the requirements. Detailed Blueprints of each part can be found in the Appendix. Significant changes with respect to the device used by Smetanin *et al.* [35, 48] have been made in order to provide easy access for operation inside a glovebox. This was achieved by keeping the main part as small as possible, which allows fast transfer through the air-lock of the glovebox. For this purpose a stand-alone frame is used, which connects all parts. For operation this frame is screwed onto a stainless steel rack.

Additionally two changes were made in order to increase the accessible frequency range. The piezo actuator used is significantly smaller than the one used by Smetanin *et al.* and the massive frame was designed to be very stiff in the actuation direction of the piezo actuator. The small piezo actuator allows operating at much higher frequencies, but with the expense of reduced stiffness and displace-
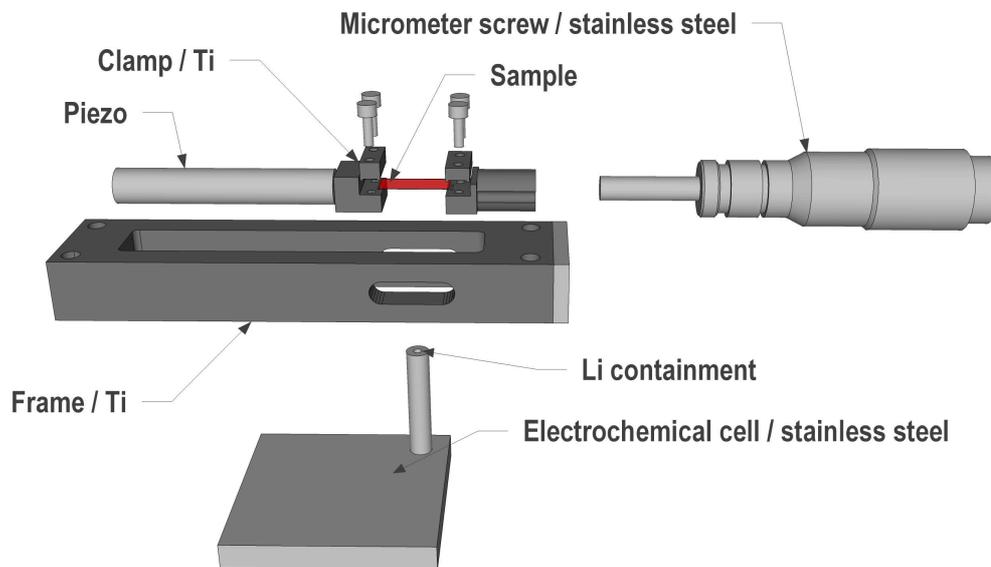
Figure 5.1: The disassembled mechanical setup of the DECMA stage. All parts are made from Tita-
          nium (dark gray) or stainless steel (SLS; light gray). The piezo actuator is inside a stainless
          steel housing. The electrochemical cell shown here is the miniaturised two electrode elec-
          trochemical cell. For operation, the DECMA stage is attached to a stainless steel rack and
          the cell is attached to a lab-boy for adjusting the height. Neither the rack nor the lab-boy is
          shown in this sketch.
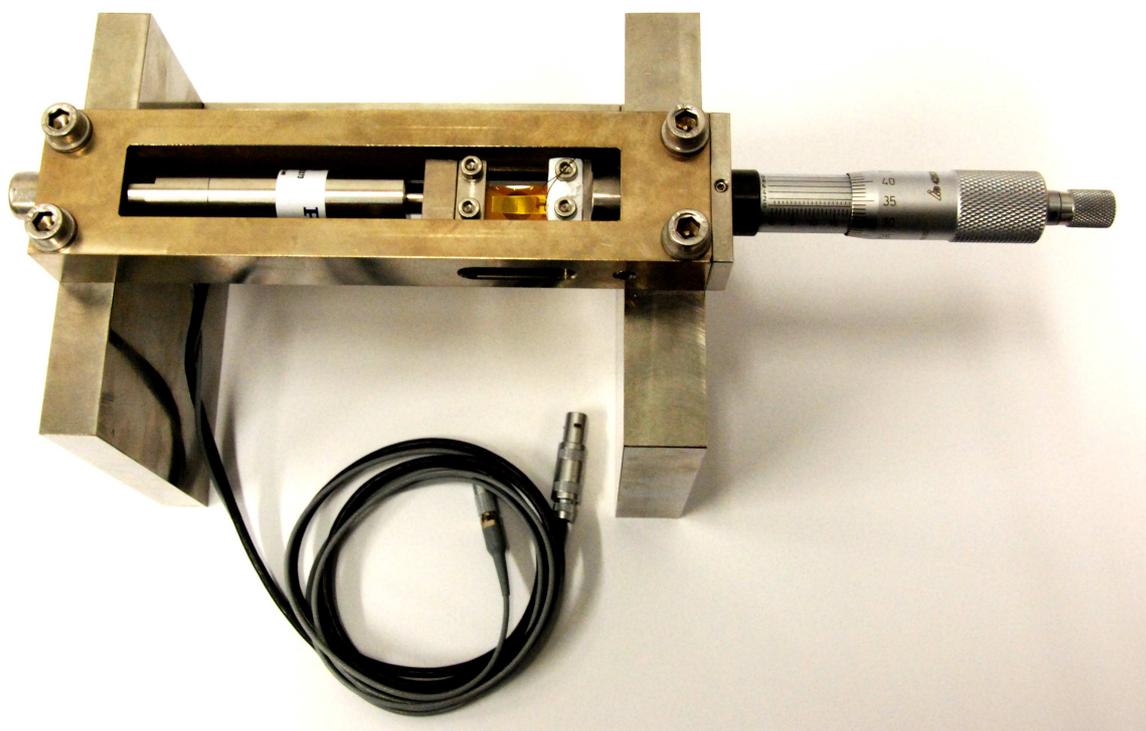
Figure 5.2: Picture of the assembled DECMA stage on the stainless steel rack with a mounted sample.
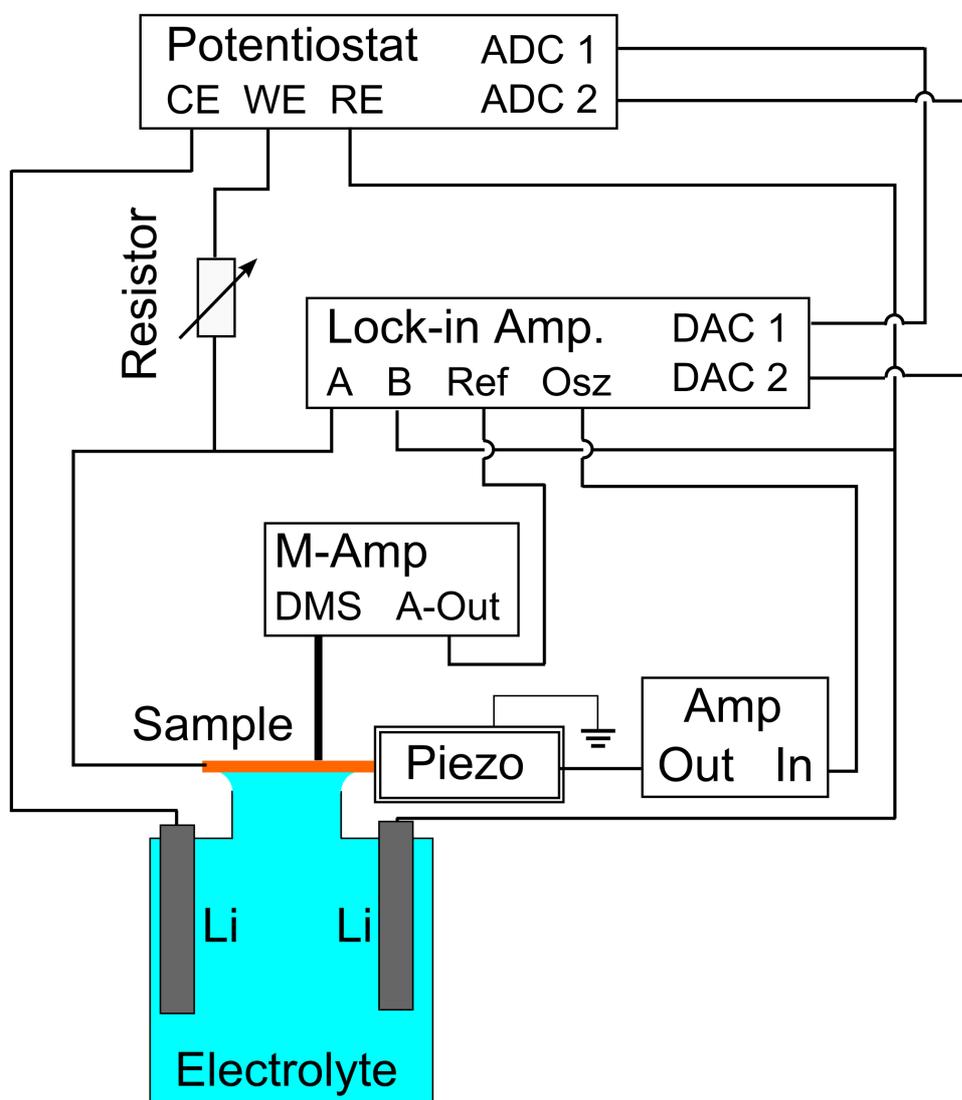
Figure 5.3: Wiring diagram for the DECMA stage for measuring the potential-strain coupling parameter using the three electrode electrochemical cell. For using the two electrode electrochemical cell, CE and RE are short-circuited. M-Amp is an abbreviation for measurement amplifier. The resistor is a decade resistor used for preventing the potentiostat from counteracting the potential variations. The ADC 1 and ADC 2 are analogue inputs for the potentiostat, CE, WE and RE correspond to the Counter, Working and Reference Elektrode connectors of the Potentiaostat. A and B are the signal inputs of the Lock-in amplifier, Ref is the reference input of the lock-in amplifier and Osz, DAC 1 and DAC 2 are the oscillator output and the analogue outputs of the lock-in amplifier. The measurement amplifier is connected to the half bridge configuration via the connectors named DMS and has an analogue output proportional to the strain in A-Out. The amplifier for the Piezo actuator just has one input (In) and one output (Out)

ment amplitude. Potential shortcomings resulting from the reduced stiffness (stress and frequency dependent as well as reduced amplitude) were circumvented by reducing the weight of the moving clamp as far as possible and introducing a most direct strain measurement, which is discussed below. The reduced native displacement amplitude of the actuator was counteracted by reducing the sample size, which allows similar strains besides smaller displacements.

For applying the required pre-strain, a micrometre screw was introduced. Compared to the original device this micrometre strew offers a better control over the pre-straining. It was designed in such a way that the clamp, which is attached to the micrometre screw, can be screwed to the frame after pre-straining in order to fix the position of the clamp and reduce potential unwanted vibrations.

Another change compared to the original device is the use of resistive strain gages as substrates for the sample. In this way the measurement of the amplitude and the phase improved significantly for high frequencies (>100 Hz). Furthermore the usage of resistive strain gages allowed to pre-strain the sample to a desired value, which turned out to be very helpful.

Additionally to the mechanical the electrical setup has been changed as well. A wiring diagram of this electrical setup is shown in figure 5.3. The central device is the potentiostat. All the data comes together there (except the straining amplitude). The potentiostat sets the electrode potential and measures the current or vice versa. Additionally it receives two analogue signals from the lock-in amplifier proportional to the in-phase and out-of-phase amplitudes of the potential variation due to the applied strain variation.

Figure 5.4: Electrochemical cells for DECMA. Left: three electrode electrochemical cell, where the big container is used for the counter electrode, the tube in the middle for contacting the sample and the one on the right for the reference electrode. The container for the reference electrode reaches into the middle tube and has an opening one millimetre below the top of the middle tube to behave almost like a Luggin capillary. Right: miniaturised electrochemical cell for operation in two electrode configuration. The steel rod has a small hole in the middle, which is filled with lithium. Contact to the sample is accomplished by some drops of electrolyte on top of the rod.

The lock-in amplifier has two tasks: It provides the sine signal for the amplifier that operates the piezo actuator, and it measures the potential variation of the electrode potential with respect to the reference electrode. There are three possible signals that can be used as a reference signal for the lock-in amplifier:

1. The analogue signal from the measurement amplifier that measures the strain of the substrate

2. The measured strain of the piezo actuator

3. The internal reference of the lock-in amplifier

The accuracy is highest for the first and lowest for the last possibility. For small frequencies ($<100\,\mathrm{Hz}$) all of them are suitable. The amplifier operating the piezo actuator is quite simple, it just amplifies the voltage signal of the lock-in amplifier by a factor of 10 with a very low output-impedance. The already mentioned measurement amplifier is only required for measuring the strain and strain variation of the resistive strain gage substrate. It drastically improved the measurement accuracy of the straining amplitude and the phase when operating at high frequencies. For operation, the strain gage is wired according to a half bridge configuration. In order to use the analogue output as a reference signal for the lock-in amplifier a low-pass Bessel filter is used with a typical border frequency of roughly 100 times the operating frequency.

(a) Servo control mode   (b) Normal mode
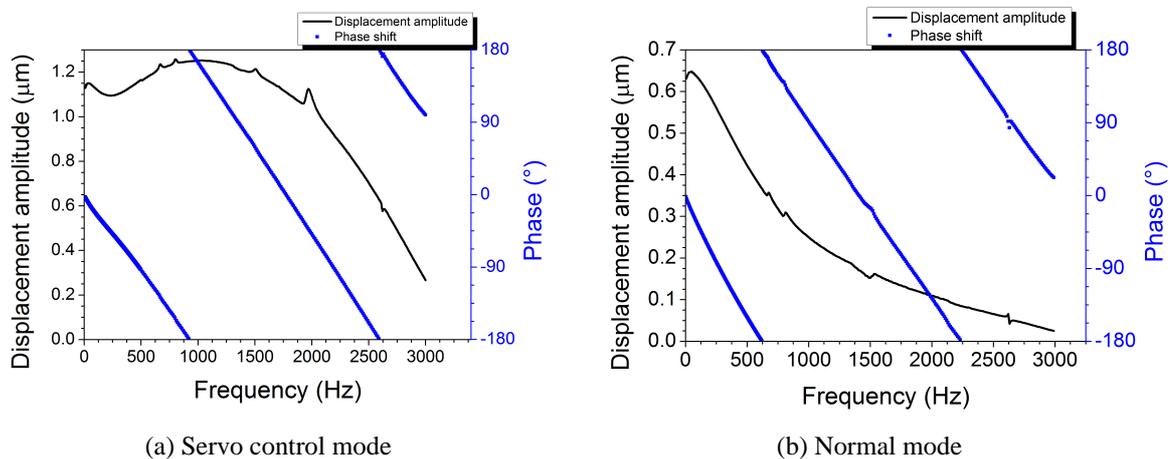
Figure 5.5: Displacement amplitude and phase shift with respect to the oscillator signal of the strain measured via a resistive strain gage, when operating in (a) the servo control mode (b) normal mode. When using the servo control mode the electronics tries to keep the amplitude, which is measured by a resistive strain gage on the piezo actuator, constant and regulates the voltage correspondingly, while in the normal mode the input voltage is simply amplified. In both cases the phase shift has a roughly linear dependency on the frequency, which corresponds to a roughly constant time delay of $60\,\mathrm{ms}$. It is important to mention that, the amplitude is not constant in the servo control mode, besides the fact that the electronics of the piezo actuator tries to keep the displacement amplitude constant. For the normal mode, the decay of the amplitude is roughly what would be expected for a first order low-pass filter. Both modes show several resonance peaks indicating the resonance frequency of the setup.

A very critical aspect of electrochemical measurements especially in lithium battery electrolytes is the electrochemical cell. Hence two different electrochemical cells were tested: A three electrode electrochemical cell made from glass, and a miniaturised two electrode electrochemical cell made from stainless steel. Both are displayed in figure 5.4. It turned out that the miniaturised two electrode electrochemical cell significantly reduces Faradaic losses and reduces the noise below the resolution of the lock-in amplifier. Furthermore, it allowed longer measurement periods due to reduced evaporation

of the dimethyl carbonate in the electrolyte without showing any measurable disadvantages at typically used scan speeds of 1 mV/s.

The overall performance and the suitability for lithium alloy electrodes of the newly designed DECMA stage was tested in detail. The improvement of the accessible frequency range was quite pronounced. Using the servo control the frequency for which the remaining amplitude was only half of the initial amplitude was beyond 2500 Hz. Without using the servo control, the amplitude was halfed already at 750 Hz. The measured phase-shift is quite significant. This is an indication that the electrical setup produces some time delay. Hence it is required that the phase shift is measured with respect to the phase shift of the actual strain. Amplitude and phase dependency on the frequency are shown in figure 5.5a and figure 5.5b for servo controlled and normal operation. For long time high frequency operation it is not recommended to use the servo control in order to prevent damaging the piezo actuator.
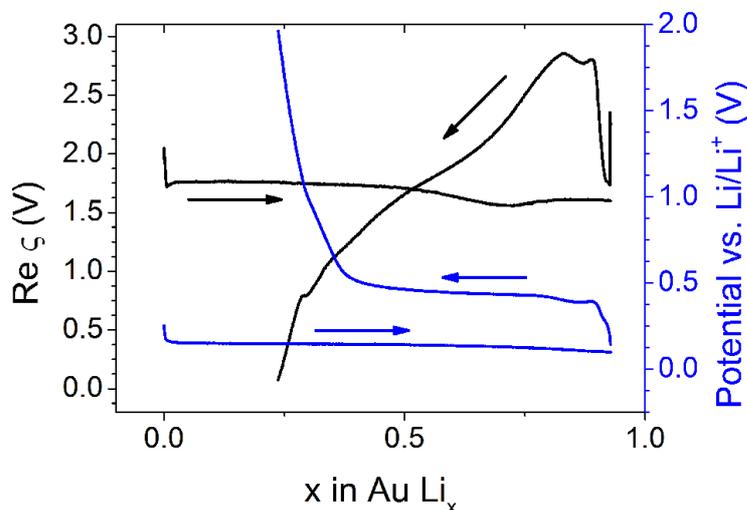
Figure 5.6: PSCP (black) and electrode potential (blue) measured during electrochemical alloying at a constant current density of 20 μA/cm^2 up to a composition of AuLi$_1$. The straining frequency was 20 Hz.

In order to evaluate the suitability of the DECMA setup for lithium alloy anodes, the PSCP of a thin gold film was measured during electrochemical alloying up to a composition of Au$_1$Li$_1$. The results displayed in figure 5.6 show a very stable signal for the whole potential range.

According to equation (4.5) a constant stress, and therefore pre-strain, in the sample can have an impact on the PSCP, if the elastic properties of the material change with concentration. For being able to estimate the effect of constant stress due to the applied pre-strain on the PSCP, two different measurements have been performed with different values of pre-strain. The first measurement was performed with a pre-strain of 0.5%, the second one with a pre-strain of 1%. Both PSCP curves, recorded during cyclic voltammetry with a scan speed of 1 mV/s, are displayed in figure 5.7. They behave quite similar, but the curve for a pre-strain of 1% is shifted to more positive values, except for the values measured below 0.5 V vs. Li/Li$^+$ in the negative scan direction and up to 1 V vs. Li/Li$^+$ in the positive scan direction. Consequently, it has to be assumed that the PSCP is slightly influenced by the pre-strain. Nevertheless, the effect only gives a small and roughly constant contribution, compared to other effects.
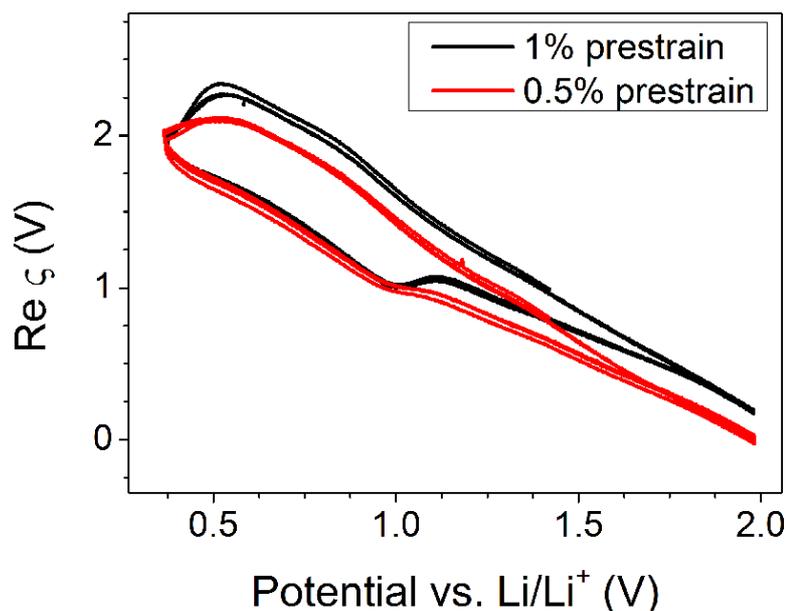
Figure 5.7: DECMA for a 55 nm thick gold film measured with different values of pre-strain. The measurement was performed during cyclic voltammetry with a scan speed of 1 mV/s, a straining frequency of 20 Hz and a RMS straining amplitude of $\approx 110\,\mu$m/m.

5.2.2 The electrochemical cell for in-situ x-ray diffraction

The In-situ electrochemical cell was designed and built in the course of this work. More precisely two slightly different designs were built and used, but only the device built more recently is presented here, because very little changes were made which did not change the performance. Detailed blueprints of all the parts can be found in the appendix.

The aim of the design was to build an in-situ electrochemical cell that can be used to measure the lattice parameter by x-ray diffraction and gracing incidence x-ray diffraction. As it turned out, the polyimide foil was too thick for gracing incidence in-plane diffraction. Nevertheless it was possible to record diffraction patterns at tilting angles as low as $\chi = 10°$ with high peak intensity[2], which was sufficient for this work.

Figure 5.8 shows a blueprint of the in-situ electrochemical cell. The cell design is a closed container with a polyimide window. This polyimide window is used as the substrate of the sample at the same time. Furthermore, the parts of the cell were designed in such a way that the polyimide window is pushed to the highest point of the electrochemical cell. During this process the polyimide is slightly strained and thereby fixed in height. The stability was nicely demonstrated during experiments (see figure 5.10b and 5.10a). An important contribution to this stability stems from the butyl bladder that was attached to the cell to compensate changes in the external pressure or volume changes of the electrolyte (e.g. by evaporation, decomposition or thermal expansion). The body and the bottom of the electrochemical cell are made from PEEK (Polyether ether ketone). The top consists of two stainless steel rings to clamp the polyimide x-ray window between them. The electrode connections are stainless steel screws. The body has an opening for inserting the electrolyte, which is closed with a stainless steel screw as well. The O-ring between the body and the top, as well as the one between the body and the bottom are made from NBR (Nitrile butadiene rubber). The O-ring, which fixes the polyimide window to the stainless steel rings of the top is made from FFKM (Perfluoroelastomer).

The assembly of the in-situ cell works as follows:

---

[2]$\chi = 0.2°$ are needed for gracing incidence in-plane diffraction
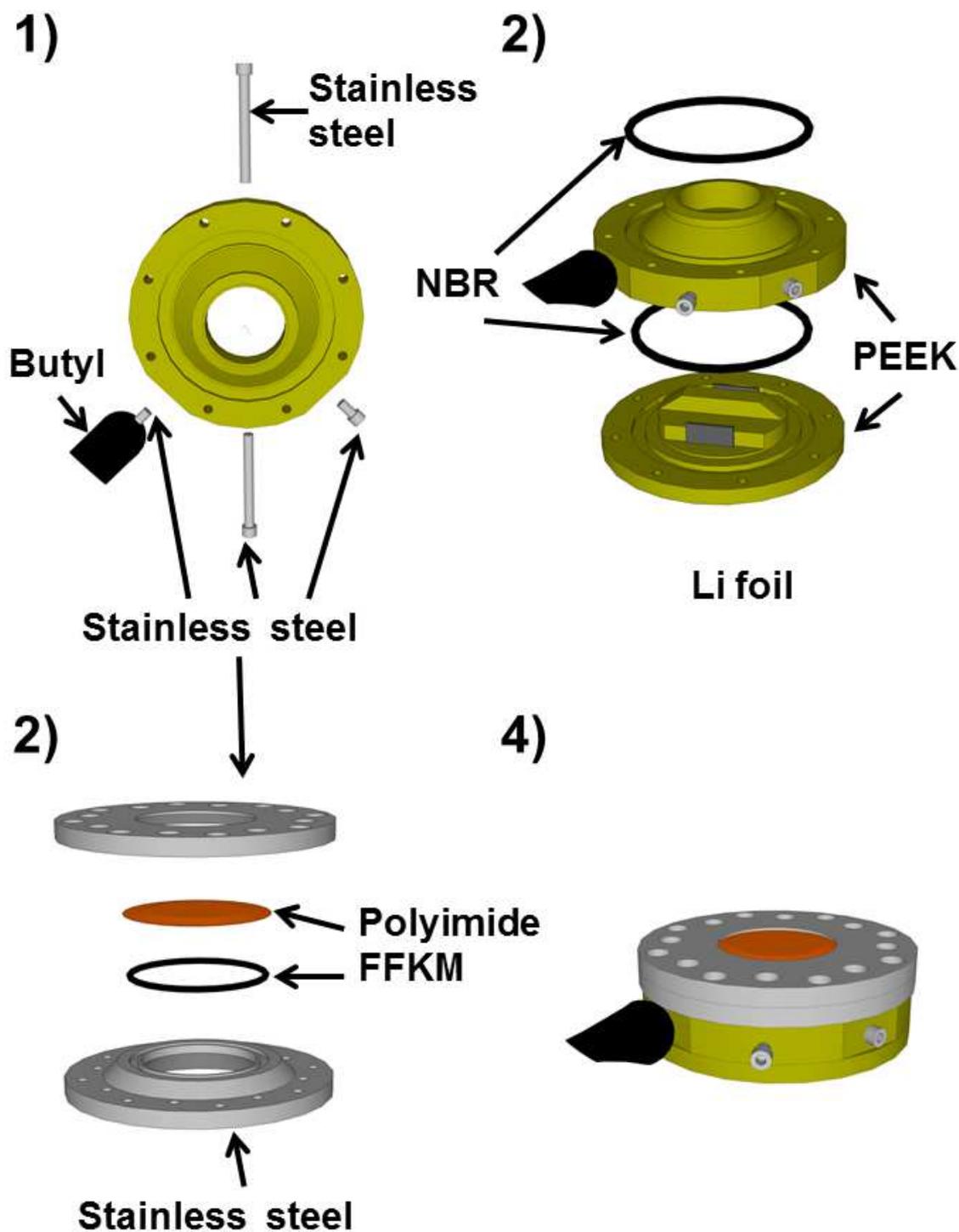
Figure 5.8: All the parts of the electrochemical cell and how to assemble it. 1. The body of the electro-chemical cell with all the screws made from stainless steel. 2. The body and the bottom of the electrochemical cell and the nitrile butadiene rubber (NBR) O-rings for sealing, shown in the sequence of assembly. 3. The top of the electrochemical cell together with the poly-imide foil and the perfluoro-elastomer (FFKM) O-ring in the sequence of assembly. 4. The assembled in-situ electrochemical cell.
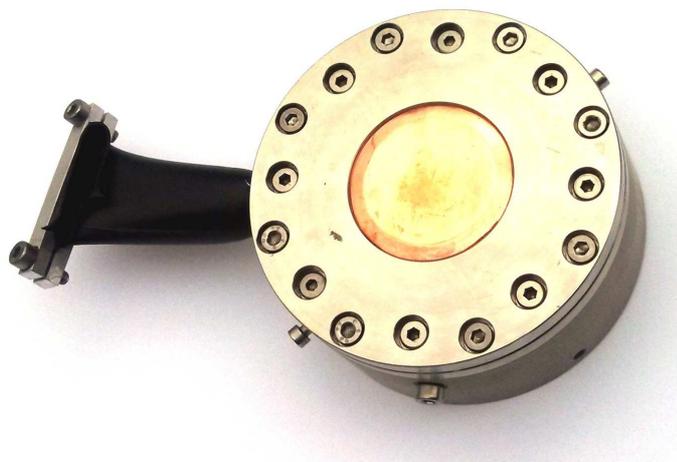
Figure 5.9: Picture of the assembled in-situ electrochemical cell with a mounted sample.

1. The body and the bottom of the cell are attached to each other to form the open cell.
2. The butyl bladder is attached to the Body and closed using the aluminium clamp.
3. The lithium foil electrodes are put into the open cell and clamped between the stainless steel screws and the PEEK bottom; there is a suitable front for this in the second version and a spacer in the first version of the cell.
4. The polyimide foil is clamped between the two stainless steel rings to form the top of the cell.
5. The top of the cell is screwed to the body of the cell.
6. The cell is filled with electrolyte through the filling hole.

Typically this assembly, as well as changes of the sample can be done in about 15 minutes.

In order to evaluate the stability of the lattice parameter measurement during in-situ measurements, a copper reference film was sputtered on the polyimide foil, on the opposite side than the sample. This allowed simultaneous measurement of the gold and copper (111) peaks, without exposing the copper to the electrolyte. Since both films share the same substrate height de-adjustments as well as creep deformations of the substrate should influence both films in a similar manner. Figure 5.10a and 5.10b show the stability of the copper lattice parameter during electrochemical measurements for a tilting angle of $\chi = 90°$ and $\chi = 10°$ respectively in contrast to significant, electrochemically induced changes of the gold lattice parameter.

5.3 Experimental details

5.3.1 Sample preparation

The samples were produced by DC magnetron sputtering. As a substrate 75 μm thick polyimide foil in round shape (5 cm diameter; for microstructural characterisation) or polyimide based resistive strain gages (HBM 1-LY11-10/120; $18 \times 9.5 \times 0.1 \, mm^3$; for DECMA) were used. Samples for DECMA were sputtered on the smooth side of the resistive strain gage. Before sputter deposition the substrates were cleaned using argon plasma etching. After this they were transferred to the sputter chamber without contact to air. In the sputter chamber the base pressure was $< 4 \times 10^{-8}$ mbar. During sputter deposition a working pressure of 5.7×10^{-3} mbar was established by a constant flow of 7 SCCM (standard cubic centimetre per minute) of argon 5.0. All target materials had a purity of 99.99%.

(a) $\chi = 90°$

(b) $\chi = 10°$
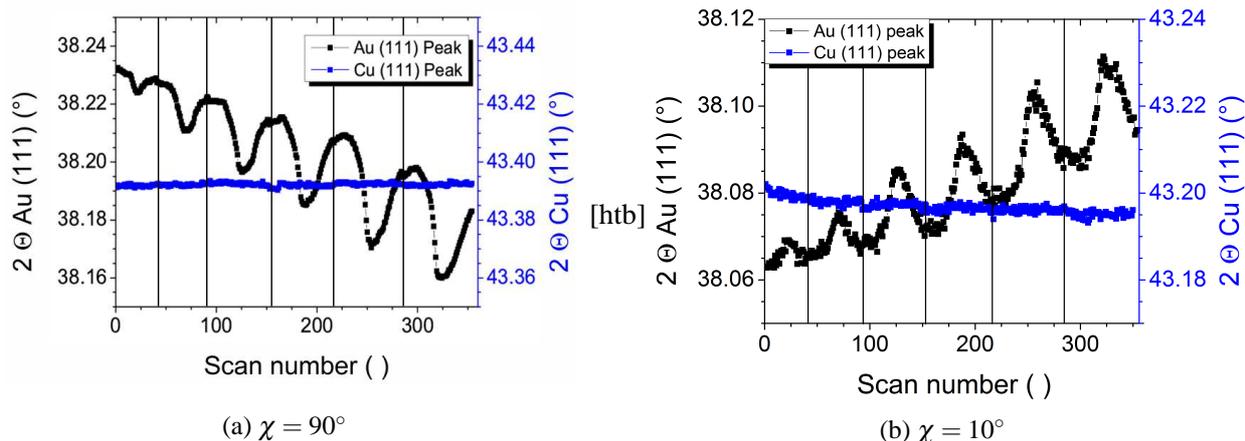
Figure 5.10: Gold and copper (111)-peak-position vs. scan number during 6 CV cycles of recorded at a tilting angle of (a) $\chi = 90°$ and (B) $\chi = 10°$. The horizontal lines separate the different CVs and therefore the time gap during which the other tinting angle was measured. Between the first and the last measurement several hours passed, nevertheless the position of the copper peak is very stable in both cases and shows only a small and monotonous drift, which is in contrast to the gold (111) peaks.

Target sample distance was $\approx 15\,cm$ (Ti, Au) / $\approx 7\,cm$ (Cu). The sputter deposition was performed using the constant power mode with a power of 50 W (Au, Cu) or 100 W (Ti). For controlling the layer thickness, sputter time was used. The first layer of each sample is a titanium adhesion layer with a thickness of $\approx 20\,nm$. On top of the adhesion layer the gold sample material was sputtered with a thickness of 55 or 100 nm, depending on the sample. The copper reference film was sputtered without adhesion layer and had a thickness of $\approx 150\,nm$. After sputter deposition the samples were stored at a temperature of 125°C in a laboratory-type drying chamber for at least 7 days and inside a glovebox at 90°C on a heating plate for at least several hours in order to remove water adsorbate.

5.3.2 Sample characterisation

Basic sample characterisation was done by STM and EBSD. Both measurements were performed at the 55 nm thick gold film after x-ray diffraction at a location, which had not been exposed to the electrolyte and hence has not had any contact to lithium.

STM was performed by Qibo Deng using an "'STM5500'" from Agilent ®. The measurement was performed on a $500 \times 500\,nm^2$ big area with 512 lines at a scan speed of $1\,\mu m/s$. For the measurement a bias voltage of 0.1 V, was used and the tip-surface distance was evaluated from the measured tunnelling current.

The measurement was performed by Julia Hütsch who used a FEI Nanolab 200 dual beam SEM, which is equipped with an EDAX EBSD detector. On an area of $2 \times 2\,\mu m^2$ the crystal orientation was measured with a step-size of 10 nm. For this measurement an acceleration voltage of 15 kV was used, while the working distance was 10.7 mm.

5.3.3 Dynamic-electro-chemo-mechanical analysis

Dynamic-electro-chemo-mechanical analysis was performed as potential-strain response measurements for direct measurement of ς [3]. For DECMA the stage shown earlier (see figure 5.2) is used with the miniaturised two electrode electrochemical cell (see figure 5.4 right). The electrolyte was LP30 as purchased from BASF (1 mol $LiPF_6$ in a mixture of ethylene carbonate and dimethyl carbonate 1:1. The purities of the components are 99.80%, 99.98% and 99.95% respectively). As reference signal for the lock-in amplifier the analogue output of the measurement amplifier was used. The amplitude of the strain variation was evaluated by fitting a sine wave to measured data in a strain-time diagram as shown in figure 5.11. All electrical connections were according to figure 5.3, except that a two electrode configuration was chosen (the counter and reference electrode connectors were connected to the same electrode). The decade-resistor for decoupling the potentiostat from the sample was set to $50\,\mathrm{k\Omega}$.
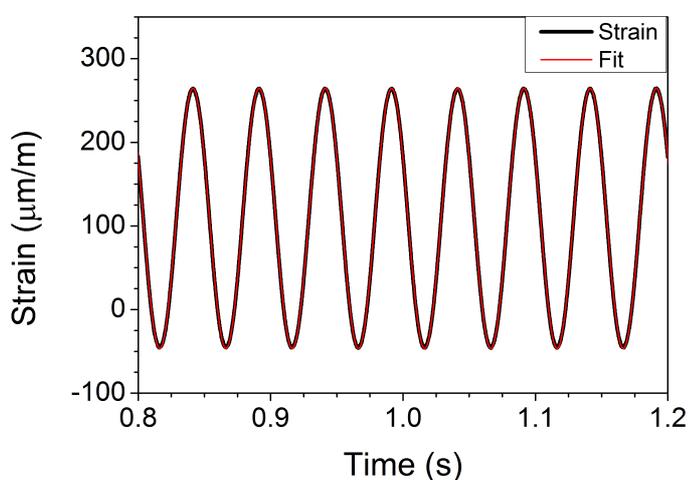
Figure 5.11: Typical strain variations of the resistive strain gage substrate as evaluated by the measurement amplifier (black) and a typical fit to a Sine wave (red).

DECMA measurements were performed during cyclic voltammetry with an applied scan speed of 1 mV/s. In order to highlight the history dependency, the applied potential window was continuously increased starting from [2 V to 1 V], by reducing the lower vertex potential after every 3 CV cycles to 0.7, 0.5, 0.4, 0.3, 0.25 V successively. The straining frequency was 20 Hz and the RMS amplitude was $\approx 110\mu\mathrm{m/m}$. Test measurements at higher frequencies showed similar results, except that for frequencies above 100 Hz the signal significantly decreased and the phase shift increased.

5.3.4 Microstructural characterisation

Microstructural characterisation was done by x-ray diffraction at the KMC-2 bending-magnet beamline [49], situated at the synchrotron facility BESSY II in Berlin. KMC-2 uses a Huber 6-cycle goniometer in psi-geometry for sample manipulation. Data acquisition was done using a two dimensional cross wire detector with a spatial resolution of $70\,\mu\mathrm{m}$ (VANTEC 2000). This detector was placed 60.5 cm away from the sample and shielded from external sources of radiation by an aluminium cone. Measurements were performed in reflection geometry, where the χ-circle was used for changing the tilting

---

[3]DECMA can be performed in current-strain response mode as well. Because of the SEI, which forms at the surface of the sample and influences the impedance, current-strain response measurements, which depend on the impedance, are not feasible for the system at hand. For more information on the differences between potential- and current-strain response, please be referred to [33]

angle between $\chi = 90°$ and $\chi = 10°$ as indicated by the left and right sketch in figure 5.12. Before every measurement all goniometer axes were carefully centred against the primary beam to omit displacement errors. Raw 2-D data from the detector was used to calculate line profile patterns by integrating the 2-D data along Debye-cones. Line profile parameters (peak position, peak height, full width at half maximum, and shape factor) were evaluated by fitting the intensity vs. scattering angle to pseudo-Voigt functions [50].
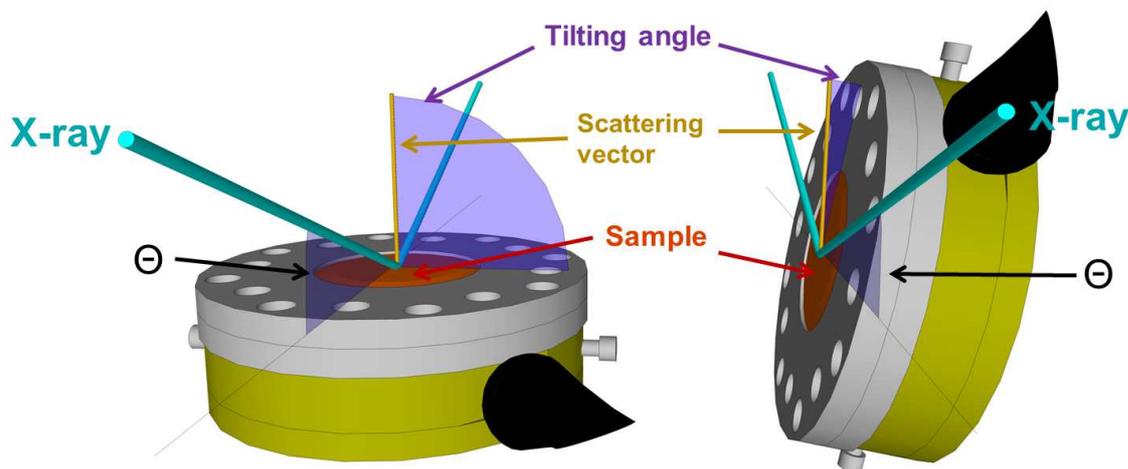
Figure 5.12: Schematic representation of x-ray diffraction measurements performed at a tilting a angle of $\chi = 90°$ (left) and $\chi = 10°$ (right).

Before the measurement all parts (including all the screws) were stored at 100°C inside a laboratory type drying chamber for at least seven days. The assembly of the cell was done inside an argon filled glovebox, with O_2 and H_2O concentrations <10 ppm and <5 ppm respectively. In case it seemed necessary to clean the in-situ cell in open air, it was done without using water and the cell was dried afterwards using a hot air fan[4].

Samples used for x-ray diffraction during cyclic voltammetry had a copper reference film sputtered on the outer side of the polyimide x-ray window. For measurements during cyclic voltammetry only the gold and copper (111) peaks were recorded. Similarly to the DECMA measurements the potential window was increased successively, starting from [2 V to 1 V] and reducing the lower vertex potential after every 2 CV cycles to 0.7, 0.5, 0.4, 0.3, 0.25 V vs. Li/Li$^+$. Between two CV cycles there was a break, which was necessary for the goniometer to change the tilting angle. During the first cycle the tilting angle was $\chi = 90°$ and during the second cycle $\chi = 10°$. For all measurements the incidence angle was 20.5°, which allowed to record the gold and copper (111) peaks at the same time. During the measurement, every 50 s one diffraction pattern was recorded with an acquisition time of 20 s.

The sample for measurements at constant potential had no copper reference. For conducting measurements the potential was slowly reduced to the desired value. After this the potential was kept for at least 30 minutes until the measurement started, in order to minimize electrochemical changes during the measurement. At a tilting angle of $\chi = 90°$ three measurements were performed at incidence angles of 20.5°, 32.5°, and 39.5°. The first measurement covered the (111) and (200) peaks, the second one covered the (220) peak and the third one the (311) and the (222) peaks. At a tilting angle of $\chi = 10°$ one diffraction pattern was recorded for every peak in the following order: (222) (311) (220) (200) (111) with incidence angles of 40.75° 38.7° 32.15° 22.1° 19.05° respectively. Every diffraction pattern was recorded with an acquisition time of 100 s.

---

[4]there was no drying chamber accessible at the synchrotron facility

6 Results

6.1 Sample characterisation

6.1.1 Surface roughness

STM results for the 55 nm thick gold film used for x-ray diffraction are displayed in figure 6.1. The main statistical values of the topology map are shown in table 6.1. Several measurements at different positions were performed, all of which lead to very similar results of the statistical values. A height profile along the diagonal is displayed in figure 6.2. Along this diagonal there are some valleys with a maximum depth of 8 nm below the average height, but most of them do not penetrate the sample more than 6 nm, which corresponds to $\approx 10\%$ of the film thickness, below the average height. This evaluation shows that the film is quite flat, hence the sample is described well by assuming a planar geometry. This assumption is further strengthened the RMS value of 2 nm or $\approx 5\%$ of the film thickness. Another important value is the ratio r of the surface area to the projected area. This value was calculated following the procedure of Deng *et al.* presented in [51] to be 1.069 and can be used to estimate the impact of the roughness on the PSCP of the surface using the theory by Deng *et al.*, which states, that the measured PSCP ς is correlated to the true local PSCP $\hat{\varsigma}$ of the surface by [51]:

$$\varsigma \frac{(1-v)r}{1+v+2vr} = \hat{\varsigma} \tag{6.1}$$

where v is the poisson's ratio. For gold film, which has a poisson's ratio of 0.42 and a roughness factor r of 1.069 the measured PSCP of the surface has to be multiplied by a value of 1.19 in order to obtain the true local PSCP for surface effects.

Table 6.1: Statistical values of the topology profile as calculated by the gwyddion software and the ratio calculated according to [51] corresponding to the topology map displayed in figure 6.1

Value	Magnitude
Measurement area	500 nm x 365 nm
Average height	0 nm
Minimum height	-10.4 nm
Maximum height	4 nm
RMS	1.9 nm
Surface area	195 e-15 m^2
Projected area	183 e-15 m^2
Ratio	1.069
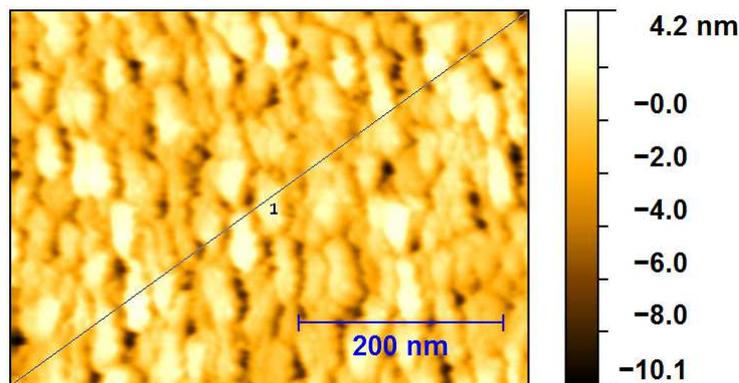
Figure 6.1: Topology map measured by scanning tunnelling microscopy of the 55 nm thick gold film used for x-ray diffraction. The height is measured relative to the average height. This picture shows an area of $500 \times 370 \, \text{nm}^2$. A part of the picture was cut away, because the measurement smeared out.
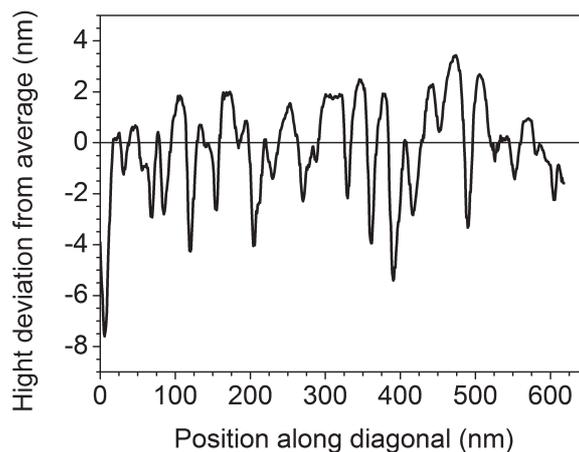
Figure 6.2: Height profile along the diagonal of the topology map shown in figure 6.1. Zero on the position ordinate corresponds to the upper right corner in the topology map. Zero on the height ordinate corresponds to the average height of the topology map.

6.1.2 Microstructural orientation mapping

Similarly to STM, the EBSD measurement has been performed on the same 55 nm thick sample, which had been used for x-ray diffraction. An orientation map is displayed in figure 6.3. The first impression of a rather pronounced (111) orientation is underlined by the inverse pole figure of this EBSD map shown in figure 6.4. Further analysis with respect to grain-size can be found in figure 6.5a. The area weighted average grain diameter was determined to be 68 nm.

An analysis of the misorientation angles is displayed in figure 6.5b. It shows an almost random misorientation distribution except for small angles and 60° misorientations (corresponding to small angle and Σ3 grain boundaries), which appear two to three times more often than random misorientations.

(a) Orientation map   (b) Colour legend
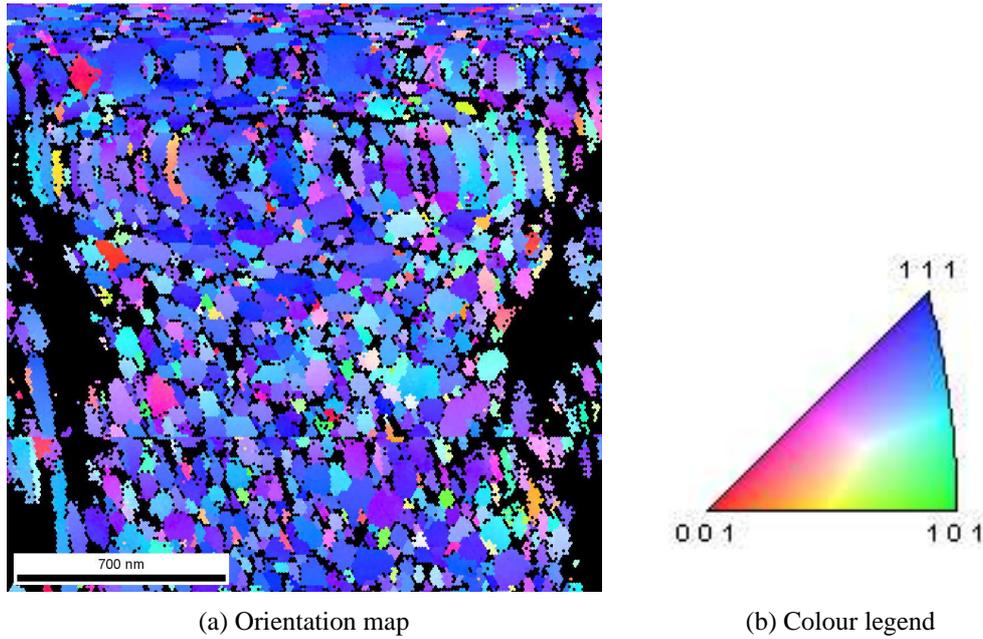
Figure 6.3: (a) Orientation map of the 55 nm thick gold film as evaluated by electron backscatter diffraction. Most grains are oriented close to a (111) orientation. (b) Colour code as inverse pole figure.

[001]
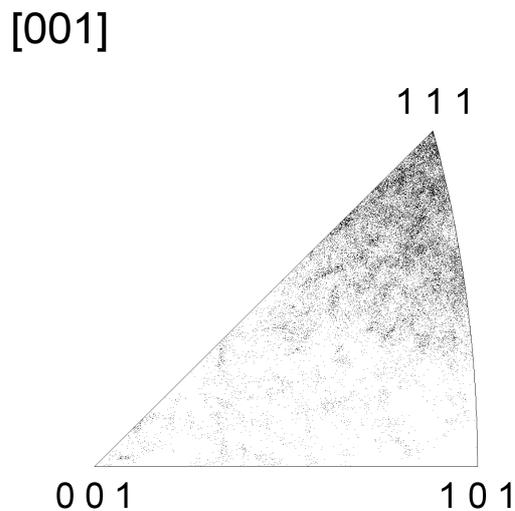
Figure 6.4: Grain orientations displayed in an inverse pole figure as determined from EBSD. Most of the grains show an orientation close to a (111) orientation.

6.2 Dynamic electro-chemo-mechanical analysis

The PSCP of a 55 nm thick gold film measured during cyclic voltammetry with different potential windows is displayed in figure 6.6. For the first cycles from 2 V to 1 V the current changes with cycle number. This is an indication for irreversible processes like electrolyte decomposition. During those cycles the PSCP shows an almost linear dependency on the electrode potential and shifts to slightly
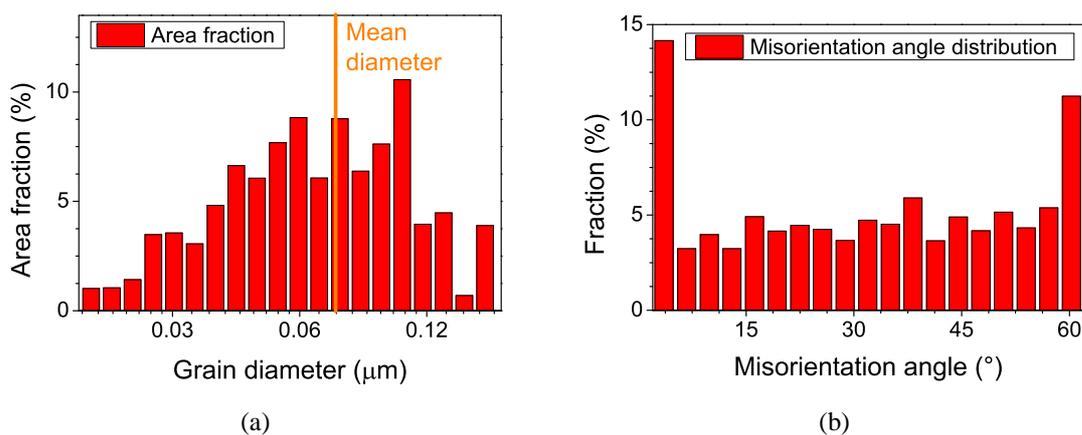
Figure 6.5: a) Area weighted grain size distribution as measured by EBSD. The mean grain size of 68 nm is indicated by the orange line. b) Misorientation of neighbouring grains as measured by EBSD. Except for small angle and Σ3 grain boundaries (60°), the misorientations show a random distribution.

higher values with cycling. For the following potential window (2 to 0.7 V) the shift of the CV curves as well as the PSCP curves diminish. Consequently it can be expected that the shift of both has the same origin. For the PSCP curve a very small hysteresis appears at a potential below 1 V vs. Li/Li$^+$.

When the potential window is increased further (2 to 0.5 V and 2 to 0.4 V; referred to as the intermediate regime in figure 6.6) both curves show significant changes. In the CV curves there appears the underpotential deposition stripping (UPDs) peak at a potential of roughly 1 V in the positive scan direction, which strongly depends on the potential window. Besides that the CV curves hardly change with cycling. There is one exception to this. The first cycle of each potential window shows a more negative current than the following cycles in a potential range exceeding that of the previous cycles. In the PSCP curve the hysteresis is becoming well visible. In the potential range where the hysteresis is visible the PSCP differs for each cycle in the positive scan direction. Besides this the PSCP curves are quite stable. These changes are indications, that the process responsible for the hysteresis is not complete.

In the final stage, corresponding to a potential window of 2 to 0.3 V and 2 to 0.25 V, the CV curves as well as the PSCP curves are very stable. For the PSCP curves the hysteresis is again significantly more pronounced than during the intermediate state and hardly changes with the potential window, being an indication that the process responsible for the hysteresis is complete. At a potential of about 1 V in the positive scan direction the PSCP hardly changes with potential and the hysteresis diminishes significantly. This is exactly where the well visible UPDs peak in the CV curve has its maximum. The obvious conclusion is, that underpotential deposit of lithium, which is deposited in the potential range of 0.9 to 0.3 V [12] and is removed at a potential of about 1 V, is responsible for the hysteresis as well as the plateau visible at a potential of 1 V in the final stage.

It has to be empathised, that regardless of the presence of the SEI, underpotential deposition is still possible. Furthermore the amount of charge transported during one CV cycle does not vanish even for the final cycles, which is associated with ongoing electrolyte decomposition. For one CV cycle in the potential range from 2 to 0.25 V the SEI formation is still responsible for 13% of the charge transfer measured in absolute values. Nevertheless it can be estimated, that the impact of the decomposition current on the PSCP is rather small for the final stage, because the PSCP curves do not drift any more like during the first cycles. This can be understood since the electrolyte decomposition is passivating against further decomposition by blocking electron transport to the electrolyte, which corresponds to a
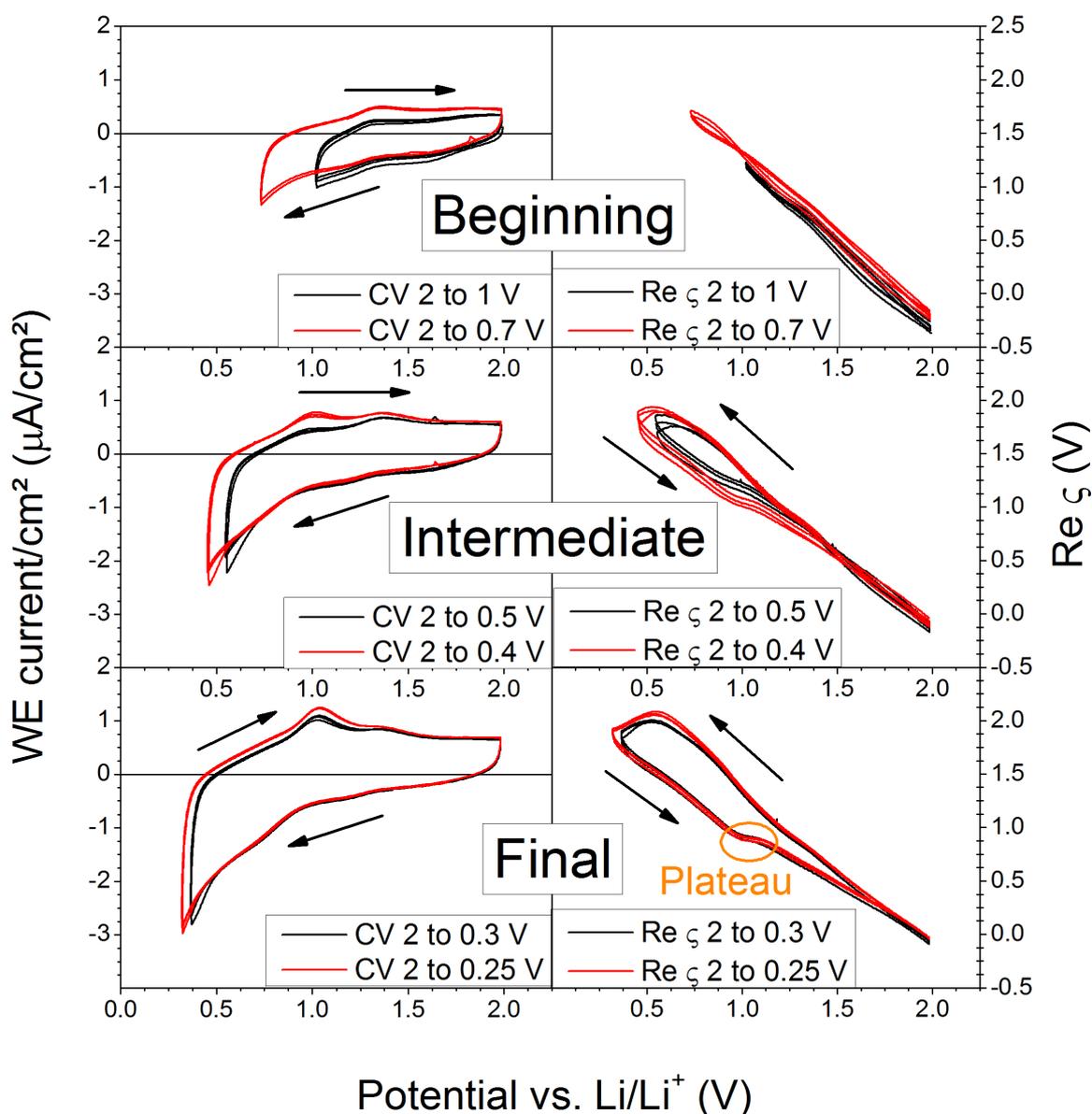
Figure 6.6: PSCP and CV results for a 55 nm thick gold film for cyclic voltammetry with different potential ranges. The measurement was performed at a scan speed of 1 mV/s with a straining frequency of 20 Hz and a strain variation of 110 $\mu m/m$ RMS in LP30. At the beginning the cyclic voltammograms show a certain drift with cycling. This is associated with electrolyte decomposition. The UPDs peak is not visible for the scans in the beginning. The PSCP scans show a certain drift, where the PSCP increases slightly with cycling. For the scan form 2 to 0.7 V a very small hysteresis appears. During the intermediate scans the currents hardly changes with cycling and the UPDs peak is small but well visible. For the PSCP measured in this potential region the drift at high potentials almost vanished, the hysteresis is much more pronounced and the PSCP at low potentials shows a certain drift. For the final scans, the drift of the PSCP has almost disappeared, the hysteresis is very pronounced and the scans show a plateau of the PSCP in the positive scan direction at a potential around 1 V vs. Li/Li$^+$. At the same time the UPDs peak is visible in the CV curve.

very high impedance and consequently a low contribution to the PSCP.

6.3 X-ray diffraction

All x-ray diffraction measurements were performed using the customised in-situ electrochemical cell. Hence all samples are pre-strained. Hence only changes of the lattice parameter are of importance. For displaying the results obtained from the lattice parameter an arbitrary reference was chosen, which typically refers to the first or second measurement value in the plot. Since all analysis is based on changes of the lattice parameter, a pre-strain (e.g. due to the assembly of the in-situ electrochemical cell) has no impact on the results.

In-situ x-ray diffraction was performed at constant potential, as well as during cyclic voltammetry. A typical line profile pattern, calculated from 2D diffraction data is shown in figure 6.7a. The very high peak-to-background ratio of about 14:1 for the (111) gold peak measured at a tilting angle of $\chi = 90°$ shows the quality of the measurement, which enables precise analysis of the data. Figure 6.7b shows a typical fit of a gold (111) peak using a symmetrical pseudo voigt function. The difference between the fit and the peak are very small, showing that the peak has a very high symmetry and that the fit parameters are suitable for describing the peak in a meaningful way. Hence using only peak parameters (2Θ, FWHM and shape factor) for further analysis only leads to a small error. The overall accuracy is demonstrated by the small scatter of the strain values calculated from peak position values shown in figure 6.13, with a standard deviation of about 10^{-5} in the strain for measurements at a tilting angle of $\chi = 90°$ and 3×10^{-5} for measurements at a tilting angle of $\chi = 10°$.

(a) Typical line profile pattern

(b) Symmetrical pseudo Voigt fit
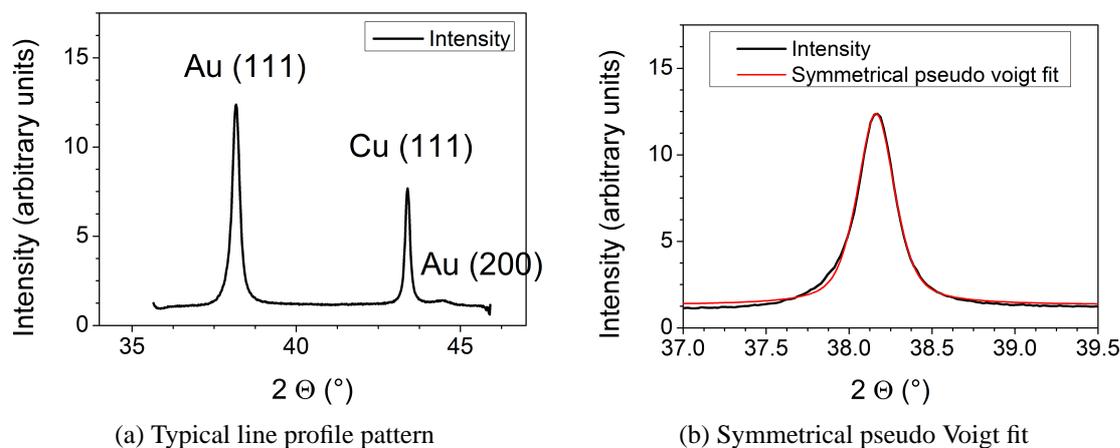
Figure 6.7: a) A typical line profile pattern calculated from a 2D diffraction data recorded during cyclic voltammetry of a 55 nm thick gold film at a tilting angle of $\chi = 90°$ and an electrode potential of 0.25 V with an acquisition time of 20s. b) Symmetrical pseudo Voigt fit of the gold (111) peak shown in a).

The diffraction pattern shows the Au and Cu reflexes, but there are no visible titanium reflexes. The typically most pronounced Ti $(10\bar{1}0)$ reflex which should be visible at $2\Theta = 40.23°$ is not visible for either tilting angle. Hence it can be expected that the Ti (0002) peak which should be at $2\Theta = 38.44°$ does not influence the Au (111) peak.

Even upon reaching 0.25 V, the gold reflexes themselves neither show any sign of a peak at 39.3°, excluding a coexisting crystalline $Au_{69}Li_{39}$ phase (see figure 6.7b) in contrast to measurements that reach lower potentials as for example performed by *Renner et al.* [26], nor are there any visible reflexes corresponding to a phase other than a face centred cubic phase. This shows that the system stays in a single phase regime for the whole measurement.

6.3.1 X-ray diffraction at constant potential

The measurement at constant potential was performed for a 100 nm thick film. Figure 6.8 shows the change of the lattice parameter with respect to the values measured at 2.5 V. The peak positions change significantly for different applied potentials. At a tilting angle of $\chi = 90°$, the (200) and (220) are very weak (see figure 6.7a), which is the reason for the significant scatter. Except the just mentioned two peaks, all reflexes have in common that the sign of the shift only depends on the tilting angle. Furthermore the most pronounced peaks ((111),(311),(222)) show a strictly monotonous trend of the shift with potential.
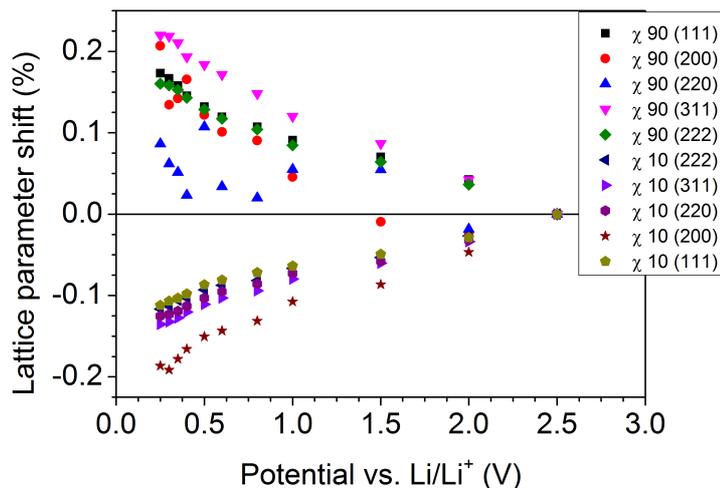
Figure 6.8: Shift of the lattice parameter with potential for all visible gold peaks in the 2Θ range of 20 to 90° relative to the lattice parameter measured at a potential of 2.5 V vs. Li/Li$^+$. The (200) and (220) peaks are very weak, when χ is 90° (see figure 6.7a for a typical Au (200) peak), which is the reason for the strong scatter.

The strong tilting angle dependent anisotropy indicates that the origin of the change in lattice parameter is elastic deformation, because composition induced changes should change the lattice parameter in an isotropic way. Due to the planar geometry of the sample with a rotational symmetry in the plane, the most likely state of deformation is a planar deformation, with only stress components along the film directions: A planar stress state. In case of a planar stress state, in-plane to out-of-plane strains should be related to each other according to $1 : (\nu - 1)$. With respect to a polycrystalline gold film, which has a Poisson's ratio of 0.42 [52], this means $1 : -0.58$. Figure 6.9 shows the in-plane to out-of-plane lattice parameter shifts of the most pronounced peaks ((111),(311),(222)). A linear fit of the relation of in-plane to out-of-plane lattice parameter shifts has a slope of -0.60 (relation of 1:-0.6), which is very close to what would be expected for a simple planar stress state. The obvious conclusion is that the source of the lattice parameter shift is a planar stress state, without any other significant contributions.

The peak broadening was analysed according to the theory by Warren and Averbach, presented in chapter 3. For this purpose the (111) and (222) peaks, measured at a tilting angle of $\chi = 90°$ at different potentials, as well as the reference peaks were fit by symmetrical pseudo-Voigt functions. Warren Averbach analysis itself was done by a slightly adapted algorithm (the peak shape was changed from Pearson VII to symmetrical pseudo voigt) written by Jürgen Markmann, which had been used in [53]. This notebook uses only peak positions, maximum intensity, FWHM and shape factor to reconstruct the peaks for the analysis. The results of this analysis are displayed in figure (6.10). For calculating the mean column length equation (3.36) was used and showed, that the mean column length
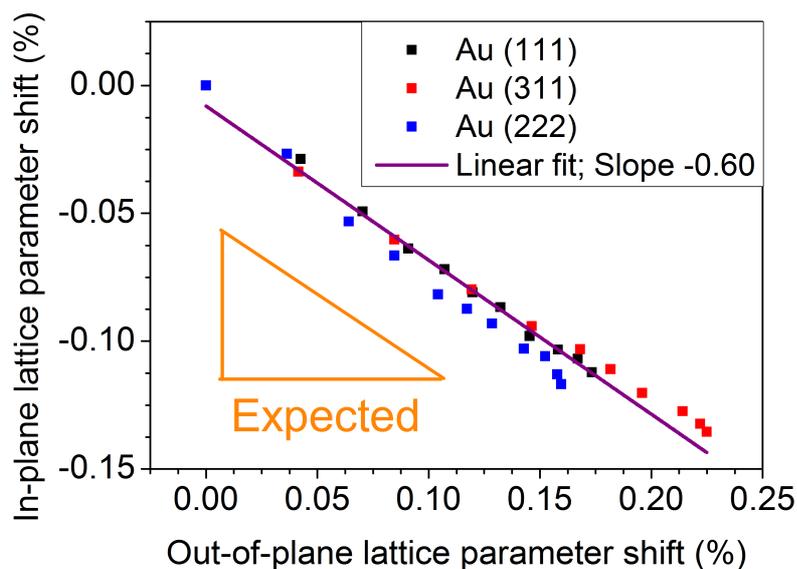
Figure 6.9: The change of the in-plane lattice parameter with respect to the change of the corresponding out-of-plane lattice parameter evaluated from (111), (311) and (222) peaks measured at different electrode potentials. The correlations show a linear behaviour with no significant deviations, regardless of the fact that different crystallographic orientations are compared. The linear fit of all displayed in-plane to out-of-plane lattice parameter shifts has a slope of -0.60. For the fit all reflexes were weighted equally. This slope is very close to the expected slope for a planar stress state of -0.58 as indicated by the orange slope triangle.

along the thickness of the film is in the range of 80 nm which is quite close to the film thickness of 100 nm and therefore indicates a columnar structure of the gold film.

The Warren-Averbach analysis (see in figure 6.10) shows a strong variation in distortion as well as a seemingly changing column length. The increase in column length with decreasing electrode potential is somehow doubtful since there are no indications for the appearance of new phases. It can be assumed, that this change in column length is a measurement artefact arising from the time gap between the measurement of the (111) and the (222) peak, during which the potential was kept constant, but the current did not vanish. This idea is strengthened by evaluating the contributions to the FWHM of the (222) peak from the grain size and the distortion, as shown in figure 6.11. The grain size contribution was estimated using Scherrer's equation [45]:

$$B_{\mathrm{CL}}(2\Theta) = \frac{0.94\lambda}{L\cos(\Theta)} \qquad (6.2)$$

where B_{CL} is the column length contribution to the FWHM in radians, L is the cube edge dimension of the coherently scattering domain and λ is the wavelength of the x-ray radiation. Obviously the grain size contribution is quite small and almost constant. Evaluating the distortion contribution B_{dist} was done by [53]:

$$B_{\mathrm{dist}} = \frac{\sqrt{8\pi(<\varepsilon^2> - <\varepsilon>^2)}\cos\Theta}{\sin\Theta} \qquad (6.3)$$

Obviously, the distortion contribution is mainly responsible for the changes of the peak broadening. Hence changes of the FWHM can be used as a measure for changes of the distortion, whereas apparent changes of the domain size, as evaluated by the Warren Averbach analysis, have to be assumed measurement artefacts.
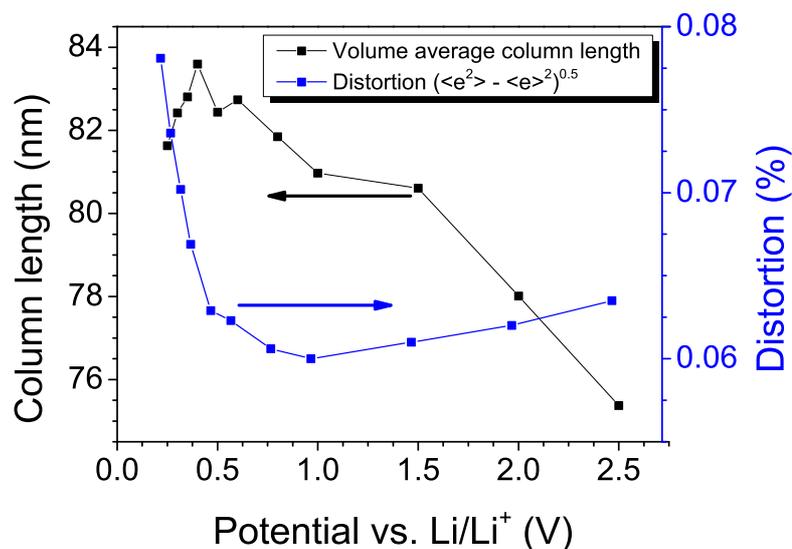
Figure 6.10: Results of the Warren-Averbach analysis for different potentials. The lines between the symbols are guides to the eye and have no physical meaning. The analysis shows significant changes of the distortion as well as the column length, where the distortion decays when the potential is reduced from 2.5 V to 1 V vs. Li/Li$^+$ and increases for further reductions of the electrode potential. The mean column length of the coherently scattering domains increases when the potential is reduced to a potential of 0.4 V vs. Li/Li$^+$ and decreases upon further reduction of the electrode potential.
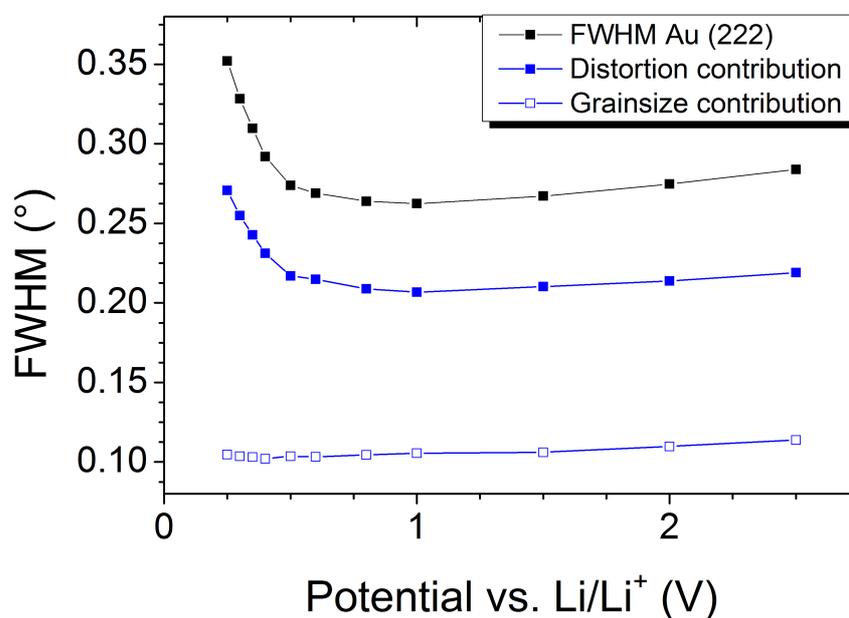
Figure 6.11: Change of the FWHM of the (222) peak measured at a tilting angle of $\chi = 90°$ (black) and the distortion contribution (massive blue; calculated using equation (6.3)) as well as the domain size contributions (empty blue; calculated using equation (6.2)). The lines between the symbols are guides to the eye and have no physical meaning.

6.3.2 X-ray diffraction during cyclic voltammetry
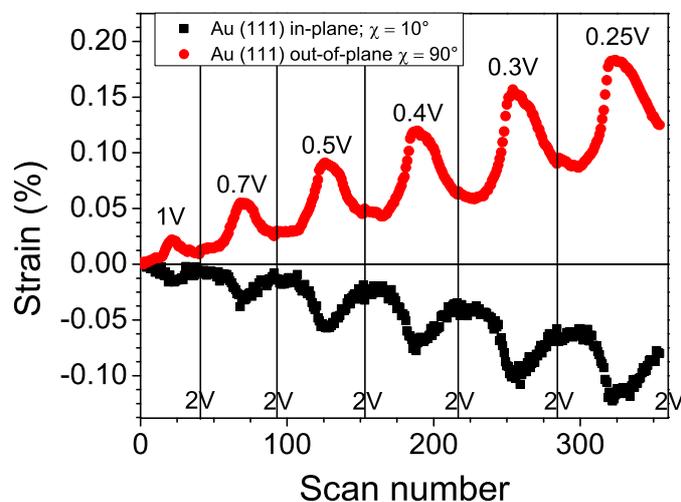
Figure 6.12: Change of the lattice parameter represented as strain values, calculated for the shift of the gold (111) peak position of the 55 nm thick gold film. The second value was chosen as the arbitrary reference. The vertical lines separate the results from different CV's and therefore indicate a time-gap during which the measurement was performed at the other tilting angle.

Similarly to potential strain coupling parameter measurements, x-ray diffraction was performed for a 55 nm thick gold film sputtered on a polyimide foil with roughly 20 nm of titanium in between, which acts as an adhesion layer. On the opposite side of the foil a roughly 150 nm thick copper film was sputtered which was used to test for measurement artefacts like substrate deformation and hight de-adjustment. The results of the copper reference peak are displayed in figure 5.10. For quantitative analysis the CV scans in the potential window of 2 to 0.3 V are used during which the the copper peak shifts roughly 5e-4° at a tilting angle of $\chi = 10°$, while peak changes for about 0.0225° leading to the conclusion, that measurement artefacts due to hight de-adjustment and substrate bending are at most responsible for an underestimation of the peak position shift of 2% during this cycle. Regarding the tilting angle of $\chi = 90°$ the shift of the copper peak is even less and the change of the gold peak position is higher, indicating that the underestimation due to substrate bending and hight de-adjustment is even less than 2% of the measured peak-shift.

Figure 6.12 shows the change of the strain values relative to the second measurement during 6 CV cycles for the 55 nm thick gold film. They were calculated from peak positions of the gold (111)-peak measured at a tilting angle of $\chi = 90°$ and $\chi = 10°$. Both, in-plane as well as out-of-plane strain changes are mainly reversible with cycling but occur in inverse directions. This is similar to the behaviour observed for measurements at constant potential and therefore suggests a planar stress state as the origin of the lattice parameter shift. This electrochemically induced planar stress state can either be caused by a changing surface stress or changes of the stress free planar dimensions of the sample that are counteracted by the substrate, according to equation (4.26). Changes of the equilibrium lattice parameter should shift the lattice parameter in a symmetrical way. The fact that the in-plane to out of plane lattice parameter change is -0.61 (see figure 6.13b) and therefore very close to the theoretical value of -0.58, shows that a planar stress state explains all the observed changes.

The FWHM is used as a measure for peak broadening as suggested by Warren Averbach analysis shown earlier. Values measured during cyclic voltammetry at a tilting angle of $\chi = 90°$ are displayed
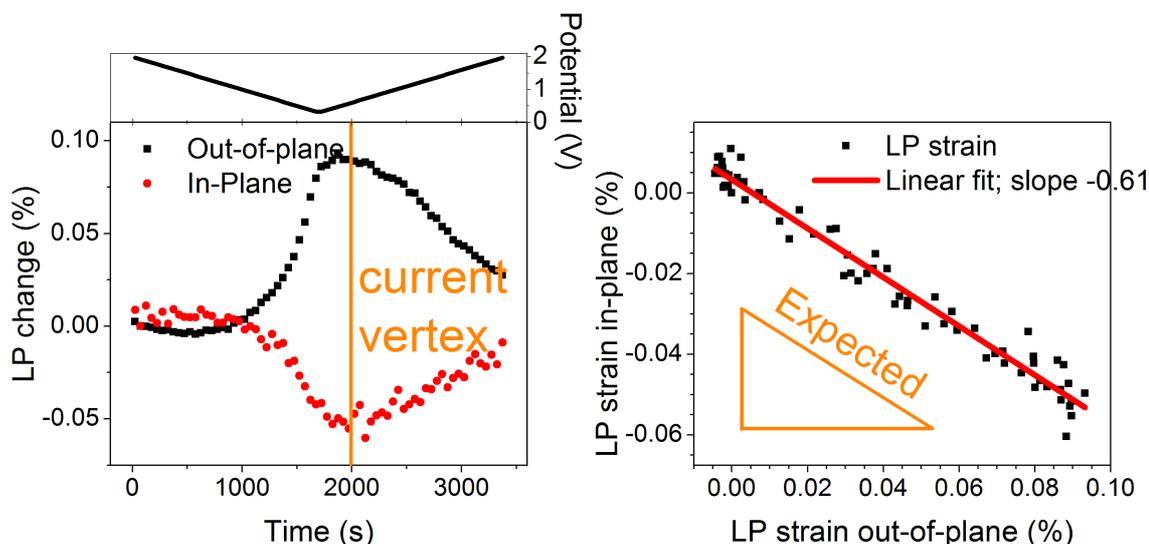
Figure 6.13: **a)** Strain values, relative to the second value displayed, calculated from (111)-lattice parameters measured during the CV from 2 V to 300 mV vs. Li/Li$^+$ for tilting angles $\chi = 90°$ (black) and $\chi = 10°$ (red) of a 55 nm Au sample. The orange line indicates where the current changed it's sign. The applied potential is displayed directly above. **b)** The tilting angle dependent lattice parameter strain values plotted against each other. The in-plane to out of plane lattice parameter changes are proportional to each other. The proportionality is very similar to an expected proportionality for a planar stress state as indicated by the orange slope triangle.
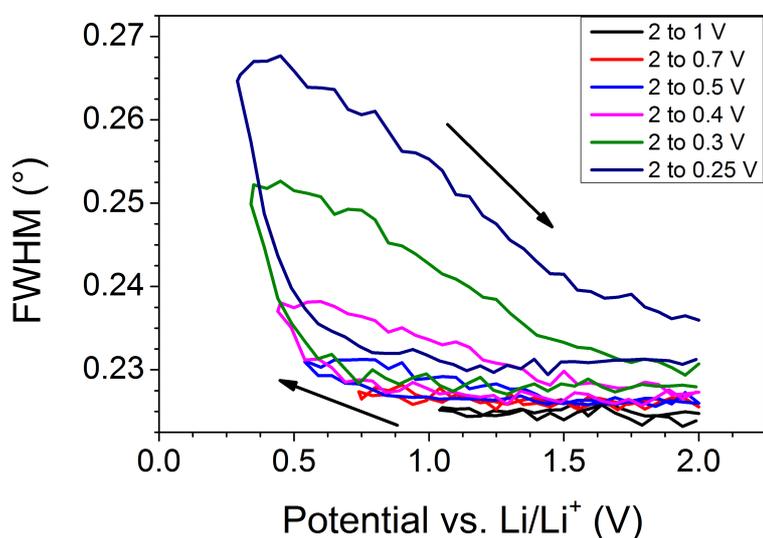
Figure 6.14: FWHM measured for a 55 nm gold film during cyclic voltammetry at a tilting angle of $\chi = 90°$ plotted vs. the electrode potential. In the negative scan direction, at a potential of roughly 0.6 V Li/Li$^+$ the FWHM starts to increase significantly. Upon inversion of the scan direction, the FWHM slowly returns to the starting value. Only after reaching 0.3 V vs. Li/Li$^+$ the FWHM is not recovered for the following cycle.

in figure 6.14. During cyclic voltammetry the FWHM significantly changes, where most of the change is reversible. In the negative scan direction the FWHM is almost constant until the potential reaches roughly 600 mV, where it starts to increase significantly. In the positive scan direction a roughly linear decay of the FWHM is visible. Only when reaching values of less than 0.4 V the FWHM does not fully recover until the following cycle starts. Such reversible distortion typically observed for an inhomogeneous elastic deformation.

7 Discussion

7.1 Dynamic electro-chemo-mechanical analysis

7.1.1 The impact of pre-strain

Investigating the impact of pre-strain (see figure 5.7) focused on evaluating systematic errors due to pre-strain, hence only qualitative conclusions will be drawn for the underlying mechanisms. An obvious tendency is that the PSCP is shifted to more positive values when the pre-strain is increased from 0.5% to 1%. The magnitude of the shift is in the range of 150 to 200 mV. There is an exception to this increase, which is in the negative scan direction below 0.5 V and in the positive scan direction up to a potential of roughly 1.1 V vs. Li/Li$^+$, where no shift is visible. This range equals the potential range where an underpotential deposit of lithium is present at the gold surface. This can be interpreted in such a way that UPD is dominating the PSCP, while the PSCP of UPD is independent of the pre-strain. An alternative explanation would be that the PSCP of UPD is shifted to more negative potentials, with the consequence that the resulting shift of the combined PSCP is annihilated. The second possibility cannot be excluded using the results at hand, but it seams rather unlikely that two different effects annihilate each other in the whole potential range, where both are active.

A rather surprising result of the impact of pre-straining is that the PSCP curves shift to more positive ς values with increases pre-strain. According to equation (4.5) this indicates that the compliance values increase with lithium concentration. Later on in this chapter it will be shown that the main bulk contribution to the PSCP is a grain boundary alloying induced apparent surface stress. One could speculate that lithium, when it enters gold grain boundaries, occupies "vacant" sites, and that this actually increases the compliance values of the grain boundaries. Based on the present results, this assumption is highly speculative, but might be worth looking into in more detail.

7.1.2 The potential strain coupling parameter of ltihium underpotential deposition

The CV curves measured during DECMA displayed in figure 6.6 hardly change with cycling. This is a strong indication that electrolyte decomposition gives only a small contribution to the measured currents.

The history dependency of the PSCP, which appears at the same time as the UPDs peak, as shown in figure 6.6, indicates that at least two mechanisms are active. Hence the measured PSCP is at least in some potential ranges a combined PSCP, where one of the contributions is UPD. The calculation of the combined PSCP does not require any restrictions on whether the contributions are linked to just one mechanism. Therefore equation (4.14) can be used to separate the contribution of UPD from all other contributions. For this purpose the effective capacities of both contributions, as well as the combined PSCP and the PSCP without underpotential deposit are required. Since these values are not known, only estimations can be made.

The most pronounced impact of the underpotential deposit on the CV curve is the UPDs peak, which has its maximum at a potential of 1.04 V vs. Li/Li$^+$. Hence this is where the mechanism of UPD should have the highest impact on the PSCP, making it the potential of choice for estimating the PSCP of UPD. Furthermore, the measured PSCP value at that potential is hardly dependent on the

pre-strain as visible in fugure 5.7. Hence effects of the pre-strain can be neglected.

A first obvious observation is that the PSCP measured during CV curves without UPD (e.g. for a potential window of [2 V to 0.7 V]) at an electrode potential of 1.04 V vs. Li/Li$^+$ in the positive scan direction is much higher ($\varsigma = 1.35$ V) than for CV curves with UPD like the one in the potential window of [2 V to 0.3 V] ($\varsigma = 0.9$ V). Together with the fact that effective capacities can only be positive, this observation leads to the conclusion that the PSCP of UPD is lower than 0.9 V.

When estimating the proportions of the effective capacities by the measured currents, it is possible to evaluate the PSCP of UPD. A possibility to do this is to compare the currents measured during one CV scan at a potential of 1.04 V vs. Li/Li$^+$ for both scan directions. The underlying assumption for this estimation is that the current which is not related to UPD only depends on the change in electrode potential, and that the potential of interest is sufficiently far away from the vertex potentials, so that influences of the change in scan direction are negligible. Choosing the current densities measured at a potential of 1.04 V during the CV with a potential window of [2 V to 0.25 V][1], which are -0.5 and 1.23 μA/cm^2 for the negative and positive scan directions respectively, leads to proportions of $C^{UPD} : C^C = 0.73 : 1.23$ and $C^{other} : C^C = 0.5 : 1.23$. Using these proportions, the combined PSCP of 0.9 V as well as a PSCP without UPD of 1.35 V in equation (4.14) leads to a PSCP for UPD of 0.59 V. In a later part of this discussion it will be shown that the second contribution is a bulk effect. Hence it can be estimated that the dynamics of UPD is higher than the dynamics of the second contribution, which makes the evaluation a lower bound.

The evaluated upper and lower bounds calculated up to this point naturally refer to values of a rough surface. In order to get bounds for the real local PSCP of underpotential deposition the impact of the roughness has to be considered. Using the roughness factor of 1.069 (Real surface area/projected surface area) and a poisson's ratio of 0.42 in equation (6.1) leads to an attenuation factor of 1.19. Hence the upper and lower bounds need to be multiplied with 1.19 in order to get bounds for the local PSCP of underpotential deposition leading to an interval of 0.7 V$< \hat{\varsigma_{UPD}} < 1.07$ V.

In 2013 Tavassol *et al.* published density functional theory (DFT) results for UPD induced changes of the surface stress. According to their results UPD of one monolayer of lithium on a (111) oriented gold surface induces a surface stress of -2.8 N/m [12]. The change in surface charge density correlated to the UPD of one monolayer of lithium on a (111) oriented gold surface (Δq) can be calculated by:

$$\Delta q = -q_0 \frac{2}{\sqrt{3}a_{(111)}^2} = -3.35 \text{C/m}^2 \tag{7.1}$$

where $a_{(111)}$=2.35 Å is the (111) lattice parameter of gold and q_0 is the elementary charge. Using the definition of the PSCP (equation 3.8) one can calculate $< \varsigma_{UPD} >= \Delta f/\Delta q = 0.84$ V, which is well within the interval evaluated from the measurement results presented here.

7.2 Microstructural characterisation

Similarly to the results measured at constant potential, tilting angle dependent changes measured during cyclic voltammetry indicate a planar stress state as the origin of lattice parameter changes. In order to get more information on the origin of the strain it is useful to compare the results to literature results measured by cantilever bending. For this comparison the mechanism is important, because changes of the gold lattice parameter show an anti-parallel change for surface stress changes and accretion of active material which corresponds to a numerically equal change of the apparent surface stress. This is in contrast to the signal recorded by substrate bending experiments, which measure the sum of real and

---

[1]It can be expected, that for this potential window contributions of electrolyte decomposition are smallest because it is the last scan.

apparent surface stress changes. Hence a comparison gives an indication on whether surface or bulk contributions are the major contribution to the strain. Recently Tavassol *et al.* published cantilever bending results of 50 nm thick gold films [12]. Their results will be used for the comparison. It has to be emphasised that the comparison is not straight forward because both measurements use different substrates. The importance of the substrate stiffness is highlighted by the evaluations presented in section 4.3. Substrate bending experiments use glass substrates, which are quite stiff, whereas the polyimide substrate used for x-ray diffraction is rather soft. Additionally the stiffness of the polyimide might be reduced when solvents are present in the polyimide. In such a case, the solvents can redistribute to relax stresses. Unfortunately no precise value for the effective substrate stiffness is available. For being able to do the comparison two different cases will be assumed. In the first case, it is assumed, that the change in lattice parameter is the result of a changing real surface stress and in the second case, it is assumed, that the change in lattice parameter results from the accretion of lithium. For both cases the real/apparent surface stress is calculated by using minimum assumptions. For the real surface stress minimum assumptions means neglecting the stiffness of the polyimide (). In this case the surface stress can be calculated by:

$$f = -\varepsilon_\parallel (B_{Au} h_{Au} + B_{Ti} h_{Ti}) \tag{7.2}$$

with materials parameters for Ti and Au according to table 7.1. For estimating the minimum apparent surface stress due to accreation of lithium, as measurable by cantilever bending experiments, from changes of the lattice parameter, the stiffness of the polyimide is assumed according to typical materials parameters, with consequently negligible substrate deformation. In this case the apparent surface stress can be calculated by:

$$f^{app} = \varepsilon_\parallel B_{Au} h_{Au} \tag{7.3}$$

The comparison using this minimum assumptions is displayed in figure 7.1. It is quite obvious that the assumption of an apparent surface stress due to the accretion of lithium is responsible for the change in lattice parameter shows a good correlation to cantilever bending results, whereas the assumption that a real surface stress is the origin for the change in lattice parameter does not fit at all. Hence it can be concluded that the change in lattice parameter mainly results from bulk mechanisms. This conclusion is strengthened by the observation, that the only regions, where the change in lattice parameter and the cantilever results show a different behaviour is the potential of UPD and UPDs, and the obvious drift in lattice parameter, which might result from SEI formation. In contrast to cantilever bending results, there is no feature corresponding to UPD and UPDs in the measured changes of the lattice parameter, hence it has to be assumed that surface effects have at most a small impact on the observed lattice parameter changes.

The change in lattice parameter shows a certain drift, which is not visible in the cantilever bending results. There are several possible explanations for this drift. All of them have in common that they are either irreversible or that their time constant is higher than the characteristic time of the electrochemical cycles. One possible origin is the formation of the SEI (solid electrolyte interface). According to Tavassol *et al.*, the SEI can induce a positive surface stress [12], which would induce a drift in the observed direction. Since Tavassol *et al.* used a different electrolyte, this is only an estimation, on the other hand, the different electrolyte might explain why the cantilever bending results do not show any drift. Another possibility is that the drift results from a slow diffusion mechanism. Later on, it will be shown that grain boundary reactions are a main contribution to the apparent surface stress, hence the slow diffusion mechanism could be diffusion of lithium atoms from the grain boundaries into the bulk of the gold grains. The impact of such a mechanism would decay with electrochemical cycling and vanish when the mean concentration equals the equilibrium concentration of lithium in the gold grains at the mean electrode potential. Unfortunately there was no information on the electrochemical pretreatment of the sample before the measurement was performed in [12], hence this possibility can neither be strengthened nor excluded.
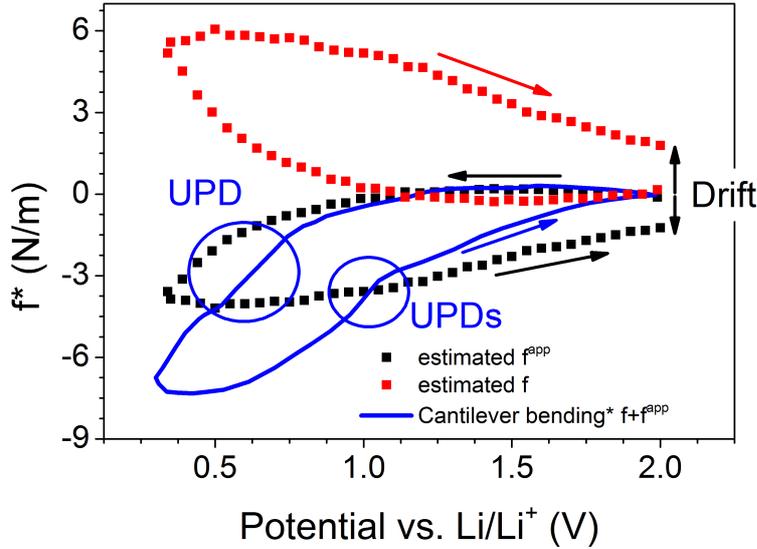
Figure 7.1: Qualitative comparison of estimated cantilever bending results calculated from changes of the lattice parameter, assuming surface effects (red) or bulk effects (black) to literature cantilever bending results (blue) as published by Tavassol *et al.* [12]. The estimated cantilever bending results use minimum assumptions by neglecting the polyimide substrate stiffness in case of surface effects and neglecting stress relaxation in case of bulk effects. Due to the uncertain effective stiffness of the polyimide the comparison only provides qualitative information.

7.3 Comparison of dynamic electro-chemo-mechanical analysis and x-ray diffraction results

The interrelation of the PSCP and the change in lattice parameter is evaluated in section 4.3. Under the assumption that the real surface stress does not change, this interrelation can be written as:

$$\varsigma = \frac{d(f + f^{app})}{d(q + q^{app})} \stackrel{df/dq=0}{\approx} B_{Au} h_{Au} \frac{d\varepsilon_{\parallel}}{d(q + q^{app})} \tag{7.4}$$

For comparison it is useful to multiply equation 7.4 with the current density, which leads to:

$$\varsigma \underbrace{\frac{d(q + q^{app})}{dt}}_{=I/A} \stackrel{df/dq=0}{\approx} B_{Au} h_{Au} \underbrace{\frac{d\varepsilon_{\parallel}^e}{d(q + q^{app})} \frac{d(q + q^{app})}{dt}}_{=d\varepsilon_{\parallel}^e/dt} \tag{7.5}$$

As discussed earlier, the interrelation of apparent surface stress and the elastic strain depends on the substrate, or more precisely on the effective stiffness of the substrate. For DECMA, the stiffness of the substrate defines the relation of the substrate strain and the sample strain. Due to the low characteristic time of 50 ms, it can be assumed that creep relaxation does not play any role for DECMA. Consequently the elastic properties provided by the supplier should be suitable for estimating that the difference in strain variation of the substrate and the sample is negligible. For in-situ x-ray diffraction, the situation is different. Due to the high characteristic time of one CV cycle, in the range of one hour, creep relaxation has to be considered. This is even more important since the sample is in contact with organic solvents. As a consequence it has to be considered that the effective stiffness of the polyimide
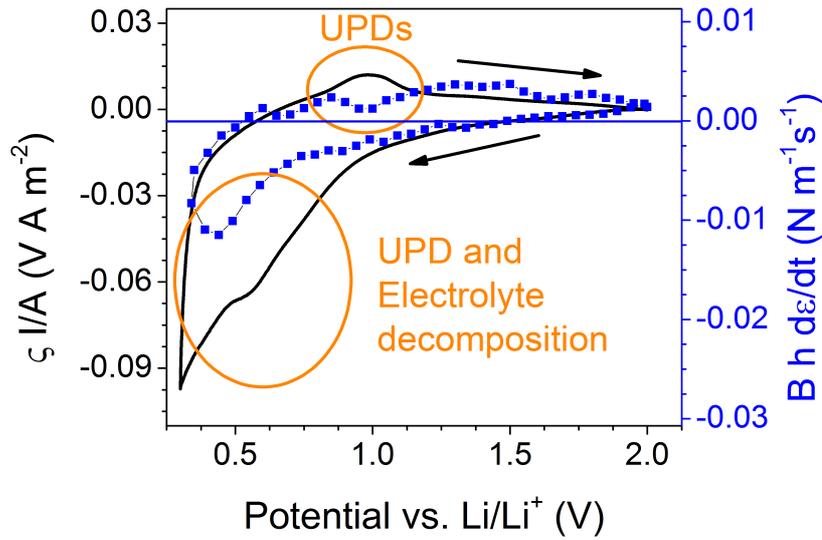
Figure 7.2: Comparison of the right (blue) and left hand side (black) of equation (7.5). In a wide potential range both curves show a very similar behaviour. Significant deviations are only visible, where the UPDs peak is visible and in the potential range, where electrolyte decompostion and UPD should occur. The zero offset results partly from the irreversible drift of the lattice parameter.

differs for both experiments. In order to estimate the resulting influence on the comparison, it was assumed that for slow measurements (x-ray diffraction) the polyimide behaves soft whereas for fast measurements (DECMA) it behaves stiff. This assumption leads to a difference in the left and right hand side of equation (7.5) by a factor of 3 ($\frac{B_{Ti}h_{Ti}}{B_{Ti}h_{Ti}+B_{Au}h_{Au}} : \frac{B_{Ti}h_{Ti}+B_{Pi}h_{Pi}}{B_{Ti}h_{Ti}+B_{Pi}h_{Pi}+B_{Au}h_{Au}} \approx 1 : 3$, where $B_{Pi}h_{Pi}$ is the planar stiffness of the polyimide according to the supplier), when using materials parameters according to table 7.1. A corresponding comparison of both sides of equation (7.5) is shown in figure 7.2, taking into account the factor 3 by the different scale. Like the comparison of lattice parameter changes to cantilever bending results, this comparison shows a quite good correlation in a wide potential range as well as deviations where UPD and UPDs appears. Additionally to this there is a rather pronounced difference below 1 V in the negative scan direction, which is most probably linked to electrolyte decomposition, which can appear when the SEI is not complete or has partly been dissolved in the electrolyte. Dissolution can be expected to occur in the in-situ electrochemical cell, which contains a significant amount of electrolyte in contrast to the miniaturised cell used for DECMA.

Table 7.1: Materials parameters for the typical components of a sample [54].

Material	thickness (nm)	Elastic modulus (GPa)	Poisson's ratio ratio	Biaxial modulus (GPa)	Planar stiffness (N/mm) [a]
Polyimide[b] *	75000	2.5	0.34	3.8	0.285
Polyimide[c]	75000	0	0.34	0	0
Titanium	≈20	110	0.33	164	0.0033
Gold	55	78	0.42	134	0.0074

[a] The "Planar stiffness" is a product of the biaxial modulus and the thickness, which relates an apparent surface stress to a strain.

[b] fast

[c] slow

* According to supplier

The comparison in figure 7.2 shows an offset between both curves. One contribution to this offset is the drift, which is naturally correlated to a slow mechanism and therefore not contributing to the DECMA results. Correcting the drift by assuming that it is constant during the measurement would shift the $Bh\mathrm{d}\varepsilon/\mathrm{d}t$ values to roughly 4e-4 Nm^{-1}s^{-1} higher values, which equals about 50% of the offset. A second possible contribution to an offset are Faradaic currents due to decomposition of impurities like dissolved oxygen or H$_2$O. Unfortunately this impact is not quantifiable from the data. It can be estimated, that a correction of the effect should should shift the $\varsigma I/A$ curve to higher values and therefore reduce the offset, because the PSCP is positive in the whole potential range and a decomposition current is negative. It has to be empathised that the impact of decomposition reactions should be higher at lower potentials, which does not fit nicely to the comparison. Hence it can be assumed, that decomposition of impurities has at most a small effect on the offset. Another possible contribution to the offset are the different time-scales of the measurements: While DECMA is sensitive only to fast processes, for which the chemical potential equals the chemical potential at the surface, changes of the lattice parameter are influenced by slow processes, like diffusion controlled processes, as well. A corresponding effect would change the results in such a way, that the current measured during cyclic voltammetry overestimates the capacity contributing to the PSCP at this potential. Together with the observation that the PSCP is higher at lower potentials, $\varsigma I/A$ would overestimate $Bh\mathrm{d}\varepsilon/\mathrm{d}t$, where the effect would increase with measurement time up to the current vertex. The deviations of both contributions seem to become bigger with distance to the vertex potential, hence it is likely that the different time constant contributes to the offset. Unfortunately this effect is not quantifiable neither with the data at hand.

7.4 Microscopic mechanisms

In the last part it was shown that mechanisms inside the bulk of the thin film are an important contribution to the PSCP of gold films in lithium electrolyte, even at a potential where no phase transitions appears. A change of the apparent surface stress requires a stress free strain in the plane of the film. Such a stress free strain can only result from a creation of new lattice places or an increase of the grain boundary thickness. Since gold and lithium form a substitutional solid solution, the lattice can only be changed at grain boundaries, surfaces or dislocations [38]. Hence the observed change in lattice parameter can only be a result of lithium entering grain boundaries dislocations or vacancies (defect alloying). When lithium enters vacancies, the volume should hardly change (lattice parameter is only slightly dependent on the lithium concentration) and the changes should be isotropic and reduce the lattice parameter, hence a corresponding mechanism can neither explain the sign and magnitude of the PSCP nor the observed tilting angle dependency of the lattice parameter change. Furthermore the results indicate that UPD and apparent surface stresses are the main contributions to the PSCP, and that the impact of UPD appears only when potentials of less than 700 mV are reached. Consequently PSCP values measured during cyclic voltammetry in the potential range of 2 V to 0.7 V are mainly governed by defect alloying. This can be used to evaluate an effective strain concentration coefficient $\eta_\parallel^{\mathrm{eff}} = \eta \mathrm{d}q^{\mathrm{app}}/\mathrm{d}(q + q^{\mathrm{app}})$, by using equation 3.18 and materials parameters of table 7.1. Corresponding results are shown in figure 7.3. It has to be emphasised that the PSCP values used for this calculation suffer from the observed shift due to the pre-strain as displayed in figure 5.7. Because the effect of prestrain was not investigated in detail, the impact can only be estimated. Subtracting the estimated impact would shift $\eta_\parallel^{\mathrm{eff}}$ to ≈ 0.02 lower values.

The calculated $\eta_\parallel^{\mathrm{eff}}$ values show a strong dependency on the electrode potential. When lithium enters dislocations, it has to create a new lattice place, to fit to the surrounding ordered structure. For a mechanism like this it is possible to evaluate the strain-concentration coefficient using lattice parameter values of different gold lithium concentrations (table 2.1) to be 0.33 (1/3 for creation of a new lattice place and ≈ -0.003 due to the reduced lattice parameter). This value is much higher
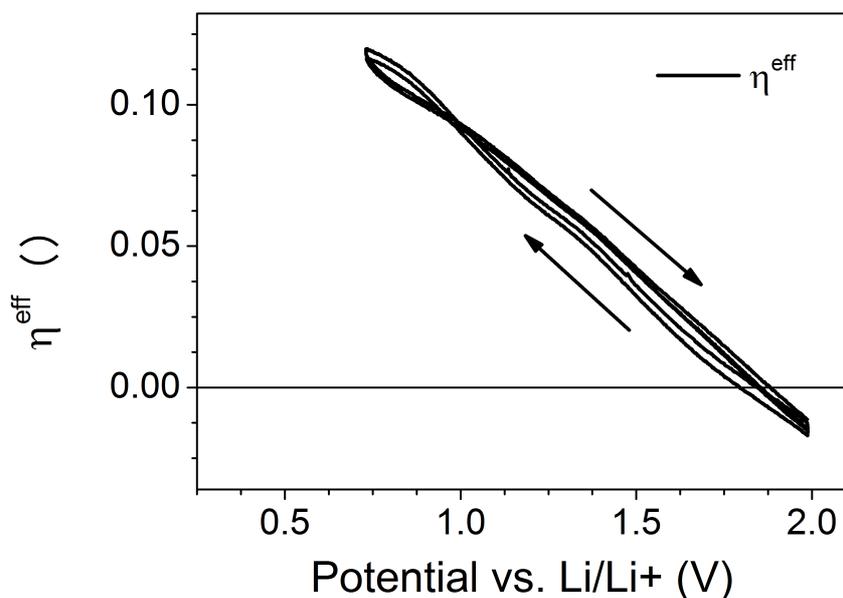
Figure 7.3: Effective planar strain-concentration coefficient $\eta_\parallel^{\text{eff}}$ of an Au film in LP30 as a function of the applied potential. The values presented here were not corrected for potential contributions of the pre-strain to the PSCP, hence they probably overestimate the actual values. It can be estimated, that the evaluated values are about 0.02 V too high.

than the ones calculated from the PSCP results. In case of grain boundaries and especially high angle grain boundaries, such a highly ordered regime does not exist. Consequently, it can be expected that lithium should be able to enter them with significantly less stress-free strain which corresponds to lower $\eta_\parallel^{\text{eff}}$ values. Hence the measured results are a strong indication that the PSCP is mainly governed by lithium entering grain boundaries. This result is further strengthened, by the finding that samples with higher thickness and therefore higher grain-size and lower number of grain boundaries per volume [55] show lower currents during cyclic voltammetry as displayed in figure 7.4. Additionally grain boundary alloying fits reversible changes of the distortion as indicated by the reversible FWHM. The reason for this reversible change is that for an arbitrary grain size distribution the increase in grain boundary thickness deforms small grains more than big ones, which is visible in a broadening of the peak. In case lithium enters dislocations and creates new lattice places there, the dislocations have to migrate. One would expect that this would irreversibly create new distortions, visible as irreversible peak broadening. Such a behaviour is only observed, when the lower potential reaches values of less than 0.4 V, in which case the following cycle starts at higher FWHM values (see figure 6.14). Knowing the processes active in the potential range of 2 to 0.25 V vs. Li/Li$^+$ allows to estimate the capacity. UPD of one monolayer of lithium corresponds to a capacity of C/m^2 when accounting for the roughness of the surface. Estimating the volume fraction of grain boundaries by taking the means grain size of 58 nm (not area weighted) and assuming a grain boundary thickness of 1 nm, hexagonal, columnar grains and a maximum lithium concentration in the grains of 39% leads to an estimated capacity of the grain boundaries of 12 C/m^2. Hence the overall capacity should be estimated to be roughly 16 C/m^2. The reversible charge transfer measured during one CV cycle in the potential range from 2 to 0.25 V vs. Li/Li$^+$ was roughly 12 C/m^2, which is very close to this estimated capacity.

Summing up, it can be concluded that UPD and grain boundary alloying are the main contribution to the PSCP for the gold lithium system in the potential range of 2 V to 0.25 V vs. Li/Li$^+$. It can be expected that the observed strong potential dependence of $\eta_\parallel^{\text{eff}}$ is important for effects like storage[56],
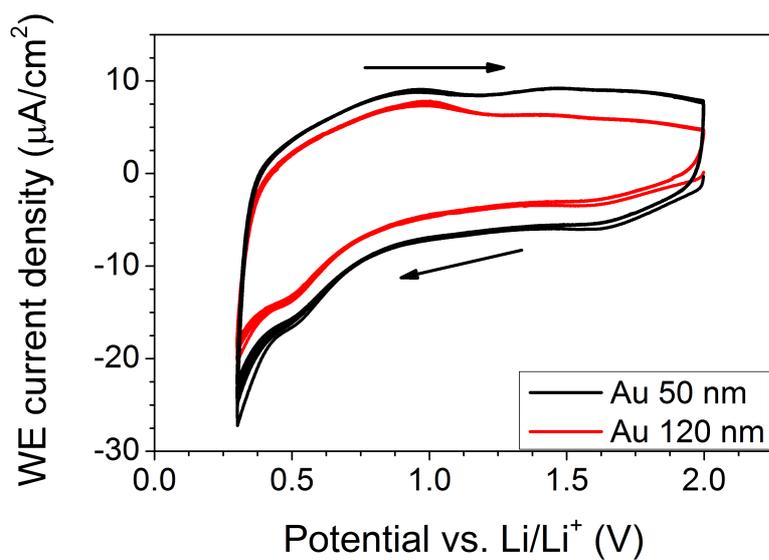
Figure 7.4: CV curves measured for two samples with different thickness at a scan speed of $10\,\mathrm{mV/s}$.
In the whole potential range, the current is higher for the thinner sample. The UPDs peak
is hardly visible, which results from the fact that the SEI had not been formed when the
measurement was performed.

trapping[57] and diffusion of lithium in grain boundaries.

8 Summary and outlook

8.1 Summary

The main topic of this thesis it the development of a method to separate surface and bulk contributions to the coupling of electrochemistry and mechanics. This development contains several aspects. First of all, a principle strategy for separating surface an bulk contributions is introduced and thermodynamic as well as mechanic principles are evaluated. In a second step, experimental devices for obtaining the required physical measures were designed, built and tested. Last but not least the strategy was applied to a model gold-lithium alloy electrode.

The strategy required theoretical evaluations of a combined PSCP, which stems from two different effects, each with its own PSCP. The evaluation showed that the measured PSCP is an effective capacity weighted average of the contributing mechanisms. Further evaluations focused the dependency of the elastic strain of the sample on changes of the real and apparent surface stress, including the substrate stiffness. It was shown, that a real surface stress has an impact on the elastic strain of the sample, which has an inverse sign and typically very different magnitude as the impact of a numerically equal apparent surface stress.

For measuring the PSCP in lithium electrolytes a customised DECMA-stage suitable for operation inside a glovebox was designed and tested. The setup was extended for a possibility to directly measure the strain of the substrate, which offers the possibility to precisely measure the constant pre-strain and improves the measurement precision of strain variations. Furthermore special care has been taken in order to increase the accessible frequency range and the stiffness of the whole setup. It turned out that this improvement in accessible frequency range could not be used for the system at hand, but might be useful for investigating other electrochemical systems. The possibility to measure the pre-strain was further used to estimate its impact on evaluated results.

Measurements of the PSCP at different values of pre-strain showed deviations of the measured PSCP. It could be evaluated, that a corresponding effect can result from changes of the compliance values with active material concentration. This finding could be used to estimate the impact of pre-strain on the measurement.

To demonstrate the possibility of measuring the PSCP in lithium electrolytes a gold thin film electrode was used. It could be shown, that the PSCP is strongly dependent on the electrode potential and changes in the range from $\approx -0.4 V$ at an electrode potential of 2 V vs. Li/Li$^+$ to 2.1 V at an electrode potential of 0.55 V vs. Li/Li$^+$. In a first step, the results were used to calculate an interval for the local PSCP of underpotential deposition of lithium on the gold surface. This interval was [0.7;1.07 V] which fits a corresponding value calculated from DFT results published by Tavassol *et.al.* of 0.83 V [12].

To show that bulk mechanisms are actually active in the system, in-situ x-ray diffraction was used. For this purpose a customised in-situ electrochemical cell was designed, which allows for measurements at arbitrary sample orientations and in a wide range of tilting angles to measure changes of the in-plane as well as out-of-plane lattice parameter. The measured changes of the lattice parameter correspond to strains in the range of 0.002% and -0.054% in-plane and -0.003% and 0.089% out-of-plane with respect to the value measured at 2 V vs. Li/Li$^+$ during a single CV cycle.

With the knowledge, that in a wide potential range mainly the bulk mechanism is responsible for

the coupling of electrochemitry and mechanics it could be concluded, that the effective concentration strain coefficient η_{ij}^{eff} needs to show a strong dependency on the electrode potential. A corresponding dependency is a strong indication for lithium entering grain-boundaries, because other possibilities for lithium entering the bulk (vacancies and dislocations) cannot explain the observed behaviour.

8.2 Outlook

Both custom made devices showed very promising performance and will hopefully be used for further investigations. The design of the in-situ electrochemical cell offers the possibility to investigate thin films during electrochemical cycling at a high sampling rate, almost independent from the orientation with a high accuracy. The DECMA-stage constructed for this work offers the possibility to perform measurements at frequencies of up to 2.5 kHz, while directly measuring the offset strain as well as strain variations, offering the possibility to investigate the frequency dependency of the PSCP.

8.2.1 Different materials

Some preliminary results of the PSCP measured for different materials have already been obtained in the course of this work, and are shown in figure 8.1. All PSCP curves show an almost linear dependency of the PSCP on the electrode potential in the vicinity of $\varsigma = 0$ with a slope of roughly -1.5. This similarity suggests, that the slope is independent on the material. Together with the finding, that the main contribution to the PSCP of the gold electrode is grain boundary alloying, this finding might indicate that a similar process is active in all the presented materials and that the slope of the PSCP of grain boundary alloying is independent on the material. Needless to say these conclusions are highly speculative, but might be worth looking into.
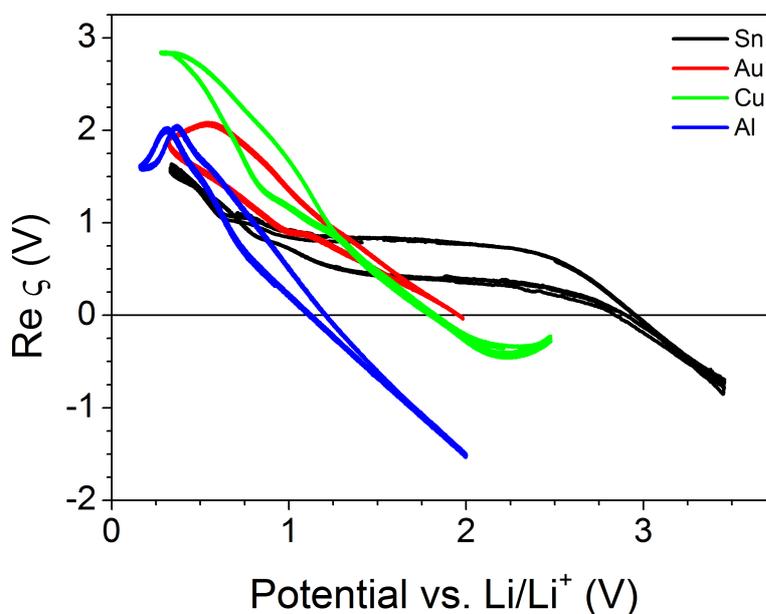
Figure 8.1: The PSCP measured for different materials during cyclic voltammetry with a scan-speed of 1 mV/s and a straining frequency of 20 Hz. For every sample three subsequent curves are displayed, which nicely overlap.

8.2.2 Impact of pre-strain

A side product of this work is, that it could be shown, that the pre-strain has an impact on the PSCP, and that this impact depends on the change in compliance values with concentration and is proportional to the stress. Consequently, measurements of the PSCP at different values of pre-strain should be suitable for evaluating the change in compliance values with concentration. With minor adoptions of the DECMA-stage, it should be possible to perform such measurements in a more quantitative way. In theory a corresponding investigation could be done by measuring the potential variation at twice the straining frequency, but a corresponding measurement would be sensitive to deviations from sinusoidal variations of the strain. Hence the author suggests to perform measurements at different values of pre-strain and to introduce an electrically controlled micrometre screw for continuous adjustments of the pre-strain.

9 Bibliography

[1] Zhang, W. J. A review of the electrochemical performance of alloy anodes for lithium-ion batteries *J. Power Sources* **196**, 13 (2011).

[2] Tarascon, J. M. and Armand, M. Issues and challenges facing rechargeable lithium batteries *Nature* **414**, 359 (2001).

[3] Christensen, J., Albertus, P., Sanchez-Carrera, R. S., Lohmann, T., Kozinsky, B., Liedtke, R., Ahmed, J., and Kojic, A. A Critical Review of Li/Air Batteries *J. Electrochem. Soc.* **159**, R1 (2012).

[4] Huggins, R. A. Lithium Alloy Anodes In *Handbook of Battery Materials 2nd Edition*, Wiley-VCH Weinheim, Germany, 405 (2011), Daniel C., Besenhard J. O., Editors, ISBN: 978-3-527-32695-2.

[5] Fauteux, D. and Koksbang, R. Rechargeable lithium battery anodes: alternatives to metallic lithium *J. Appl. Electrochem.* **23**, 1 (1993).

[6] Mukhopadhyay, A. and Sheldon, B. W. Deformation and stress in electrode materials for Li-ion batteries *Prog. Mater. Sci.* **63**, 58 (2014).

[7] Song, M. K., Park, S., Alamgir, F. M., Cho, J., and Liu, M. Nanostructured electrodes for lithium-ion and lithium-air batteries: The latest developments, challenges, and perspectives *Mater. Sci. Eng. R Reports* **72**, 203 (2011).

[8] Deshpande, R., Cheng, Y. T., and Verbrugge, M. W. Modeling diffusion-induced stress in nanowire electrode structures *J. Power Sources* **195**, 5081 (2010).

[9] Hao, F., Gao, X., and Fang, D. Diffusion-induced stresses of electrode nanomaterials in lithium-ion battery: The effects of surface stress *J. Appl. Phys.* **112** (2012).

[10] Sethuraman, V. A., Chon, M. J., Shimshak, M., Srinivasan, V., and Guduru, P. R. In situ measurements of stress evolution in silicon thin films during electrochemical lithiation and delithiation *J. Power Sources* **195**, 5062 (2010).

[11] Mukaibo, H., Momma, T., Shacham-Diamand, Y., Osaka, T., and Kodaira, M. In Situ Stress Transition Observations of Electrodeposited Sn-Based Anode Materials for Lithium-Ion Secondary Batteries *Electrochem. Solid-State Lett.* **10**, A70 (2007).

[12] Tavassol, H., Chan, M. K. Y., Catarello, M. G., Greeley, J., Cahill, D. G., and Gewirth, A. A. Surface Coverage and SEI Induced Electrochemical Surface Stress Changes during Li Deposition in a Model System for Li-Ion Battery Anodes *J. Electrochem. Soc.* **160**, A888 (2013).

[13] Gao, Y. F. and Zhou, M. Coupled mechano-diffusional driving forces for fracture in electrode materials *J. Power Sources* **230**, 176 (2013).

[14] Biener, J., Wittstock, A., Zepeda-Ruiz, L. A., Biener, M. M., Zielasek, V., Kramer, D., Viswanath, R. N., Weissmüller, J., Bäumer, M., and Hamza, A. V. Surface-chemistry-driven actuation in nanoporous gold. *Nature Mater.* **8**, 47 (2009).

[15] Kitzler, T., Maawad, E., Többens, D. M., Ziehmer, M., and Markmann, J. The Electro-Chemo-Mechanical Coupling in Lithium Alloy Electrodes and Its Origins *J. Electrochem. Soc.* **162**, A2684 (2015).

[16] Koch, R. The intrinsic stress of polycrystalline and epitaxial thin metal films *J. Phys. Condens. Matter* **6**, 9519 (1994).

[17] Chason E., Sheldon B. W., FreundL. B. , Floro J. a., and Hearne S. J., Origin of compressive residual stress in polycrystalline thin films. *Phys. Rev. Lett.* **88**, 156103 (2002).

[18] Mukhopadhyay, A., Tokra, A., Xiao, X., and Sheldon, B. W. Stress development due to surface processes in graphite electrodes for Li-ion batteries: A first report *Electrochim. Acta* **66**, 28 (2012).

[19] Nadimpalli, S. P. V., Sethuraman, V. A., Bucci, G., Srinivasan, V., Bower, A. F., and Guduru, P. R. On Plastic Deformation and Fracture in Si Films during Electrochemical Lithiation/Delithiation Cycling *J. Electrochem. Soc.* **160**, A1885 (2013).

[20] Ichitsubo, T., Yukitani, S., Hirai, K., Yagi, S., Uda, T., and Matsubara, E. Mechanical-energy influences to electrochemical phenomena in lithium-ion batteries *J. Mater. Chem.* **21**, 2701 (2011).

[21] Sethuraman, V. A., Srinivasan, V., Bower, A. F., and Guduru, P. R. In Situ Measurements of Stress-Potential Coupling in Lithiated Silicon *J. Electrochem. Soc.* **157**, A1253 (2010).

[22] Kienast, G., Verma, J. Das Verhalten der Alkalimetalle zu Kupfer, Silber und Gold *Zeitschrift für Anorg. und Allg. Chemie* **310**, 143 (1961).

[23] Pelton, A. D. The Au-Li (Gold-Lithium) system *Bull. Alloy Phase Diagrams* **7**, 228 (1986).

[24] Aurbach, D., Daroux, M., Faguy, P., and Yeager, E. The electrochemistry of noble metal electrodes in aprotic organic solvents containing lithium salts *J. Electroanal. Chem. Interfacial Electrochem.* **297**, 225 (1991).

[25] Kulova, T. L., Skundin, A. M., Kozhevin, V. M., Yavsin, D. A., and Gurevich, S. A. A study of lithium insertion into electrodes with thin gold films *Russ. J. Electrochem.* **46**, 877 (2010).

[26] Renner, F., Kageyama, H., Siroma, Z., Shikano, M., Schöder, S., Gründer, Y., and Sakata, O. Gold model anodes for Li-ion batteries: Single crystalline systems studied by in situ X-ray diffraction *Electrochim. Acta* **53**, 6064 (2008).

[27] Zhang, X., Kostecki, R., Richardson, T. J., Pugh, J. K., and Ross, P. N. Electrochemical and Infrared Studies of the Reduction of Organic Carbonates *J. Electrochem. Soc.* **148**, A1341 (2001).

[28] Agubra, V. A. and Fergus, J. W. The formation and stability of the solid electrolyte interface on the graphite anode *J. Power Sources* **268**, 153 (2014).

[29] Tasaki, K., Goldberg, A., Lian, J.-J., Walker, M., Timmons, A., and Harris, S. J. Solubility of Lithium Salts Formed on the Lithium-Ion Battery Negative Electrode Surface in Organic Solvents *J. Electrochem. Soc.* **156**, A1019 (2009).

[30] Bard, A. J. and Faulkner, L. R. *Electrochemical Methods: Fundamentals and Applications, Volume 6* Wiley, NY, USA (2001) ISBN: 0471043729.

[31] Beaulieu, L. Y., Larcher, D., Dunlap, R. A., and Dahn, J. R. Reaction of Li with Grain-Boundary Atoms in Nanostructured Compounds *J. Electrochem. Soc.* **147**, 3206 (2000).

[32] Magnfält, D., Abadias, G., and Sarakinos, K. Atom insertion into grain boundaries and stress generation in physically vapor deposited films *Appl. Phys. Lett.* **103**, 051910 (2013).

[33] Weissmüller, J., Viswanath, R. N., Kibler, L. A., and Kolb, D. M. Impact of surface mechanics on the reactivity of electrodes. *Phys. Chem. Chem. Phys.* **13**, 2114 (2011).

[34] Gokhshtein, A. Y. The Estance Method *Russ. Chem. Rev.* **44**, 921 (1975).

[35] Smetanin, M., Kramer, D., Mohanan, S., Herr, U., and Weissmüller, J. Response of the potential of a gold electrode to elastic strain. *Phys. Chem. Chem. Phys.* **11**, 9008 (2009).

[36] Deng, Q. *Dynamic Electro-Chemo-Mechanical Analysis at the Metal-Electrolyte Interface.* Phd. thesis, TUHH, (2014).

[37] Weissmüller, J. and Kramer, D. Balance of force at curved solid metal-liquid electrolyte interfaces *Langmuir* **21**, 4592 (2005).

[38] Larché, F. and Cahn, J. W. A Linear Theory of Thermochemical Equilibrium of Solids Under Stress *Acta Metall.* **21**, 1051 (1973).

[39] Weissmüller, J. Electrocapillarity of Solids and its Impact on Heterogeneous Catalysis In *Electrocatalysis, Volume 14* Wiley-VCH Weinheim, Germany, 163 (2013) Alkire R- C., Kolb D. M., Lipkowski J., Editors, ISBN: 978-3-527-33227-4.

[40] Shuttleworth, R. The Surface Tension of Solids *Proc. Phys. Soc. Sect. A* **63**, 444 (1950).

[41] Viswanath, R. N. and Weissmüller, J. Electrocapillary coupling coefficients for hydrogen electrosorption on palladium *Acta Mater.* **61**, 6301 (2013).

[42] Balogh, Z. and Schmitz, G. Diffusion in Metals and Alloys In *Physical Metallurgy, 5th Edition*, Elsevier Amsterdam, Netherlands, 387 (2014) Laughlin D., Hono K., Editors, ISBN: 9780444537706.

[43] Dey, A. N. Electrochemical Alloying of Lithium in Organic Electrolytes *J. Electrochem. Soc.* **118**, 1547 (1971).

[44] Chromik, R. and Cotts, E. Thermodynamic and Kinetic Study of Phase Transformations in Solder/Metal Systems *MRS Proc.* **445**, 31 (1996).

[45] Warren, B. E. *X-ray Diffraction* Dover Publications inc., New York, USA, 1 (1990) ISBN: 0486663175

[46] Warren, B. E. and Averbach, B. L. The Effect of Cold-Work Distortion on X-Ray Patterns *J. Appl. Phys.* **21**, 595 (1950).

[47] Krill, C. E. and Birringer, R. Estimating grain-size distributions in nanocrystalline materials from X-ray diffraction profile analysis *Philos. Mag. A* **77**, 621 (1998).

[48] Smetanin, M., Deng, Q., and Weissmüller, J. Dynamic electro-chemo-mechanical analysis during cyclic voltammetry *Phys. Chem. Chem. Phys.* **13**, 17313 (2011).

[49] Erko, A., Packe, I., Hellwig, C., Fieber-Erdmann, M., Pawlizki, O., Veldkamp, M., and Gudat, W. KMC-2: the new x-ray beamline at BESSY II *AIP Conf. Proc.* **512**, 415 (2000)

[50] Sánchez-Bajo, F. and Cumbrera, F. L. The Use of the Pseudo-Voigt Function in the Variance Method of X-ray Line-Broadening Analysis *J. Appl. Crystallogr.* **30**, 427 (1997).

[51] Deng, Q., Gosslar, D.-H., Smetanin, M., and Weissmüller, J. Electrocapillary coupling at rough surfaces *Phys. Chem. Chem. Phys.* **17**, 11725 (2015).

[52] Tsai, H. Elastic properties, damping capacity and shape memory alloys In *Smithells Metals Reference Book, 8th Edition, Chapter 15* Elsevier Amsterdam, Netherlands, 15.1 (2004) Gale, W. P. and Totemeier, T. P., Editors, ISBN: 978-0-7506-7509-3.

[53] Ames, M., Markmann, J., Karos, R., Michels, A., Tschöpe, A., and Birringer, R. Unraveling the nature of room temperature grain growth in nanocrystalline materials *Acta Mater.* **56**, 4255 (2008).

[54] Gale, W. P., Newcomb, S., Totemeier, T. P., and Vandervoort, G. Metallography In *Smithells Metals Reference Book, 8th Edition, Chapter 1* Elsevier Amsterdam, Netherlands, 1.1 (2004) Gale, W. P. and Totemeier, T. P., Editors, ISBN: 978-0-7506-7509-3.

[55] Thompson, C. V. Grain Growth in Thin Films *Annu. Rev. Mater. Sci.* **20**, 245 (1990).

[56] Harper, B. D., Rao, J. M., Kenner, V. H., and Popelar, C. H. Hygrothermal effects upon stress relaxation in a polyimide film *J. Electron. Mater.* **26**, 798 (1997).

[57] Li, H., Shi, L., Wang, Q., Chen, L., and Huang, X. Nano-alloy anode for lithium ion batteries *Solid State Ionics* **148**, 247 (2002).

10 The potential strain coupling parameter of stressed materials

As discussed in chapter 4 the chemical potential for substitutional uptake equals the chemical potential for interstitial uptake in case the active material concentration is directly correlated to a change in the number of lattice places. Hence all following evaluations can be done in an identical way for substitutional uptake.

10.1 The effect of stress on the potential strain coupling parameter

The change in electrode potential with elastic strain is correlated to the change in chemical potential with elastic strain according to equation (3.13):

$$\frac{d\mu_{\text{int}}}{d\varepsilon_{ij}} = -Fz \left. \frac{dE}{d\varepsilon_{ij}} \right|_{\varepsilon_{kl \neq ij}} \tag{10.1}$$

The chemical potential of a binary interstitial solid solution depends on the stress according to [38]:

$$\mu_{\text{int}}(\rho_{\text{Act}}, \sigma_{ij}) = \mu_{0,\text{int}}(\rho_{\text{Act}}) - \frac{\partial \varepsilon_{ij}^{sf}}{\partial \rho_{\text{Act}}} \sigma_{ij} - \frac{1}{2} \left(\frac{\partial C_{ijkl}}{\partial \rho_{\text{Act}}} \sigma_{ij} \right) \sigma_{kl} \tag{10.2}$$

The molar density ρ_{Act} in the reference state can be written as:

$$\rho_{\text{Act}} = \frac{N_{\text{active}}}{N_{\text{host}}} \frac{1}{\Omega \text{mol}} \tag{10.3}$$

Using equation (10.3) to replace ρ_{Act} in the second term of equation (10.2) leads to:

$$\frac{\partial \varepsilon_{ij}^{sf}}{\partial \rho} \sigma_{ij} = \frac{\partial \varepsilon_{ij}^{sf}}{\partial N_{\text{active}}} N_{\text{host}} \Omega N_A \sigma_{ij} \tag{10.4}$$

where N_A is the Avogadro constant. The most general definition of the strain concentration coefficient

$$\eta_{ij} = N_{\text{host}} \left. \frac{d\varepsilon_{ij}^{sf}}{dN_{\text{active}}} \right|_{\sigma_{ij}} \tag{10.5}$$

can be used to transform equation (10.4) into:

$$\frac{\partial \varepsilon_{ij}^{sf}}{\partial \rho_{\text{Act}}} \sigma_{ij} = \eta_{ij} \Omega \text{mol} \sigma_{ij} \tag{10.6}$$

a similar treatment for the third term leads to:

$$\frac{1}{2} \left(\frac{\partial C_{ijkl}}{\partial \rho_{\text{Act}}} \sigma_{ij} \right) \sigma_{kl} = \frac{1}{2} \left(\frac{\partial C_{ijkl}}{\partial N_{\text{active}}} N_{\text{host}} \Omega \text{mol} \sigma_{ij} \right) \sigma_{kl} \tag{10.7}$$

Hence the chemical potential of an interstitial solid solution can be written as:

$$\mu_{\text{int}}(\rho_{\text{Act}}, \sigma_{ij}) = \mu_{0,\text{int}}(\rho_{\text{Act}}) - \eta_{ij}\Omega \text{mol}\sigma_{ij} - \frac{1}{2}\left(\frac{\partial C_{ijkl}}{\partial N_{\text{active}}}N_{\text{host}}\Omega \text{mol}\sigma_{ij}\right)\sigma_{kl} \tag{10.8}$$

With this definition the change in electrode potential upon uni-axial strain in x-direction (11) can be calculated to be:

$$\left.\frac{\text{d}E}{\text{d}\varepsilon_{11}}\right|_{\varepsilon_{ij\neg11}} = \frac{\eta_{ij}\Omega C_{ij11}}{zq_0} + \frac{1}{zq_0}\left(\frac{\partial C_{ijkl}}{\partial N_{\text{active}}}N_{\text{host}}\Omega C_{11ij}\right)\sigma_{kl} \tag{10.9}$$

Which for the special case of a material with cubic symmetry and $\eta_{ij} = \eta\delta_{ij}$, simplifies to:

$$\left.\frac{\text{d}E}{\text{d}\varepsilon_{11}}\right|_{\varepsilon_{ij\neg11}} = \frac{\eta\Omega 3K}{zq_0} + \frac{1}{zq_0}\left(\frac{\partial C_{ijkl}}{\partial N_{\text{active}}}N_{\text{host}}\Omega C_{11ij}\right)\sigma_{kl} \tag{10.10}$$

10.1.1 Correlation to literature

For a strain corresponding to a planar stress state, in an isotropic material and concentration independent compliance values one ends up with equation (3.18), as will be shown in the following:

$$\left.\frac{\text{d}E}{\text{d}(\varepsilon_{11}+\varepsilon_{22})}\right|_{\varepsilon_{ij\neg11,22,33},\sigma_{33}=0} = \frac{\eta\Omega}{zq_0}\frac{\text{d}\delta_{ij}\sigma_{ij}}{\text{d}(\varepsilon_{11}+\varepsilon_{22})} = \frac{\eta\Omega}{zq_0}\frac{\text{d}(\sigma_{11}+\sigma_{22})}{\text{d}(\varepsilon_{11}+\varepsilon_{22})} \tag{10.11}$$

using elasticity theory $\sigma_{11}+\sigma_{22}$ can be written as:

$$\sigma_{11}+\sigma_{22} = \frac{E}{(1+v)(1-2v)}(\varepsilon_{11}+\varepsilon_{22}+2v\varepsilon_{33}) = (\varepsilon_{11}+\varepsilon_{22})\frac{E}{1-v} = (\varepsilon_{11}+\varepsilon_{22})\frac{3K(1-2v)}{1-v} \tag{10.12}$$

by inserting equation (10.12) in equation (10.11) and using, that for an interstitial solid solution $\eta = \widehat{\eta}$ leads to:

$$\left.\frac{\text{d}E}{\text{d}(\varepsilon_{11}+\varepsilon_{22})}\right|_{\varepsilon_{ij\neg11,22,33},\sigma_{33}=0} = \frac{\widehat{\eta}\Omega}{zq_0}B = \frac{\widehat{\eta}\Omega}{zq_0}\frac{3K(1-2v)}{1-v} = \varsigma_{\text{ad}} \tag{10.13}$$

This comparison shows that, in case the compliance parameters are constant, ς_{ad} is the derivative of the chemical potential with respect to a planar strain.

11 Technical drawings

DECMA-stage;
Technical drawings were made by Henning Lohmann
on the basis of blueprints by the author

## Frame: Part 1

Clamp: Part 2

Clamp: Part 3

EINZELHEIT A

A
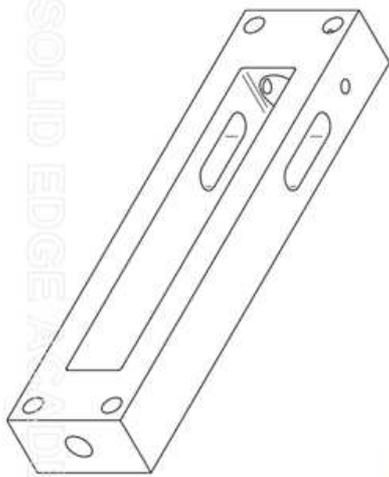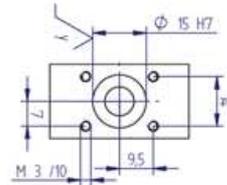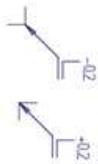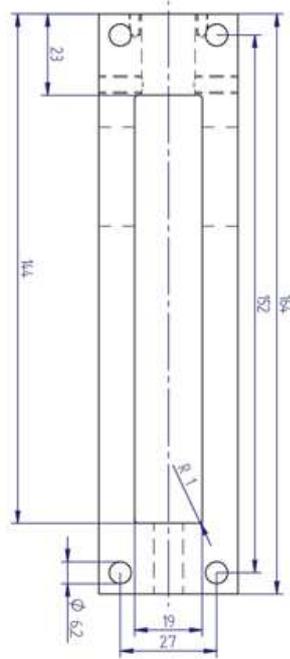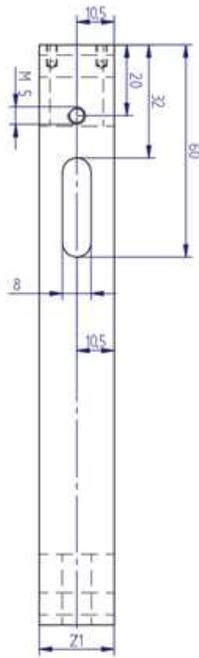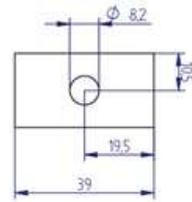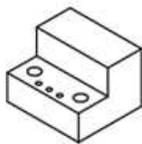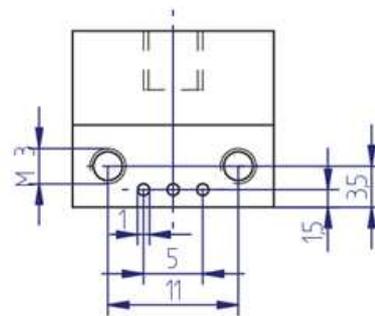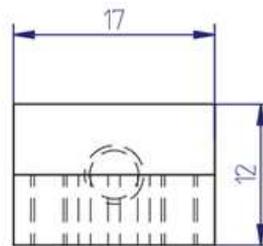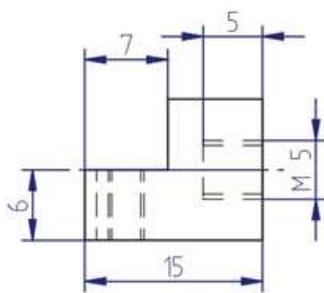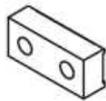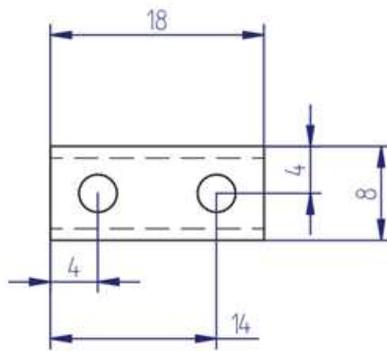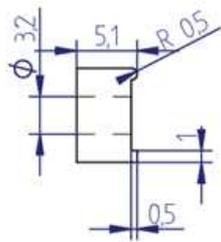
Clamp: Part 4

Clamp: Part 5
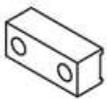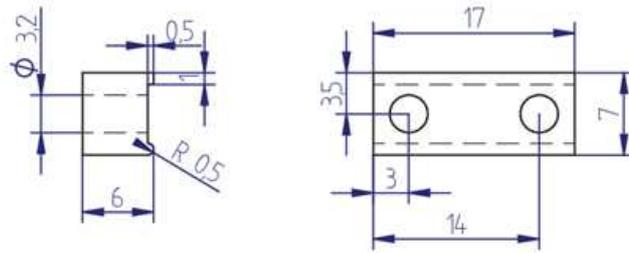
Fixation for Micrometre screw: Part 6
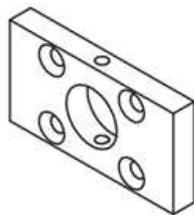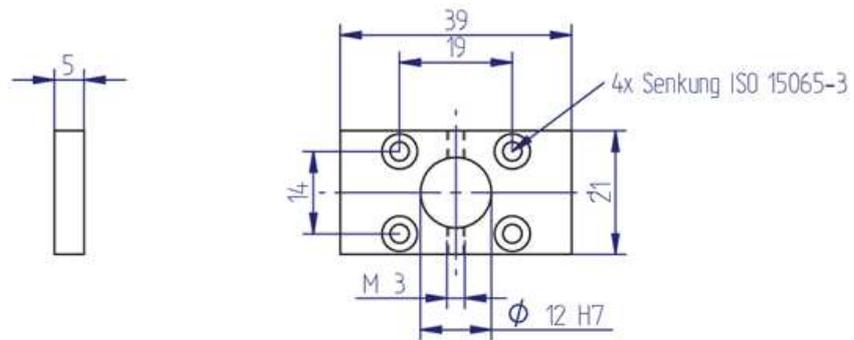
Rack: Part 8
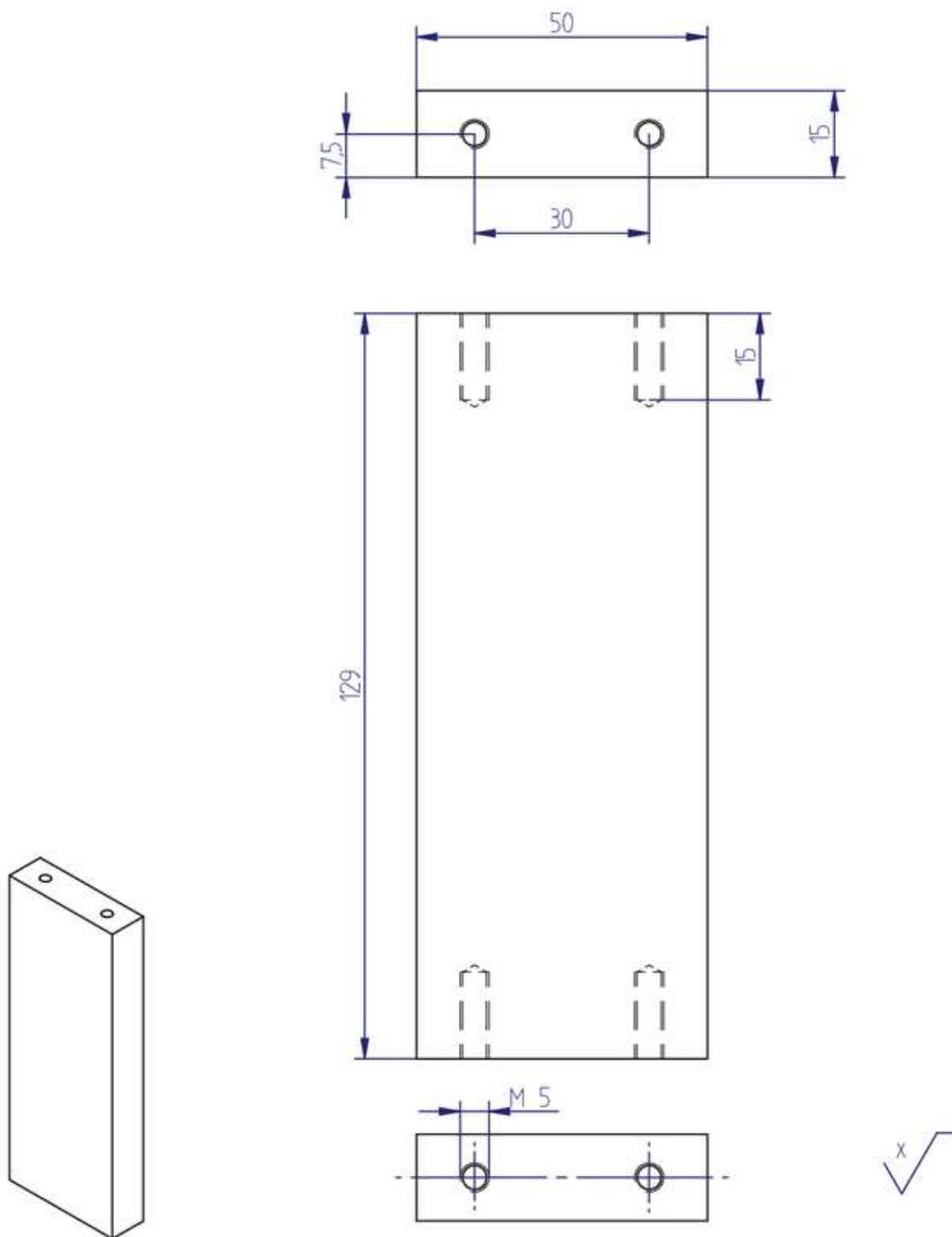
Rack: Part 9
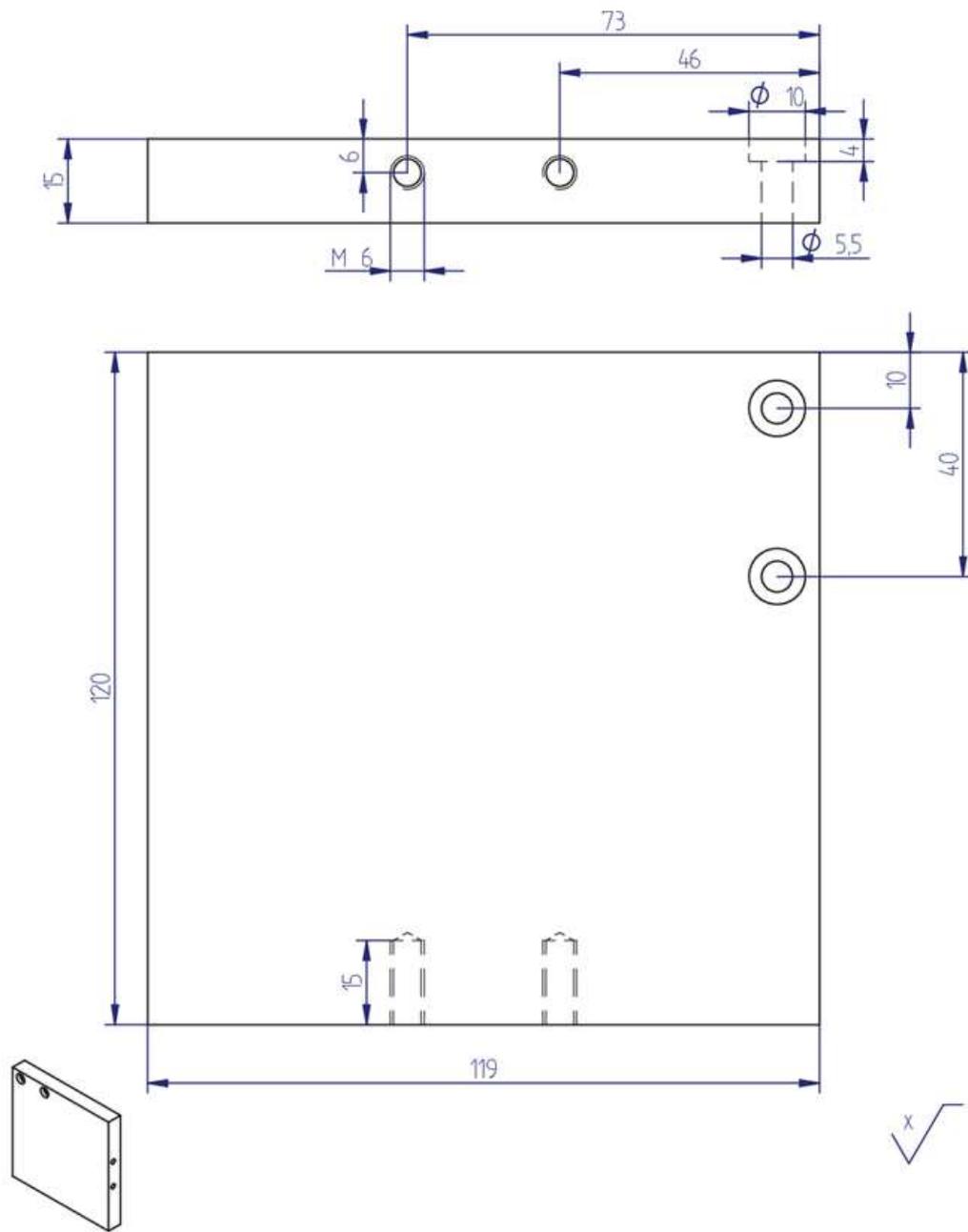
Rack: Part 10
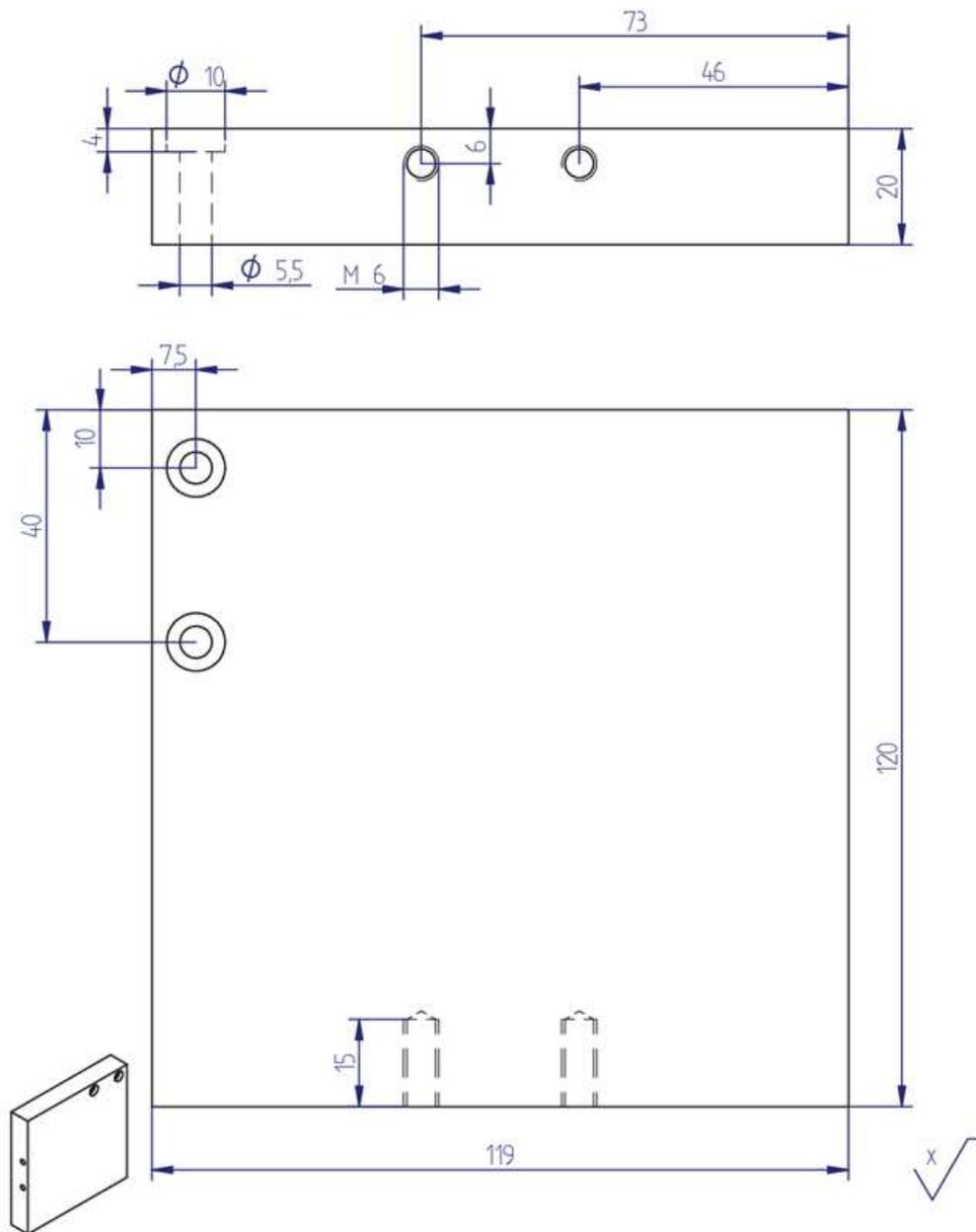
In-situ electrochemical cell
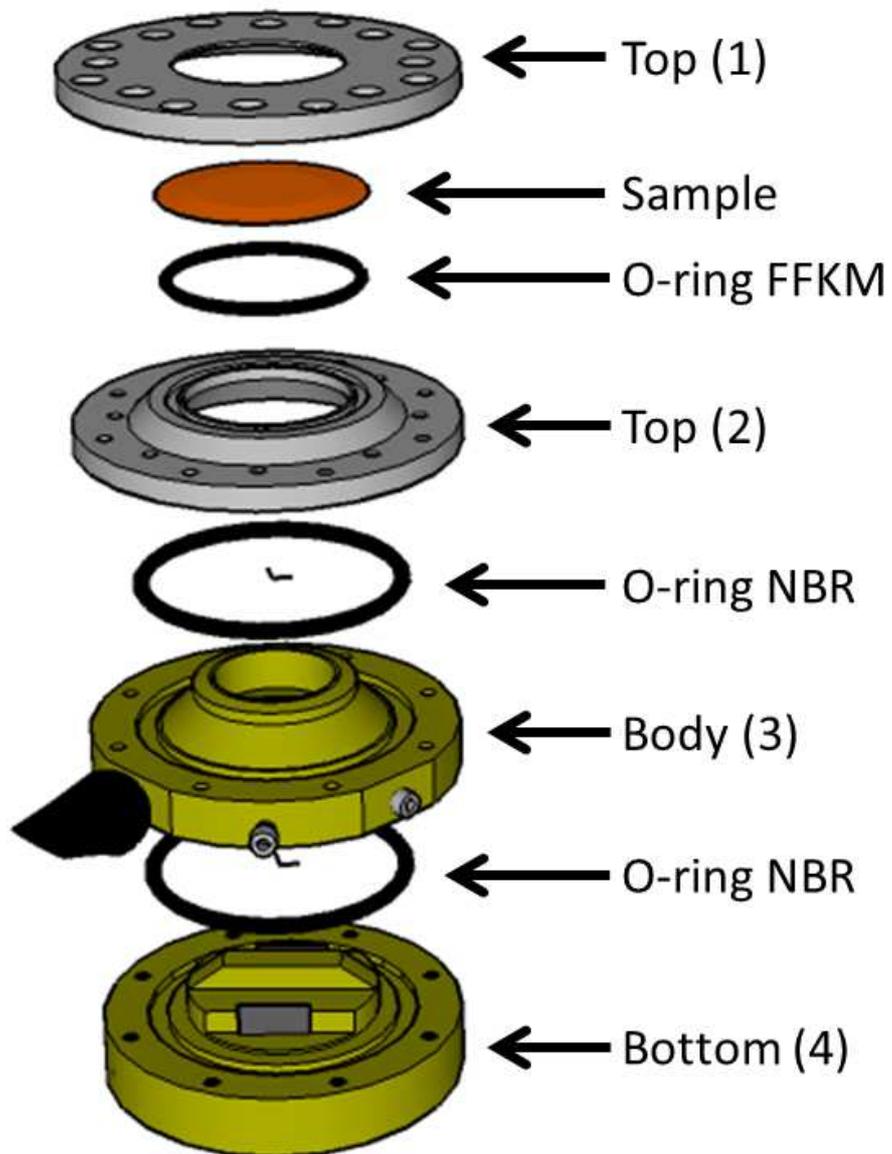
Top (1)
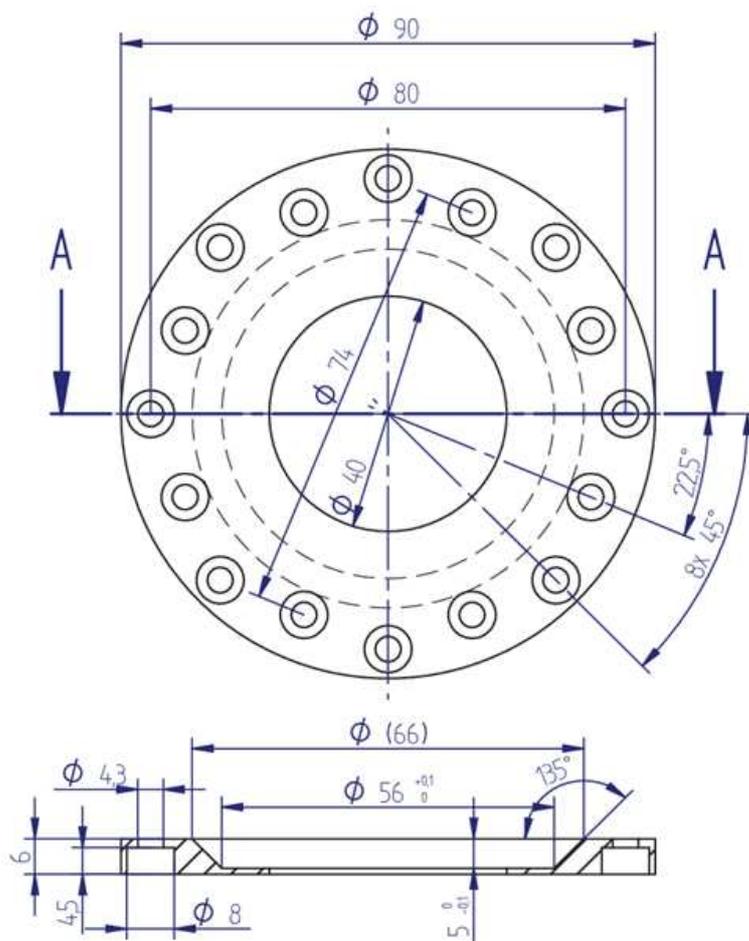
Schnitt A–A
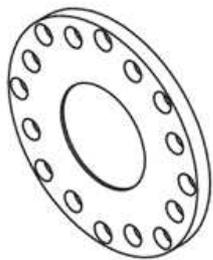
Top (2)
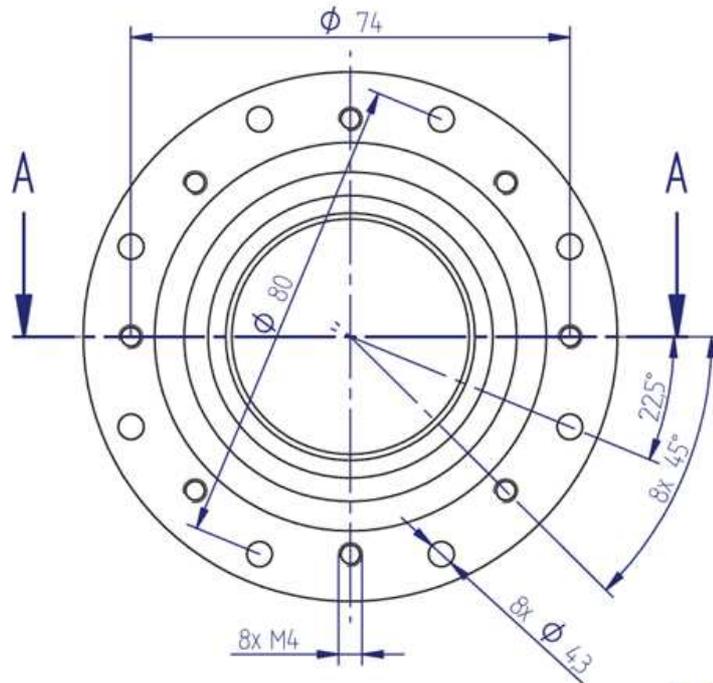
Schnitt A-A
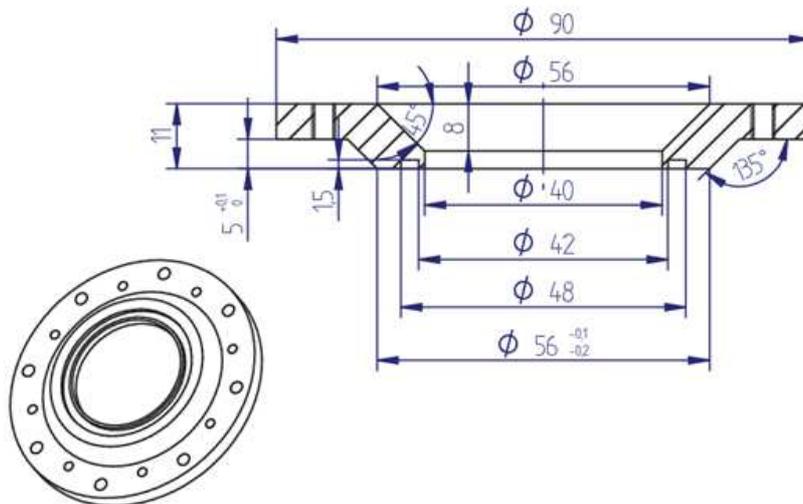
Body (3)

Crossection
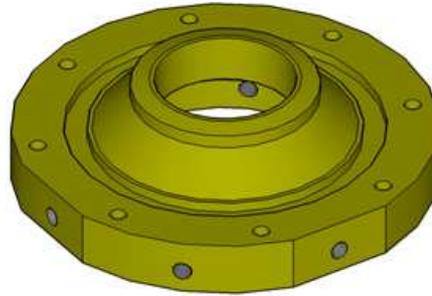
Top view

90mm
68mm
58mm
40mm
32mm
30mm

M4

40mm

Section cut

30mm
29mm
25mm
21mm
16mm
11mm

24mm
23mm
14mm
12mm
10mm
7mm
5mm

Body (3)

Crossection

Top view

15mm
4mm
40mm
4mm
30mm
48mm
58mm
68mm
90mm
45°

Section cut 1

30mm
30mm
21mm
16mm
11mm
5mm

10mm
14mm
16mm
23mm
30mm

Section cut 2

30mm
23mm
17mm
16mm
14mm
10mm
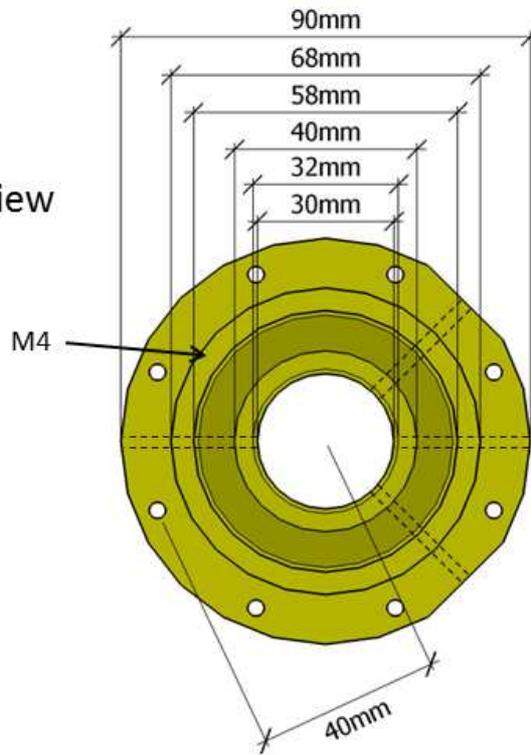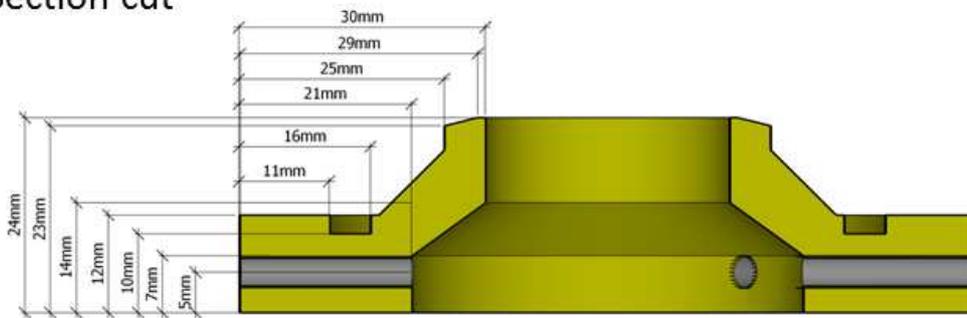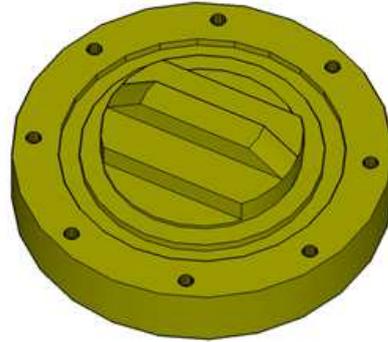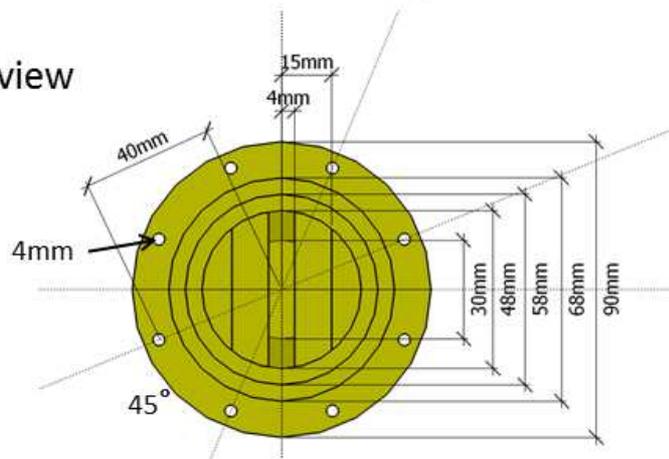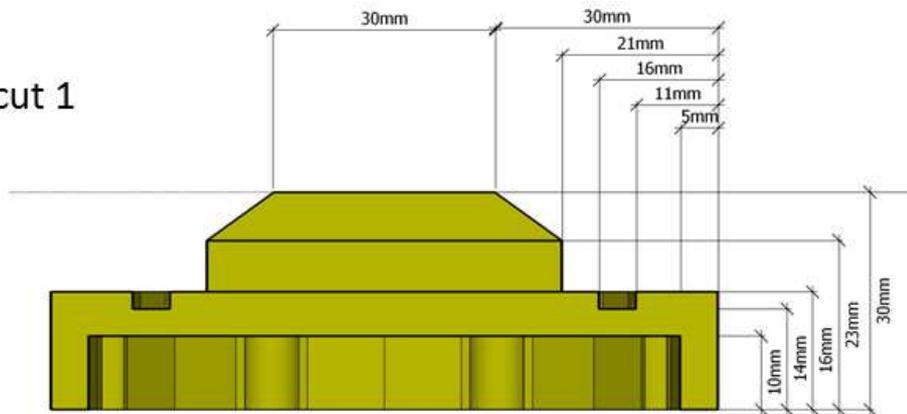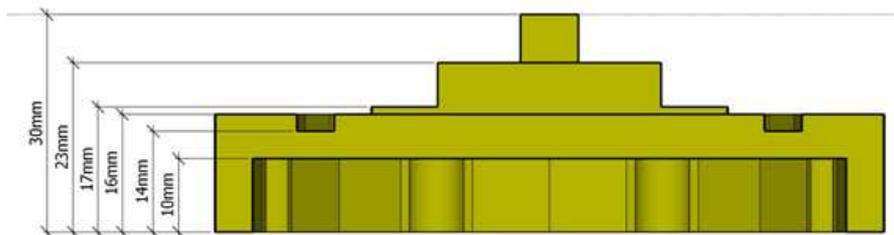
Lebenslauf

Persönliche Daten:

Name:	Mag. Tobias Kitzler
Geburtsdatum:	23.06.1985
Geburtsort:	Haag am Hausruck
Staatsbürgerschaft	Österreich

Bildungsweg:

09.1991 - 07.1995	Volksschule Perg
09.1995 - 07.1996	Hauptschule II Perg
09.1996 - 07.2000	Hauptschule I Perg
09.2000 - 06.2004	Bundesoberstufenrealgymnasium Perg
24.06.2004	Reifeprüfung am Bundesoberstufenrealgymnasium Perg
10.2004 - 09.2005	Zivildienst im Integrativkindergarten Perg
10.2005 - 05.2011	Diplomstudium Physik an der Universität Wien (Mit Auszeichnung abgeschlossen)
13.05.2011	Abschlussprüfung Physik an der Universität Wien
10.2011 - 09.2015	Anstellung als Doktorand am Helmholtz-Zentrum Geesthacht
10.2011 - 11.2016	Doktorarbeit an der Technischen Universität Hamburg
03.11.2016	Disputation der Promotion

Veröffentlichungen:

Diplomarbeit: Kitzler, Tobias (2011), "Impedanzwandler für elektrische Transportmessungen mit kurzen Strompulsen bei tiefen Temperaturen"

Lang W. Puica I. Zechner G. Kitzler T. Bodea M. A. Siraj K. and Pedarnig J. D. "Non-ohmic Electrical Transport Properties Above the Critical Temperature in Optimally and Underdoped Superconducting $YBa_2Cu_3O_{6+x}$" *Journal of Superconductivity and Novel Magnetism* 25(5) 1361 (2012)

Kitzler T. Maawad E. Többens D. M. Ziehmer M. and Markmann J. "The Electro-Chemo-Mechanical Coupling in Lithium Alloy Electrodes and its Origins" *Journal of The Electrochemical Society,* 162(14), A2684–A2691 October (2015)